AD-A208 238

DTIC
ELECTE
MAY 16 1989
D

NUMERICAL MODELING OF TWO-TERMINAL

QUANTUM WELL DEVICES

Prepared by

H. L. Grubin, J. P. Kreskovsky, and M. M. Cahay

for

Air Force Office of Scientific Research

Scientific Research Associates, Inc.
P. O. Box 1058

89 5 15 206

REPORT DOCUMENTATION PAGE

Form Approved
OMB No. 0704-0188

1a. REPORT SECURITY CLASSIFICATION	1b. RESTRICTIVE MARKINGS
Unclassified	

2a. SECURITY CLASSIFICATION AUTHORITY	3. DISTRIBUTION/AVAILABILITY OF REPORT
N/A since unclassified	Approved for public release,
2b. DECLASSIFICATION/DOWNGRADING SCHEDULE	distribution unlimited
N/A since unclassified	

4. PERFORMING ORGANIZATION REPORT NUMBER(S)	5. MONITORING ORGANIZATION REPORT NUMBER(S)
SRA R89-910027-F	AFOSR-TR· 89-0605

6a. NAME OF PERFORMING ORGANIZATION	6b. OFFICE SYMBOL (If applicable)	7a. NAME OF MONITORING ORGANIZATION
Scientific Research Associates		Air Force Office of Scientific Research/NE

6c. ADDRESS (City, State, and ZIP Code)	7b. ADDRESS (City, State, and ZIP Code)
P. O. Box 1058 Glastonbury, CT 06033-1058	Bolling AFB DC 20332-6448

8a. NAME OF FUNDING/SPONSORING ORGANIZATION	8b. OFFICE SYMBOL (If applicable)	9. PROCUREMENT INSTRUMENT IDENTIFICATION NUMBER
AFOSR	NE	F49620-88-C-0108

8c. ADDRESS (City, State, and ZIP Code)	10. SOURCE OF FUNDING NUMBERS			
BLDG. 410 BOLLING AFB, DC 20332-6448	PROGRAM ELEMENT NO.	PROJECT NO.	TASK NO.	WORK UNIT ACCESSION NO.
	61102F	3005	A1	

11. TITLE (Include Security Classification)

Numerical Modeling of Two-Terminal Quantum Well Devices

12. PERSONAL AUTHOR(S)
H. L. Grubin, J. P. Kreskovsky, M. M. Cahay

13a. TYPE OF REPORT	13b. TIME COVERED	14. DATE OF REPORT (Year, Month, Day)	15. PAGE COUNT
Final	FROM 880801 TO 890131	890417	

16. SUPPLEMENTARY NOTATION

aluminum gallium arsenide/gallium arsenide

17. COSATI CODES			18. SUBJECT TERMS (Continue on reverse if necessary and identify by block number)
FIELD	GROUP	SUB-GROUP	Resonant Tunneling Devices, Quantum Potential

19. ABSTRACT (Continue on reverse if necessary and identify by block number)

This report discusses in detail the results of a Phase I investigation of AlGaAs/GaAs resonant tunneling devices (RTD) using the moment representation of the density matrix equation and the concept of a quantum potential. One dimensional numerical simulations of the density matrix equation (i.e., continuity and momentum-balance equations) and the Poisson's equation were performed. Our study constitutes the first attempt to solve numerically the moments of the density matrix equation. Our numerical simulations, while including the effect of momentum relaxation, show the occurence of negative differential conductivity in the current voltage characteristics of RTD. Our simulations were repeated for a variety of RTD, with different barrier/well thicknesses and heights. The influence of the doping profile throughout the entire device on the current-voltage characteristics was also investigated. Additionally, we have studied the rectifying characteristic of the I-V curve of an asymmetric RTD (with different barrier heights), an interesting feature with potential device applications. (KR) ←

20. DISTRIBUTION/AVAILABILITY OF ABSTRACT	21. ABSTRACT SECURITY CLASSIFICATION
☐ UNCLASSIFIED/UNLIMITED ☒ SAME AS RPT. ☐ DTIC USERS	Unclassified

22a. NAME OF RESPONSIBLE INDIVIDUAL	22b. TELEPHONE (Include Area Code)	22c. OFFICE SYMBOL
Witt	(202) 767-4931	NE

DD Form 1473, JUN 86 — Previous editions are obsolete.

TABLE OF CONTENTS

I. Introduction

Since the pioneering work of Tsu and Esaki, there has been a growing interest in double-barrier resonant tunneling devices (hereafter referred to as RTD). Structures grown by both molecular beam epitaxy (MBE) and metalorganic chemical vapor deposition (MOCVD) have been reported with improved peak-to-valley ratios, exhibiting negative differential resistance (NDR) at room temperature. To date, the best peak-to-valley current ratios ever reported were obtained with pseudomorphic $In_{0.53}Ga_{0.47}As/AlAs/InAs$ resonant tunneling diodes [1]. (A schematic cross-section of the device is shown in figure 1). For this RTD, the peak-to valley current ratios are as high as 30 at 300K and 63 at 77K were obtained. In table I, we show some of the substantial improvements in the peak-to-valley ratios of typical $Al_xGa_{1-x}As/GaAs/Al_xGa_{1-x}As$ RTD' made over the last fifteen years [2,7].

The theoretical understanding of the current voltage characteristics of typical RTD's is still far from being complete. Several mechanisms have been proposed to explain the NDR region, including; 1) coherent resonant tunneling throughout the RTD [8] and 2) the mechanism of sequential tunneling proposed by Luryi in which electrons first tunnel through the first barrier, then suffer elastic or inelastic collisions before tunneling through the second barrier [9]. The usual approach to treat coherent resonant tunneling involve various refinements of the original work by Tsu and Esaki [8] and include contributions of a spatially dependent effective mass [10], self-consistent space-charge effects [11] and electron-electron interactions [12]. The Tsu-Esaki approach leads to large peak-to-valley ratios, in some cases one or two orders of magnitude greater than those seen experimentally. The Tsu-Esaki approach also introduces conceptual difficulties, one of which was brought to light by Jogai et al [12b]. In one important case, as pointed out by Jogai et al, in the Tsu-Esaki approach, in which carriers are emitted from the two boundaries, the resulting wave function cannot in general accurately represent the electron density in any accumulation layer that forms at a barrier, particularly when low doped spacer layers are introduced into the design of the device. For if the spacer layers were sufficiently wide, then the electrons would need to tunnel significantly long distances to contribute to current. Indeed the introduction of space layers in the Tsu-Esaki formalism has resulted in significant decreases in the calculated current level [12b], although not necessarily that observed experimentally. Thus additional mechanisms are needed to explain the current observed levels. Jogai et al [12b] proposed that electrons can be thermionically emitted over the spacer layer barrier and fall into the accumulation zone by the emission of a phonon. This process is cumulative and can lead to significant amounts of charge prior to the upstream barrier. In addition if the potential in the well and in the accumulation layer are below that of the emitter Jogai et al [12b] remind us that additional quantum states will form, states that are not part of the streaming Tsu-Esaki formulation. One approach that can avoid many of these difficulties involves use of the Wigner-distribution formalism. In some cases this last approach reproduces the current-voltage characteristic of RTDs [13,14]. However, when the necessary inclusion of scattering is included, this last formalism predicts peak-to-valley ratios that are smaller than experimental values [13]. The origin of these difficulties is discussed in [14].

In this report we describe the results of a Phase I study in which we implement another approach to examine quantum transport in RTDs. We use the moment representation of the density matrix equation. These equations are solved numerically together with Poisson's equation. This is the first time an attempt has been made to solve numerically the moments of the density matrix equation.

The goal of this Phase I study was limited to demonstrating a capability for analyzing typical AlGaAs/GaAs resonant tunneling structures using the moments of the density matrix. The

results of the Phase I study are:

(1) The current voltage relation observed in the RTD reflects contributions from a variety of effects. The **phenomena of resonance** is dominantly a single particle wavefunction effect arising from the placement of a half-integral number of wavelengths in the quantum well. The presence of **accumulation** in the upstream region prior to the first barrier, and **depletion** in the second barrier are dominantly single particle wave function contributions. The voltage at which the peak current occurs is dominated by space charge effects and by the details of the **quantum distibution function. Negative differential resistance is accompanied by locally increasing charge in the well, and by very low carrier velocities in the quantum well**; a result that is consistent with arguments demonstrating long dwell times at resonance. **Physical dissipation** within the device prior to the collecting contacts is a necessary requirement for understanding transport in the RTDs.

(2) Specificially, numerical simulations using the first two moments of the density matrix equation show the occurence of negative differential conductivity in the current-voltage characteristics of resonant tunneling structures. The current levels obtained in numerical simulations have the correct order of magnitude when compared with experimental resulis.

(3) The I-V characteristics of typical device are sensitive to the shape of the resonant tunneling structure and to the doping profile in the cladding layers sandwiching the RTD.

(4) The voltage at which NDR is calculated is obtained only for the tunnel structure and its immediate adjacent layers. Thus, the voltage is only a small fraction of the actual device size. The numerical values are thus lower than that seen experimentally. For situations where the quantum distribution function plays a role similar to that implemented in the Tsu-Esaki picture, the voltage at peak current occurs at values similar to that predicted by others.

(5) For the first time, this study has shown that the quasi Fermi-level is changing rapidly over the region of interest, i.e., the RTD itself. This result generalizes previous theories where the Fermi level was assumed to be constant for electrons incident from either contacts and equal to its value in the corresponding contact.

(6) Asymmetric RTDs were studied, tending to reinforce many of the above comments. Additionally several new device applications as current rectifiers, emerge.

(7) **The key conclusion is that resonance is dominated by single particle contributions, and that the voltage dependence is dominated by the boundary conditions and the particle distribution function.**

The purpose of this report is to describe in detail the above key results arising from SRA's Phase I SBIR study. The report is divided into seven sections. Sections II and III provide a brief description of the equations used in this Phase I study. Starting with the quantum density matrix equation, we derive the first two moment-equations thereof, for examining transport in quantum phase based devices. Two significant features of the approach are taken at SRA: (1) the introduction of Bohm's quantum potential into the transport formulation, (2), the use of the first two moment equations of the density matrix equation coupled to Poisson's equation to calculate self-consistently the current-voltage characteristics of typical RTD's. Additionally, we also calculate the self-consistent charge density, conduction band energy profiles throughout the entire device. Section IV describes briefly the numerical approximations used to solve the governing equations given in section III. Section V contains a description of the different resonant tunneling structures studied in this Phase I, and the general features of resonance. A systematic study including the

influence of barrier of barrier height, barrier and well thickness and doping profiles on the shape of the current-voltage characteristics has been performed and is described in Section VI. Additionally, we have studied the rectifying characteristic of the I-V curve of an assymetric RTD (with different barrier heights). Finally, Section VII contains the conclusions and recommendations. Appendices are included that describe in more detail the numerical procedures used to solve the governing equations, the basis for the governing equations and alternative procedures.

II. Transport in Quantum Based Devices

The quantum mechanical description of transport in the Phase I study of resonant tunneling structures is based upon the use of the Bohm quantum potential [14b], and we spend some time discussing this potential. The potential is best understood by beginning with a single particle formulation of quantum mechanics. We start with the single particle Schrodinger equation:

$$i\hbar \frac{\partial \Psi(x,t)}{\partial t} = -\frac{\hbar^2}{2} \frac{\partial}{\partial x}\left[\frac{1}{m}\frac{\partial \Psi(x,t)}{\partial x}\right] + E(x,t)\Psi(x,t) \tag{1}$$

where we are assuming that the effective mass is spatially dependent, and that we are in a time dependent mode.

Without any loss of generality we write the single particle wavefunction in the following form:

$$\Psi(x,t) = R(x,t)\exp[iS(x,t)/\hbar] \tag{2}$$

(Note: under special cases it is possible to separate S(x,t) into a part that is dependent only on position and a part that is dependent only upon time, as in the case of the separation of variables that leads to the time independent Schrodinger equation.) Then defining momentum and probability density as:

$$m(x)v(x,t) = \partial S(x,t)/\partial x \tag{3}$$

$$\rho(x,t) = R(x,t)^2 \tag{4}$$

Schrodinger's equation can be written in the form:

$$\frac{\partial \rho}{\partial t} + \frac{\partial \rho v}{\partial x} = 0 \tag{5}$$

$$\frac{m\partial v}{\partial t} = -\frac{\partial(E+Q)}{\partial x} - \frac{1}{2}\frac{\partial mv^2}{\partial x} \tag{6}$$

where Q(x,t) is a potential that is quantum mechanical in origin, and has been referred to as the quantum potential (see ref. 14b and references therein). Q(x,t) is defined as:

$$Q(x,t) = -\frac{\hbar^2}{2}\frac{1}{\sqrt{\rho}}\frac{\partial}{\partial x}\left[\frac{1}{m}\frac{\partial\sqrt{\rho}}{\partial x}\right] \tag{7}$$

Equations (5) and (6) represent the hydrodynamic form of Schrodinger's equation. They are, however, subject to the constraint of single-valuedness of the wave-function. In writing down the single-valuedness condition it is important to recognize an important difference between the hydrodynamic formulation and the usual form of Schrodinger's equation. Schrodinger's equation is correctly written in terms of the canonical momentum and allows

for the presence of a vector potential $A(r,t)$. Thus the momentum must be generalized from equation (3) to read (in three dimensions):

$$m(r)v(r,t) = \nabla S(r,t) - eA(r,t) \qquad (8)$$

and the constraint is expressed as:

$$\oint \nabla S \cdot dr = nh \qquad (9)$$

The above constraint means that allowed movements of a quantum fluid have to be restricted in such a way that the integral of the velocity around a circuit containing a flux line depends upon the flux in that circuit.

In the single particle picture, if the particle history was determined along a characteristic path then the acceleration would be determined by the applied classical field, which in equation (6) is given by $-\partial E/\partial x$ and by the quantum mechanical force, which is dependent upon gradients of probability density and introduces nonlocality. To examine its significance we consider a simple contribution obtained by examining the form of the quantum potential, at one instant of time for a particle that is described by a minimum wave packet. Recall, that in time the shape of the minimum wave packet is constant and is of the form [14c]:

$$\rho(x,t) = [1/\sqrt{2\pi\sigma}]\exp[-(x-<x>)^2/2\sigma] \qquad (10)$$

where $<x>$ is the expectation value of position at time t, and $\sigma = \hbar/2m\omega$. For $\rho(x,t)$ given by equation (10), the quantum potential is given by

$$Q(x,t) = (\hbar\omega/2)[1 - 2(x-<x>)^2/\sigma] \qquad (11)$$

and the quantum mechanical force associated with the quantum potential is given by:

$$-\partial Q(x,t)/\partial x = 2\hbar\omega(x-<x>)/\sigma \qquad (12)$$

Let us now consider what is occuring. Classically, if a particle is subject to a constant accelerating force, i.e., $E(x,t) = -Fx$, where x represents position along a characteristic path, then along this path the velocity will increase in one direction at a rate that is linear in time. When the quantum potential is included there are two cases to consider. The first case is that in which σ is sufficiently large such that the quantum potential is always positive. For this case quantum effects are negligible. The second case is that where σ is very small, and the wave packet has a sharp peak. Here, Q can be negative over a small region and specific quantum effects occur. Indeed, to the left of the packet, the quantum force tends to decelerate the wave packet, whereas to the right of the wave packet the quantum force tends to enhance the acceleration. Indeed it may be anticipated that this quantum force is responsible for the spreading of the wave packet as it travels in time. But more to the point, the effect of a narrow, large density gradient charge distribution has the effect of retarding the motion of carriers and may also be responsible for the reflection of wavepackets at boundaries.

Now the Schrodinger equation is second order in space, and dissipationless numerical schemes have been developed to examine the space and time dependence of a host of different problems, including double barrier structures. The implementation of these procedures has been discussed earlier by the present authors [14d]. We emphasize however the fact that the quantum potential above is obtained from the single particle wave function. Further, since present algorithms for solving the single particle Schrodinger's equation are limited in their ability to calculate probability current, and since multiparticle current is

is one of the connectors to measurement, alternative approaches are required. The approach at SRA is based upon the quantum hydrodynamic equation. To develop an intuition for the multiparticle approach, we first illustrate the hydrodynamic features of the single particle Schrodinger equation, in the limit of zero time derivatives of equations (5) and (6).

IIa. Hydrodynamic Aspects of the Single Particle Schrodinger Equation.

The presence of a zero time derivative of the momentum balance equation implies that $S(x,t) = S_1(x) + S_2(t)$, and $R(x,t) = R(x)$. In the case of zero time derivatives, one space integration yields (ignoring spatial derivatives of the effective mass):

$$mv^2/2 + (E+Q) = E_0 \qquad (13)$$

$$\rho v = J \qquad (14)$$

where E_0 and J are constants of integration. We rewrite equation (13) by replacing v by the constraint of constant current, then

$$\frac{d^2\sqrt{\rho}}{dx^2} + \frac{2m}{\hbar^2}\left[[E_0 - E(x)] - \frac{mJ^2}{2\rho^2}\right]\sqrt{\rho} = 0 \qquad (15)$$

Let us examine the above equation in the context of generic problems. First consider a bound state problem. For bound states the wave function of the system, apart from an arbitrary phase, is a real function. The probability current, J, is zero. For the case of a harmonic oscillator, with $E = kx^2/2$, the above differential equation is that of a harmonic oscillator, with the concomitant bound states. The situation of a particle in a box is equally interesting. For the case of large walls, the wavefunctions outside the box are real and evanescent. The probability current is zero, and the above equation leads to bounds states. The question of interest is how do we solve equation. The traditional approach is to solve the equation in separate regions and match boundary conditions. Consider the case of a particle approaching a wall. Assume a structure as given below:
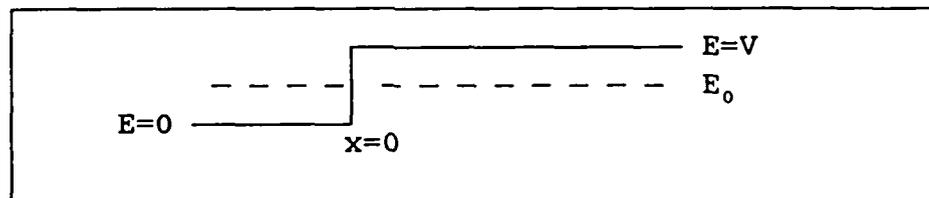
and we assume that $0 < E_0 < V$. The wave function for this problem consists of an oscillatory component to the left of the barrier followed by a evanescent wave to the right of the barrier (see, e.g., Fig. 7, pg 326 of Bohm [14c]). A simple examination of the above differential equation indicates that the solution to the left of the barrier is

$$\sqrt{\rho} = A\sin kx + B\cos kx, \qquad (16)$$

where

$$k = [2mE_0/\hbar^2]^{1/2} \qquad (17)$$

To the right of the barrier:

$$\sqrt{\rho} = C\exp{-\kappa x} \qquad (18)$$

where

$$\kappa = [2m(E_0-V)/\hbar^2]^{1/2} \tag{19}$$

Continuity of $\sqrt{\rho}$ and its first derivative yields a solution in terms of one coefficient. To obtain this coefficient, unity particle normalization is invoked. Now the $J = 0$ situation leads to eigenvalue problems, and bound states can be found. When $J \neq 0$, equation (15) is nonlinear, and we are no longer dealing with an eigenvalue problem; but as in the case of a regional approximations solutions can be obtained for well defined values of 'k' and 'κ', (see equations (17) and (19)).
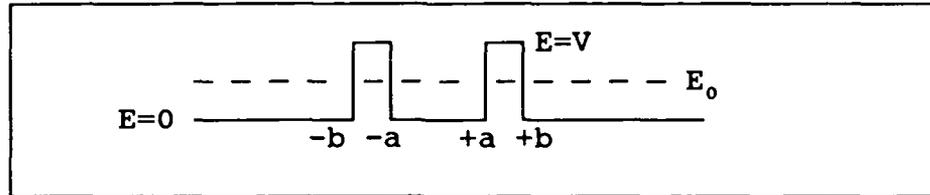
At this point we consider approximate regional solutions to the situation depicted in the above double barrier figure. In examining the solutions we define several quantities to simplify the form of equation (15). First, let

$$\alpha = (mJ/\hbar)^2 \tag{20}$$

Then, equation (15), in the first, third, and fifth regions, reads:

$$\frac{d^2\sqrt{\rho}}{dx^2} + \left[k_0^2 - \frac{\alpha}{\rho^2}\right]\sqrt{\rho} = 0 \tag{21}$$

Defining,

$$\xi = (\sqrt{\rho})^{'} \tag{22}$$

and dividing equation (21) by 'ξ', the following differential equation emerges

$$\frac{d\xi}{d\sqrt{\rho}} + \left[k_0^2 - \frac{\alpha}{\rho^2}\right]\frac{\sqrt{\rho}}{\xi} = 0 \tag{23}$$

Equation (23) integrates directly to:

$$\xi^2 + [k_0^2\rho + \alpha/\rho] = \xi_0^2 \tag{24}$$

where ξ_0^2, is an integration constant. A second integration, using 2.261 of reference [14e], yields:

$$2k_0^2\rho(x) = \xi_0^2 + [\xi_0^4-4\alpha k_0^2]^{1/2}\sin(2k_0x + \phi) \tag{25}$$

where ϕ is a second constant of integration. The differential equation in the barrier region has solutions:

$$2\kappa_0^2\rho(x) = \zeta_0^2 + [4\alpha\kappa_0^2-\zeta_0^4]^{1/2}\sinh(2\kappa_0x + \vartheta) \tag{26}$$

where ζ_0 and ϑ are constants of integration.

Consider the significance of the above results. Standard textbook examples demonstrate that for a square potential well of width 2a, that unity transmission resonance occurs when,

$$2k_0 a = n\pi \tag{27a}$$

The resonance condition for a double barrier is in the WKB approximation (see Bohm; Quantum Theory, p. 286 [14c])

$$\int_{-a}^{+a} k_0(x)\,dx = (n+1/2)\pi \tag{27b}$$

Exact solutions that incorporate finite barrier height and width introduce additional phase contributions. Returning to equation 25, for purposes of illustration, we assume $\phi = \pi/2$. Then between the two barriers of the above figure, the maximum value of $\rho(x)$ occurs at $x = 0$, and the minimum value occurs at $x = \pm a$. These values are:

$$\rho = \xi_0^2 \pm [\xi_0^4 - 4\alpha k_0^2]^{1/2}/2k_0^2 \tag{28}$$

Solutions within the barrier are fit with the hyperbolic functions, and are matched to solutions outside the barrier. The solutions outside the barrier maintain their oscillatory nature, and as such there is a region outside the barrier that will show local accumulation followed by depletion, et cyclic, as displayed below:
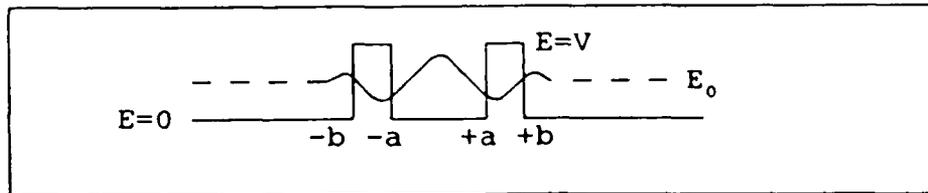
The above picture is artificial because it doesn't account for the fact that in a situation in which particles are subject to bias, the transport is not symmetric. In the presence of this asymmetry the solutions for a net flow of carriers from left to right is expected to look like that shown in the diagram below:
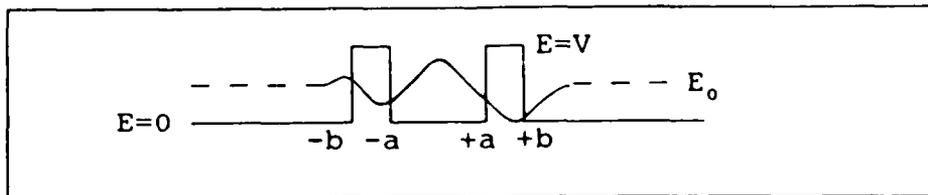
The above solutions suggest that the presence of charge accumulation at the upstream barrier, and charge depletion at the downstream barrier are a consequence of the single particle wavefunction quantum properties. These conclusions will emerge from our later discussion.

The above qualitative discussion was entirely set around finding solutions to the differential equation for the amplitude of the single particle wave function, where we invoked the constraint of conservation of probability current. It is useful to recall that the formal steps leading to the WKB approximation [14f] involves the same philosophy, but instead of solving the differential equation for amplitude, the differential equation for the gradient of the phase is solved. To see this we use the definitions of v and ρ, as given by equations (3) and (4); then writing as shorthand $S' = \partial S/\partial x$, equations (13) and (14) combine as:

$$S'^2 = 2m(E_0-E)+(\hbar^2/4)[3(S''/S')^2-2(S'''/S')] \qquad (29)$$

As discussed by Messiah [14f], the above equation is rigorously equivalent to Schrodinger's equation. However, in the WKB approximation one expands the phase S in a power series in $\hbar^2$:

$$S = S_0 + \hbar^2 S_1 + \dots, \qquad (30)$$

substitutes this expansion into equation (29) and keeps only the zero-order terms. Thus $S'^2 \approx S_0'^2$, and the quantum potential is ignored, except as higher order effects. The turning points require a different approach. Thus, within the context of the WKB approximation, the time independent Schrodinger equation, is replaced by another equation (see Messiah, equation VI. 48 [14f]). In the approach taken below, the WKB approximation is not invoked. But the SRA approach has its own approximation, which are identified in Section IV.

III. Evolution of the Quantum Transport Equations

While the above numerical considerations will be discussed below, a principle point that must be emphasized is that the above description is in terms of single particle wavefunctions. For the systems that we are concerned with, it is the multiple particle wave functions that are of importance. This will require a considerable discussion, and is deferred to appendix C. At this point, we refer to some recent work of Ancona and Iafrate [15], who demonstrated, through an expansion of the Wigner-Bloch differential equation with off diagonal contributions, that the quantum potential with ρ, **representing the carrier density** of the system, was the lowest order quantum statistical contribution to carrier transport in semiconductors. They derived a generalized drift and diffusion equation formulation that differed from the classical drift and diffusion equation formulation through the incorporation of the quantum potential. The constant proceeding the Quantum potential in the study of Ancona and Iafrate differ from that in the SRA study. The origin and significant of this difference is currently under study.

One important feature of the Ancona and Iafrate study [15] is the presence of dissipation. Now the discussion of the the single particle Schrodinger equation, which is dissipationless, offers conceptual difficulties when we make a transition from a single particle picture to a to a multiparticle problem with contacts. These difficulties are present in both quantum and classical transport. It is important to consider this point. For example, in the case of classical multiparticle transport, with electrons assumed to be moving ballistically within the N^- region of a symmetrically fabricated $N^+N^-N^+$ structure, the mean carrier energy increases in going from the cathode to the anode, as would the carrier velocity. Conservation of multiparticle current requires that increases in velocity are accompanied by decreases in particle density. Thus classically in the **absence** of dissipation there will necessarily be charge **depletion** at the downstream anode - unless dissipation is present in the interior of the device. If the assumption is made, as is ususally done, that the physical contact conditions are represented by boundaries where the numbers of carriers at the cathode and anode are equal, then **scattering within the interior of the structure is conceptually necessary.** Similar dissipation issues arise quantum mechanically. In the problems we are solving the device is represented by a 2000A computational domain. The size of the simulated device is at least a factor of at least five smaller that the transport domain of the structure shown in figure 1, which has additional anode and cathode layers. Thus, the effects of physical dissipation in the problem studied studied in the Phase I program may be over emphasised. In the Tsu-Esaki formulation which is for multiparticles, all interior dissipation is ignored. For the hydrodynamic formulation of the **single** particle

Schrodinger's equation, there is no meaning to introducing N^+ cathode and anode regions, since we are dealing with a single particle. This is not the case when the density matrix is invoked.

In the problems studied below, we have started from the density matrix, and include disspation. The equations used have the same relation to that of Ancona and Iafrate [15], as the first two moments of the Boltzmann transport equation have to the semiconductor drift and diffusion equations (although without the rigor of development). The first two moment equations we deal with are the continuity and momentum balance equations. The continuity equation is as given by equation (5) with ρ as carrier density, and v as mean carrier velocity. The momentum balance equation is written in terms of velocity flux densities, ρv. We now examine the intuitive evolution of the quantum momentum balance equation. We again start from the single particle wave function.

For the case of the **single particle wave-function**, combining equations (5) and (6) yields the following probability momentum balance equation:

$$\frac{\partial \rho v}{\partial t} + \frac{\partial \rho v^2}{\partial x} = - \frac{\rho \partial (E+Q)}{m \partial x} - \frac{\rho v^2}{2m} \frac{\partial m}{\partial x} \tag{31}$$

Now from the classical moments of the Boltzmann transport equation, the momentum balance equation , assuming Boltzmann statistics, is:

$$\frac{\partial \rho v}{\partial t} + \frac{\partial \rho v^2}{\partial x} = - \frac{\rho}{m}\left[\frac{\partial E}{\partial x} + \left(\frac{mv^2}{2} - \frac{3kT}{2}\right)\frac{1}{m}\frac{\partial m}{\partial x}\right] - \frac{1}{m}\frac{\partial \rho kT}{\partial x} - \rho v \Gamma \tag{32}$$

On the basis of equations (31) and (32), incorporation of the quantum potential is direct. The resulting quantum momentum balance equation for a **collection of carriers of density ρ** is:

$$\frac{\partial \rho v}{\partial t} + \frac{\partial \rho v^2}{\partial x} = - \frac{\rho}{m}\left[\frac{\partial (E+Q)}{\partial x} + \left(\frac{mv^2}{2} - \frac{3kT}{2}\right)\frac{1}{m}\frac{\partial m}{\partial x}\right]$$

$$- \frac{1}{m}\frac{\partial \rho kT}{\partial x} - \rho v \Gamma \tag{33}$$

In equations (32) and (33), T represents an electron temperature and Γ represents a momentum scattering rate. During the phase I study is Γ constant and equal to 3.3×10^{12}/sec.

In the case of Fermi statistics, with the inclusion of the quantum potential, the relevant momentum balance equation is:

$$\frac{\partial \rho v}{\partial t} + \frac{\partial \rho v^2}{\partial x} = - \frac{\rho}{m}\left[\frac{\partial (E+Q)}{\partial x} + \left(\frac{\rho v^2}{2} - \frac{NkTF_{3/2}}{\rho}\right)\frac{1}{m}\frac{\partial m}{\partial x}\right]$$

$$- \frac{2}{3m}\frac{\partial NkTF_{3/2}}{\partial x} - \rho v \Gamma \tag{34}$$

where, N is the density of states of the conduction band,

$$N = \frac{1}{4\pi^3}\left[\frac{2\pi m kT}{\hbar^2}\right]^{3/2} \tag{35}$$

and

$$F_\ell(x_f) = \frac{2}{\sqrt{\pi}} \int_0^\infty \frac{x^\ell \, dx}{1+\exp(x-x_f)} \qquad (36)$$

Here,

$$x_f = (E_f - \varepsilon)/kT. \qquad (37)$$

The incorporation of the pressure gradient in equations (33) and (34) represents the effect of the mixed states. **At this point there is no reason to assume that the form of the pressure gradient as used here is either correct or incorrect. Indeed the form of the pressure gradient is a consequence of assuming that the quantum distribution function has the form of a displaced Fermi Dirac distribution function. The solutions are dependent upon this choice. It is anticipated that a rigorous form of the quantum pressure gradient will emerge from the energy balance equation to be studied during a Phase II program.**

During the Phase I study the pressure gradient is as given by equation (34), although some modifications, as discussed below, were introduced. Within the context of equation (34) we introduce the Fermi energy, which within the framework of the discussion below is strictly a mathematical transformation. Now classically equation (36) identifies E_f as the Fermi energy, ε the bottom of the conduction band, and under equilibrium conditions:

$$F_{1/2}(x_f) = \rho/N, \qquad (38)$$

Under the quantum mechanical conditions, x_f is identified as

$$x_f = (E_f - E - Q)/kT \qquad (39)$$

which we recognize as being similar in philosophy to that of Ancona and Iafrate [15]. In the study discussed below the carrier density ρ is obtained self-consistently. The quantity E_f is **defined and obtained** through equation (38). In terms of E_f, the momentum balance equation reads:

$$\frac{\partial \rho v}{\partial t} + \frac{\partial \rho v^2}{\partial x} = -\frac{\rho}{m}\left[\frac{\partial E_f}{\partial x} + \left(\frac{\rho v^2}{2} - \frac{NkTF_{3/2}}{\rho}\right)\frac{1}{m}\frac{\partial m}{\partial x}\right] - \rho v \Gamma \qquad (40)$$

where we have used the identify:

$$\frac{2}{3}\frac{dF_{3/2}}{dx_f} = F_{1/2}(x_f) \qquad (41)$$

In implementing equation (41) and in order to avoid the time consuming efforts of inverting the Fermi-integral in equation (41), the latter was replaced by the following approximate relationships:

$$x_f = \ell n(\rho/N) + \rho/(N\sqrt{8}), \qquad \text{for } x_f < 4.4426 \qquad (42a)$$

$$x_f = (9\pi/16)^{1/2}(\rho/N)^{2/3}, \qquad \text{for } x_f > 4.4426 \qquad (42b)$$

Equation (41) coupled to the equation of continuity, equation (5), with ρ identified in both equations as the ensemble averaged density of particles are two of three governing equations in the study performed. The third equation is Poisson's equation. To write this

down it is necessary to have a more complete definition of the energy E(x) appearing in the above equations. For the study considered here E(x) is the energy of the conduction band with the presence of the heterostructure represented by the Anderson rule:

$$E = \Sigma - \chi(x) \tag{43}$$

where $\chi(x)$ is a position dependent electron affinity. Σ is obtained from Poisson's equation:

$$\nabla\epsilon\nabla\Sigma = e^2[\rho - \rho_0] \tag{44}$$

where $\epsilon(x)$ is position dependent permitivity, and ρ_0 is a position dependent doping level.

For conduction band variations between GaAs and $Al_xGa_{1-x}As$, the following relationships were used:

$$m^* = 0.067 + 0.083x \tag{45a}$$
$$\Delta E_c = 0.697x \tag{45b}$$

At the present stage of our study, no attempt was made to include the energy balance equation. In other words, no energy dissipation is actually included in the present formulation. The last term on the right-hand side of equation (40) describes at best some momentum relaxation in the device. Refinements to be made to our approach to include energy dissipation (such as due to phonon scattering which is an inelastic scattering mechanism) will be considered in the future.

It is instructive, for purposes of later discussion to introduce two expressions. The first is a rewriting of the quantum equation (39):

$$\frac{d^2\sqrt{\rho}}{dx^2} + \frac{2m}{\hbar^2}\left[[E_f - E(x) - kTx_f]\right]\sqrt{\rho} = 0 \tag{46}$$

Thus the density of particles is altered by statistics. The second, introduces a quantity:

$$<k> = [<2m^*Q/\hbar^2>]^{1/2} \tag{47a}$$

with Q in ev, and m^* in units of the free electron mass

$$<k> = 0.5123(A^{-1})[<m^*Q>]^{1/2} \tag{47b}$$

Consider equation (46). Anticipating later results, we note that all of our calculations indicate that the quantum quasi-fermi level is approximately constant up to the beginning of the second barrier. In these calculations the value of E_f at the emitter is arbitrarily set to zero. We now consider several key features of the above crucial quantities.

III.a The Shape of the Quantum Potential

First we note that classical statistics teaches that the presence of low or undoped spacer layers, can result in built-in potential (or barrier) associated with the spacer layer, and that the barrier can have energies exceeding the energies of the carriers at the emitter. It is not an issue at low temperatures. In the absence of any quantum mechanical contributions, $E(x) = E_f - kTx_f$; when quantum mechanical contributions are introduced, any difference between the left and right hand sides of this equation is a consequence of quantum mechanical contributions. For example, for wide spacer layers quantum mechanical tunneling into these spacer layers is unlikely, there is a buildup of charge to the left of the

classical barrier height, resulting in a decrease in the upstream barrier height.

Figure 2 shows the equilibrium distribution of charge , quantum potential, and energy under zero bias conditions for a double barrier structure located at the center of a nominally undoped portion of a structure containing N^+ contacts. The structure will be discussed in more detail later. Note the presence of local charge accumulation within the spacer layer, and the presence of local charge accumulation in the symmetric center of the device. The quantum potential, which is plotted in figure 2b shows small positive values within the space layer, as well as between the barriers. However, within the barriers Q is negative.

Moving into the device, for a sufficiently long spacer layer, the charge density will approach its classical value until the barrier is reached. Within the barrier tunneling is possible for sufficiently narrow barriers; and charge exists where none would be present classically. Classically, the absence of any charge would result in $kTx_f \sim -E_g/2$, where E_g is the bandgap of the barrier material. The presence of tunneling reduces the magnitude of x_f, i.e. Q is negative in the barrier. But prior to tunneling through the well, it is clear that not all carriers will achieve this tunneling, and thus there will be an accumulation of charge upstream from the well, as there was upstream from the spacer layer. Thus prior to a negative value of Q in the barrier, Q will be positive upstream from the well. (See figure 2b)

The well is classically accessible by thermionic emission over the barriers, and quantum mechanically through tunnelling. Particles in the well, as well as the carriers upstream of the built-in potential and the emitter barrier will accumulate, and Q is positive. In the second barrier Q is negative.

How may we expect Q to vary with applied bias. Increasing the potential difference between the emitter and collector, with the carriers entering the device with the reference Fermi energy, will result in a gradual decrease in energy E(x) between the contacts. Thus it is anticipated that the affect of charge accumulation at the upstream built in potential, or barrier, is mitigated as the barrier is pulled down below the emitter energy. When, the carriers reach the first barrier they are subject to the same constraints as under zero bias conditions, and Q remains positive prior to the upstream barrier and negative within the barrier. With regard to the magnitudes of Q, the increase in the numbers of carriers reaching the first barrier results in a disproportionate increase in electrons near the upstream barrier. When the increase is confined to the same or smaller distances, there is a consequent increase in Q. Increases in charge in the upstream barrier result in increases in charge tunneling through the first barrier into the well. **What happens to this excess charge?** Either it increases or decreases! In order for the charge to decrease as a function of bias, either the dwell time in the well must be relatively insensitive to bias, or the tunnel time through the second barrier must decrease with increasing bias. Because of the small potential difference across the first and second barriers the tunnel times are approximately the same. Further independent analytical calculations demonstrate that as resonance is approached the dwell times increases. Thus it is anticipated that the charge density in the well increases as a function of bias. This is seen numerically.

If the increase in charge is confined to the well Q must increase! When its value approaches that of the energy for classical transmission resonance, a condition of resonance exists, where the charge density in the well displays a half integral number of wavelengths (with suitable phase adjustments), a condition of resonance exists (see equation 47b). The point to be emphasized is that as the bias is increased the density of carriers in the quantum well increases. This is the point emphasized by Rico and Azbel [16]. The detailed calculations indicate this.

III.b The Distribution of Velocity

The charge distribution under equilibrium conditions for the structure discussed in
the above paragraphs is shown in figure 2. Note the small local accumulation layer in the
center. As discussed in the above paragraphs the density in the quantum well increases with
increasing bias. Now current continuity requires that local increases in charge are
accompanied by local decreases in mean velocity, and vice versa. It is found that at low
values of bias the average time spent in the well, defined as $L/<v>$, where L is the width of
the well, and $<v>$ is the mean velocity in the well, varies at low values of bias from 10fs, to
approximately 500fs at bias levels in the region of negative differential resistance. Indeed,
the calculations suggest that it is the significantly reduced velocity at resonance that is
responsible for NDR. Now the time spent in the well has been referred to as the dwell
time. The concept of a dwell time should be confined to those situations where the RTD is
part of a transient experiment. For calculations, such as that discussed here, carriers are
continually being replaced by carriers from the contacts, and so transit time is likely to be a
more appropriate description. which as as discussed by others is accompanied by an
increase in the amount of time spent in the well. In the calculations performed below the
dwell time, as this is sometimes referred to is not calculated. Rather the mean velocity is
calculated. It is found that the mean velocity in the well decreases as resonance is reached.

Since current continuity constrains all of the results of this study, the transition from the
quantum well to the downstream barrier is accompanied by a substantial decrease in carrier
density and a corresponding increase in mean velocity. While an integration of this has not
been performed simple estimates indicate that the integrated charge in the structure
decreases in the NDR region, with most of the decrease occuring in the downstream barrier
and the region between the downstream barrier and the collector contact. Now there will
be scattering events that will limit the value the velocity will attain. Very recent calculations
where numerical inaccuracies were significantly reduced, suggest that the most significant
number of scattering events occur in the downstream barrier. This last conclusion is similar
to that of Luryi [9].

III.c The Quasi-Fermi Level and the Electron Energy Distribution

The quasi-Fermi level is treated here as a mathematical concept. Under equilibrium
conditions the quasi-Fermi level is constant. It is set to zero in our calculations. For a
structure with a long low doped spacer layer, the equilibrium conduction band energy
distribution is displayed in figure 2. At the contacts the density is high and the conduction
band energy is below the quasi-Fermi level E_f. For the case of the long spacer layers, the
equilibrium charge distribution is such that the conduction band energy exceeds that of the
E_f, thereby introducing a barrier and a consequent low value of current due to tunneling.
At high bias levels carriers can be thermionically emitted over the barrier associated with
the built-in potential. How are both these profiles expected to change as the bias is
changed?

First we note that because the conduction band energy is governed by Poisson's equation
throughout the entire structure, the conduction band energy undergoes very smooth
variations between the emitter and collector contacts. Thus as a function of bias the
potential diagram in figure 2 will be tilted. The quasi-Fermi energy, which is governed by
distribution of a carriers at each point in the structure undergoes a severe variation. From
the emitter to the first barrier, where there is substantial charge accumulation the Fermi
energy is near zero. The Fermi energy begins to track the conduction band energy smoothly
as it goes through the well, but now begins to assume values below $E(x)$, as it should.
Finally, at the collector is reached the fermi energy increases above $E(x)$. This crossover is
a universal feature of the calculations, as it should be. The interesting feature is that as

resonance is approached the charge in the second barrier decreases precipitously, and the Fermi energy drops significantly below the energy of the conduction band. (One deficiency in the present formulation is that there is no mechanism for constraining the value of Fermi-energy by the band gap of the material.) These features will be illustrated below.

III.d The Voltage at Resonance

We can now ask when resonance will occur. In terms of equation (46), the simplest picture is given near absolute zero, where conditions associated with the built in potential are not an issue. In this case equation (46) teaches that resonance will occur when the quasi bound state as determined by a half-integral number of wave lengths crosses the Fermi energy. **Calculations at 4.2K for a 40/50/40 AlGaAs-GaAs RTD confirm this result.** At 4.2K where where the effect of the quantum distribution function is less pronounced this occurs at a bias that is approximately equal to $2(E_f - E_0)$ where E_0 is the energy of the resonant state. The factor of '2' is a consequence of the potential drop across the rest of the structure. This, of course, is the standard argument for resonance. **The moment balance equations indicate something additional, namely that the position of resonance is also influenced by the detailed particle distribution function in the well and barrier.** For example, if we assume Boltzmann statistics and the density of particles in the well is below the conduction band density of states, then resonance, which is governed by single particle effects, should occur at extrinsic voltage levels significantly lower than that in which statistics is ignored. If the statistics is governed, by e.g., equation (42b) resonance should occur at values much higher than that where statistics is ignored. This was also observed. The equations also indicate that resonance when space charge effects are included can also be sustained for a finite range of bias values. This feature does not emerge from any other study.

When will the current begin to decrease? Again, if $E_f = x_f = 0$, we should begin to see a departure from the peak current when the energy of the carriers in the well departs from resonance. In other words, the carrier energy increases. The presence of the space charge distribution in the RTD complicates matters. To see this we approximate equation 40 by time independent conditions, ignore spatial variations in the effective mass, and assume the scattering rate is constant. It is then a straight forward matter to demonstrate that the net velocity flux in the RTD is given by

$$ J = \rho v = - \frac{1}{\Gamma L} \int_0^L \frac{\rho}{m} \frac{\partial E_F}{\partial x} \, dx \tag{48} $$

As may be expected E_F undergoes its strongest position dependence at the second barrier, which is also where ρ exhibits its strongest depletion. Thus the results of equation 48 suggest that while the NDR region is a consequence of resonance and the very low velocities of the carriers, the structure of the current is likely to be determined by the net decrease in charge in the structure. Additionally, the above results suggest that NDR, while accompanied by a net decrease in charge, does not necessarily imply a decrease of charge in the well.

The results discussed above are dependent in a detailed manner on the quantum distribution function, whose form was assumed for the Phase I study. Thus, the presence of a charge distribution in the well that is governed by the logarithmic term could result in a decrease in current at a premature value of voltage. On the other hand, if x_f is always positive, there can be a delay in reaching the peak current. It is important to note that when space charge considerations enter, and there is, e.g., accumulation at the upstream barrier, a condition of resonance could occur arising from bound states in the accumulation layer.

III.e The Minimum in Current

When will there be a minimum in current? The argument here is direct. As the bias is increased and the condition of resonance is exceeded, the velocity in the barrier begins to increase. Thus increases in charge density within the well are now accompanied by increases in velocity and the current rises. Of course if the downstream barrier falls below the energy of the entering carriers the current will again rise, but this latter increase in not associated with tunneling.

IV. Numerical Approximations...Artificial Diffusion

In using the hydrodynamic approach to solving the quantum mechanical problem, Schrodinger's equation, which is a second order differential equation, is replaced by two first order differential equations. The numerical techniques used to solve the governing equations employ central difference approximations to the spatial derivatives appearing in the governing equations. Such a procedure generates a numerical scheme which is non-dissipative. As such, depending on the grid structure and the boundary conditions employed, spatial oscillations, or wiggles, in the solution may arise. These wiggles are usually associated with high frequency components which are present in the solution, but cannot be resolved by the local mesh. As a result, errors in the solution accumulate about the Nyquist frequency (wave length $2\Delta x$) and wiggles appear. To eliminate these wiggles, some form of spatial dissipation is typically introduced in the numerical scheme. The procedure followed here is to introduce numerical, or artificial diffusion based on gradient diffusion, into the governing continuity and momentum equation. This is a very common procedure, and results in the continuity equation, instead of being expressed as that given by equation (5) being given by the following equation, in one dimension:

$$\frac{\partial \rho}{\partial t} + \frac{\partial \rho v}{\partial x} - \frac{\partial}{\partial x}\left[D\,\frac{\partial \rho}{\partial x}\right] = 0 \tag{49}$$

where $D = v\Delta x/2$. Here Δx is the spatial increment in the calculation. Obviously, the introduction of artifical diffusion into the continuity equation reduces the formal accuracy of the difference approximation from $O(\Delta x^2)$ to $O(\Delta x)$. Similarly, as in the case of the continuity equation, artifical diffusion is introduced into the momentum equation as follows:

$$\frac{\partial \rho v}{\partial t} + \frac{\partial \rho v^2}{\partial x} = -\frac{\rho}{m}\left[\frac{\partial E_f}{\partial x} - \left(\frac{\rho v^2}{2} - \frac{NkTF_3/2}{\rho}\right)\frac{1}{m}\frac{\partial m}{\partial x}\right]$$
$$- \rho v\Gamma + \frac{\partial}{\partial x}\left[D\frac{\partial v}{\partial x}\right] \tag{50}$$

where the diffusion term in equation (50) is given by $D = \rho v\Delta x/2$. Thus the relevant balance equations used in the study are equations (49) and (50). In addition, all studies for finite bias use as initial conditions the solution to the equilibrium solution. This occurs for $\rho v = 0$. From equation (50), we obtain:

$$0 = -\frac{\rho}{m}\left[\frac{\partial (E+Q)}{\partial x} + \left(\frac{NkTF_3/2}{\rho}\right)\frac{1}{m}\frac{\partial m}{\partial x}\right] - \frac{2}{3m}\frac{\partial NkTF_3/2}{\partial x} \tag{51}$$

-15-

V. Applications and Results

Va. Structure of a Typical Device

Most of the structures studied in this report are described in figure 3 and table II. An additional asymmetrically doped structure was also examined. In this structure the RTD and two cladding layers, each of which are 50A wide, are nominally undoped at $5x10^{14}cm^{-3}$. The doping in the remaining part of the middle region of the structure was taken as either as $10^{16}cm^{-3}$ (type I device) or as $5x10^{14}cm^{-3}$ (type II device). The low doped region is then sandwiched between two heavily doped contacts ($2x10^{18}cm^{-3}$) where the carrier concentration is assumed to reach its equilibrium at the two end points of the device simulation. There is also one asymmetric simulation. The presence of undoped cladding layers helps to reduce the migration of impurities from the more heavily doped regions. Impurities could partially destroy the phase coherence of typical RTD and reduce the size of the PVR observed experimentally. Another reason for introducing spacer layers is to keep a greater degree of symmetry of the overall structure since an applied bias would be dropped over a longer, undoped region. As Ricco and Azbel pointed out [16], asymmetry in the conduction band profile degrades the peak in transmission through the RTD, thereby reducing the resonant tunneling through the structure.

The RTD itself is modeled has shown in figure 3b. To avoid numerical problems connected with sharp interfaces, a typical RTD is taken as trapezoidal in shape, the consequences of which are marginal as will be discussed later. Because comparison to earlier studies will be made, it is important to review the Tsu-Esaki and Luryi, formalism to describe RTD's.

Vb. Current-voltage characteristics in previous formalisms

There have been several calculations [10-14] of current-voltage characteristics of RTD's following the pioneering work of Tsu and Esaki [8]. In this approach, two major assumptions are made:

1. The total device length is assumed to be short enough (or the mean-free path long enough) that electrons can traverse the device without scattering (elastic or inelastic). This is the so-called assumption of ballistic transport. As discussed earlier, and also more recently by Landauer [16b], this assumption is incomplete. **Further, for consistency it may be necessary to include scattering in the interior of the device.**

2. The contacts at each end of the device are in local thermodynamic equilibrium, launching electrons into the device with a spectrum of wavevectors, weighted according to Fermi-Dirac statistics.

The Tsu-Esaki approach, is different from ours since it is based on an individual electron picture whereas our approach, while dominated by 'single particle' contributions, is more global, treating the total gas of electrons flowing from the contacts in a "hydrodynamic" picture, i.e., using the moment-equations of the density matrix equation. In the Tsu-Esaki's picture the occurrence of NDR in the current-voltage characteristics of typical RTD's is explained as follows:

In a typical RTD, there exists one (or several) quasi-bound state(s) E_0 (as shown in figure (4)) due to the quantum confinement of the two-dimensional electron gas in the well. When a small dc voltage is applied across the structure, the metastable resonance state (E_0) is not low enough to let sufficient numbers of electrons with Fermi energy in the left contact flow through the structure and only a small current flows through the RTD. Increases in

bias result in increases in current and it is generally believed that the peak current occurs when the quasi-bound state lines up with the Fermi energy of the emitter (see figure 4):

$$V_{ndr} \simeq 2[E_0 - E_f]/e \qquad (52)$$

where the factor of 2 occurs because it is <u>assumed</u> that the bottom of the well shifts by one-half of the applied voltage. Estimates of the NDR position in the Tsu-Esaki formalism are given for the structures studied here in Table III.

An alternative argument offered by Luryi [9] indicates that the current begins to increase from zero at the above value of voltage, which is then referred to as

$$V_{th} \simeq 2[E_0 - E_f]/e \qquad (53)$$

and peaks at

$$V_{ndr} \simeq 2[E_0 - E_c]/e \qquad (54)$$

where E_c is the bottom of the conduction band at the emitter contact.

As discussed by Tsui et al [16c, 16d] the situation becomes more complicated when an accumulation layer exists at the emitter barrier and a depletion layer exists at the collector barrier. In the former the accumulation layer lowers the conduction band edge in the emitter closer to the barrier, thus lowering the peak-voltage or threshold voltage; the second shows the tendancy to raise the threshold voltage at the barrier.

Each of the above features along with the contributions of statistics may be assessed within the framework of the hydrodynamic approach, some of which were accounted for during this Phase I study. Note in the hydrodynamic approach, the mean energy used in calculating the resonant energy includes a contribution from x_f.

From the above discussion, an important parameter to determine is the actual of the quasi-bound state and it's value for a given RTD geometry. This is discussed next.

Vc. Location of the Quasi-bound state

In order to facilitate the discussion of the position of the quasi-bound state in the well, which is determined self-consistently in the hydrodynamic calculation, but is a separate calculation in all other approaches, we have supplemented our study with calculations of the transmission coefficient using transfer matrix methods. This was implemented for a perfectly symmetric resonant tunneling structure such as the one shown in figure 3. This technique has been widely used in the past to calculate the current-voltage characteristics of resonant tunneling structures [10,11,12]. Figure 5a shows the transmission coefficient versus total energy of the electron incident from either side of the resonant tunneling structure for the case of zero bias. The situation under finite bias is shown in figure 5b. In figure 5a we show for comparison the transmission coefficient versus energy in two cases: (1) the effective mass throughout the entire structure is constant and equal to the GaAs effective mass $m^* = 0.067m_0$;(2) the effective mass is spatially and equal to $m^* = 0.092m_0$ in the $Al_xGa_{1-x}As$ barriers which corresponds to an Al concentration $x = 0.3$.

The transmission coefficient reaches unity when the energy of the incident electron perfectly matches the energy of the quasi-bound state in the well. As can be seen from figure 5a, the energy of the quasi-bound state is actually lower when the effective-mass variation with position is taken into account. Also, the transmission coefficient no longer reaches unity under non zero bias condition. For high current density levels, asymmetric

barriers would then be preferable to keep the transmission coefficient (and therefore the current) through the RTD as high as possible once it is under bias [16]. This point will be discussed in more detail below.

In the figure 5b calculation the applied voltage is distributed linearly across the two barriers and the well, and so the downward shift in the resonance level is relative to the applied voltage.

In figure 5c, the bias dependent calculation is repeated for a higher barrier height. The quasi-bound state is higher in energy, and the width of the transmission peak at half-maximum is smaller, for the higher barrier.

In our numerical simulations, the resonant tunneling structure was assumed to have a trapezoidal rather than perfectly rectangular shape (see figure 3b). The trapezoidal approximation was taken to avoid numerical problems in the actual calculation of the quantum potential across sharp interfaces. (In practice, the interfaces between GaAs, and AlGaAs layers are never perfectly sharp and a trapezoidal approximation might actually be closer to the actual shape of resonant tunneling devices grown by MBE or MOCVD.)

Replacing the rectangular barriers by trapezoidal ones with relatively steep walls has little effect on the position of the quasi-bound state in the well. This was checked by using the transfer matrix technique to derive the transmission through a perfectly rectangular resonant tunneling structure and its "trapezoidal" approximation. The transmission coefficients through the two structures are shown in figure 6a and 6b for comparison. Little difference is seen between the two curves. The same is true when the structure is under bias although not shown below.

The position of the quasi-bound state in the well is also a function of well width. We show in figure 7 the transmission coefficient versus energy for three resonant tunneling devices with different well thicknesses (devices #2, 3, 4 of Table II). As can be seen from figure 7, the quasi-bound state position is lower for wider wells while keeping all other parameters of the RTD the same. Typically, the position of the quasi-bound states have been used to infer the position of the negative differential region of the RTD's. While, we do this below, it will be demonstrated by the simulations of this study that this procedure is sometimes misleading.

VI. Numerical Examples

VIa. Type I, Device #1

The first set of calculations is for the type I structure with a barrier of 30A and a well width of 50A. The equilibrium distribution was discussed earlier and displayed in figure 2. Recall, for this calculation, the quasi-Fermi level is constant throughout the structure and arbitrarily set to the value zero. The equilibrium charge density shows a small peak in the center of the structure (figure 2a). The quantum potential is shown in figure 2b. Note that its peak values occur at the peak values of the conduction band profile, shown in figure 2c. The offset in potential in the structure is a consequence of the low density in the quantum well and implies that Boltzmann statistics prevails. In this calculation the quantum potential has a peak value within the well of approximately 0.031 eV.

Note that the solutions are symmetric, that the small excess peak charge within the well, is consistent with the single particle nature of the solution. Also, as a result of the low doping concentration in the middle of the structure, the conduction band energy profile is higher in that region. The detailed calculation indicates that the conduction band in the

center of the well is approximately 7mv above the fermi energy at the emitter. The quasi bound state for this structure is approximately 57mv. Thus according to the Tsu-Esaki formula the peak current should occur at 0.128mv, whereas the current-voltage curve for this structure shows a peak current between 0.06 and 0.08v, as shown in figure 8.

What are the origins of the above differences? To examine this we look at the variation of conduction band energy $E(x)$, space charge $\rho(x)$, and quantum potential $Q(x)$ as a function of bias, as displayed in figure 9. The conduction band energy shows the expected tilt as the bias is increased. The distribution of energy is such that at a bias of 0.1v, approximately 20% of the voltage drop falls across the upstream accumulation layer, 30% across the double barrier plus well, and 50% downstream from the second barrier. Within the framework of Tsu-Esaki, the large voltage drop across the upstream accumulation layer tends to lower the voltage at which the peak current occurs, while the large voltage across the downstream region tends to increase the voltage at which the peak current occurs. Thus within the framework ot Tsu-Esaki it is not clear whether the calculations for this structure should peak at voltages above or below that at which they occured.

The charge distribution for this structure is bias dependent; with several key features. As seen in figure 9b, there is a region of charge accumulation upstream of the barrier that increases with increasing bias. The charge in the well continues to increase with increasing bias. In most of our numerical examples the bias dependence of the charge density profile shows the general trend reproduced in figure 9b. We notice an important charge accumulation inside the well which keeps increasing when the applied bias increases. The charge density within the first barrier is small at low values of bias. This is concomitant with large values of the quantum potential in the same region. As can be seen from eq. (7), the large value of the quantum-potential prevents the electron from moving through the second barrier and forces them to pile up in the quantum well. For larger values of bias, the strength of the quantum potential gradually decreases through the second barrier and the charge density starts increasing in that region (figure 9c).

In all our numerical simulations, including those of figure 9 we notice the formation of a depletion layer downstream of the second barrier once we pass the valley current of the I-V characteristic. This depletion layer is a specific single particle quantum effect. The depletion layer keeps on extending for biases greater than the voltage at the valley of the I-V curve until the depletion layer touches the heavily doped region (210^{18}cm^{-3}). Then, the electron density downstream of the second barrier gradually increases and the depletion region disappears. For the range of biases for which the depletion is formed, the electrons piling up in the resonant tunneling will feel an important electric field downstream of the second barrier. This stresses the importance of the doping profile and concentration on the right-side of the second barrier.

The above discussion has concentrated on carrier density rather than velocity. Figure 9d displays the general velocity trend seen in all of our calculations. The low average velocity in the well in contrast to the very high average velocity in the barrier reflects the fact that the electron spends more time in the well than in the barrier. Correspondingly, the charge density in the well is more prominent than in the barriers. The average velocity is always large in the depletion region after the second barrier. Indeed, very recent calculations in which numercial error was significantly reduced, displayed very high velocities in the second barrier. These velocities were limited in value by scattering; a result consistent with the proposal by Luryi [9]. This fast sweep of electrons after crossing the RTD is desirable for fast-switching applications of the device. The average velocity is bigger than the saturation velocity in GaAs ($\approx 0.8\times10^{7}$cm/s) for large values of bias in the depletion region. This situation is possible since it occurs on relatively small distances ($<$500A). We also note that the average velocity quickly drops back to a minimum while approaching the right-hand

side heavily doped region. But most significantly, the velocity in the well under conditions of resonance, shows a steady decrease with increasing bias. For example in one set of calculations, prior to resonance the mean velocity in the well led to a nominal transit time of 10fs. At resonance, the nominal transit time was increased to 500fs!

While the mean velocity for this structure, shows the expected increase in velocity in the downstream barrier where the charge density is reduced to extremely low values (see figure 9d); and the carrier velocity in the well begins to drop near the peak current, how can we be certain that we are near resonance? In figure 9c the bias dependence of the quantum potential is plotted. It is our observation that when the value of Q approaches the resonant energy level that the mean carrier velocity decreases. Further, the bias value at which Q approaches resonance is dependent upon the value of charge in the well, as reflected in the quantum distribution function, through the term x_f.

Thus peak currents can occur at voltage levels below that predicted by Tsu-Esaki. Further the distribution of carriers in the well increases with increasing bias, which is shown in figure 9b. We note once again, however than at 4.2K, where the effect of the x_f is reduced the voltage at peak current occurs at values close to that predicted by Tsu-Esaki. The voltage at which the current peaks appears to be strongly model dependent and should be a cornerstone of any Phase II study.

The quantum potential is displayed in figure 9c. If we concentrate on its value in the well, the most dramatic point to note is that as the bias is raised the value of the quantum potential tends to cluster around a narrow range, increasing in magnitude from the upstream barrier to the downstream barrier. These values are given in the table below, at a value in the center of the structure:

V:	.01	.02	.04	.06	.08	.10	.11	.12	.14	.16	.20
Q:		.020	.029	.044	.049	.053	.054	.055	.056	.057	.058	.059
<k>L	0.94	1.13	1.39	1.47	1.53	1.54	1.55	1.57	1.58	1.60	1.61

The first point to note about the table is that for a bias of approximately 0.06 to 0.08 volts we are approaching the classical condition for transmission resonance within the well. And at these values we are approaching the peak current level. Indeed, as shown in figure 8, the peak current for this structure occurs at bias of between 0.06 and 0.08. **This result when coupled to the fact that the values of < k > L approach resonance, indicates that the characteristics are dominated by the single particle wave nature of the equation.**

To supplement the discussion of the space charge profiles it is useful to plot the quasi-Fermi level in the RTD, recognizing that the quasi-Fermi level is not a physical quantity, but rather a mathematical transformation between charge density and energy (see fig. 9e). The plots stress the strong position dependence of the quasi-fermi level in the immediate vicinity of the resonant tunneling structure for different values of bias. Outside the double barrier structure, the quasi-Fermi level is nearly constant and equal to its value in the respective contact. This is an important difference with previous treatments of double barrier structures where, under the assumption of ballistic transport, the quasi Fermi level for electrons impinging from the contacts are assumed to be constant throughout the entire double barrier region. However, we are aware that the variation of the quasi-Fermi level, such as derived from equation (42a, b), is not rigorous. Indeed, equation (42a,b) implicitly assumes that thermal equilibrium has been reached throughout

the entire structure. We also note that E_f-E_c must have a constraint that it not exceed a material constant, e.g. $E_g/2$. To include this will require the constraint of the energy balance equation.

The results for this device are that the peak to valley ratio is small and that the voltage at peak current is below that predicted by the Tsu-Esaki formalism. In this context it is worthwhile digressing to consider the PVR in the context of wavepackets. Consider a double barrier structure with a transmission peak at an energy E_r. Assume that the transmission at E_r has a spread of Γ_r at FWHM. Further assume that a 'minimum' wavepacket was propagating at a momentum k_r corresponding to the resonant resonant energy, and that the spread in energy of the wavepacket at FWHM is Γ_w. If $\Gamma_w < < \Gamma_r$, it may be anticipated that most of the wavepacket will get through. If $\Gamma_w > > \Gamma_r$, only a small portion of the wavepacket is expected to be transmitted. In the former case it is expected that a large PVR is possible, whereas in the latter case a smaller PVR is likely. For the situation where $\Gamma_w > > \Gamma_r$ it is also possible that for wavepackets with propagating momentum that differs from k_r, that there may be portions of the wavepacket that will be transmitted through the resonant level. The situation with respect to the time independent solutions displayed here is unclear. The solutions obtained are for mean density and mean velocity. The Fourier decomposition of density will necessarily peak at values of wavelength that are characteristic of the number of wavelengths that fit into the well. The relationship between the spread in significant wavelenghts, the width of the resonant level and the PVR has not been determined, but should form part of the Phase II study. It is anticipated that if if the spread in wavenumbers, associated with the spread in wavelengths is much greater than Γ_r than the PVR will be small.

VIb. Type I, Device # 2

The above calculations were for a structure with a 30A barrier and 50A wells. What happens when the width of the barrier is increased to 40A? We first display a calculation of the transmission curves for the 30A and 40A barriers (see figure 10). Figure 10 illustrates that the width of the transmission peak through RTD's with thinner barriers is broader than that of the thicker barrier. From the same figure, we also notice that the position of the quasi-bound state is not very much affected by the barrier width. Since the width of the quasi-bound state is broader for thinner barriers, we expect the current level to be higher in the RTD with the smaller barrier. This is indeed the trend observed in our numerical examples.

The situation where the barrier width is increased to 40A is tabulated below:

V:	.01	.02	.04	.06	.08	.10	.11	.12	.14	.16	.20
Q:	.032	.039	.050	.055	.057	.059	.060	.060	.061	.062	.062
$\langle k \rangle$L	1.19	1.30	1.48	1.55	1.58	1.61	1.62	1.62	1.64	1.65	1.65

The broad charge distribution for this case is similar to the diode with the 30A barrier. Of course the current level is lower, (compare figures 8 and 11) because of the larger barrier; but the voltage at peak current is approximately the same. The important point to note here is that the resonance occurs at a higher value of mean Q for the wider barrier than for the 30A barrier. But the zero bias quasi-bound state is also higher in energy for the 40A barrier.

VIc. Type I Device #3 and #4

In order to investigate the effect of well width on the properties of the RTD, two types of calculations were performed. In the first, the well width was reduced to 30A, and in the second, the well width was increased to 70A. The current-voltage characteristics of these structures are shown in figures 12 and 13 respectively. In the first, at a given value of bias the mean Q values in the well were higher than that for the 50A well. This was expected, as the position of quasi-bound state increases in energy when the well width is reduced. The results however show negative conductance at values of bias that are only marginally above that obtained for the wider well, and for Q values below that expected for resonance. The distribution of charge while qualitatively similar to that for device #1 is significantly smaller in value at comparable bias levels. The carrier velocity in the well shows a decrease on the resonance is approached. Indeed, it was expected that resonance would occur for mean well widths near 0.08v or 0.09v. This situation requires further analysis. The situation for the well width of 70A, yielded low Q values, and a very small negative conductance was not seen. In fact, the traversal time for electrons is obviously larger for structures with thicker wells; a smaller peak-to-valley should therefore be expected in those structures since the scattering mechanisms are more effective in increasing the valley current (while destroying the phase coherence of electrons in the well). In the table below, the values $<k>L$ were obtained by assuming a well width of 35A.

V:	.01	.02	.03	.04	.06	.08	.10	.12	.14	.16	.18
Q:	.028	.038	.048	.053	.057	.060	.063	.065	.068	.070	.072
$<k>L$	0.78	0.90	1.02	1.07	1.11	1.14	1.16	1.18	1.21	1.23	1.25

Experimentally, there has only been one systematic study of the dependence of resonant tunneling current on well widths in AlAs/GaAs/AlAs double barrier diode structures [17]. In those structures, where the well width is increased, the resonant tunneling is found to be reduced because the increase in the well width lowers the resonant levels, increases the effective barrier height, and results in a sharpening of the transmission coefficient around the resonance peak (or equivalently, the decrease of the resonant level widths). A comparison to this work should be performed as part of a Phase II study.

VId. Type I, Device #5 with higher barriers (0.318 ev)

Having established that a condition of resonance exists, is it possible, for a specific cladding distribution to control the voltage at which the resonance condition occurs. A calculation was performed for a structure with a large barrier, 0.318v, and with no variation in the effective mass. (A comparison of calculations with and without a spatial variation in the effective mass, shows that the differences lie in a lower current level when the mass varies. The voltage at peak current is essentially unaltered.) In addition, the doped $5x10^{16}/cm^3$, regions were extended an additional 50 A into the structure. The presence of the increased barrier height results in an increase in the quasi-bound state energy, and an increase in Q at resonance. The result is an increase in the voltage at peak current, although the current levels are lower than that of the comparable figure 11 curve; with the differences arising from the increased barrier height. The tabulated mean values are given below, while the current-voltage relation is displayed in figure 14.

V:	.01	.02	.04	.06	.08	.10	.11	.12	.14	.16	.20
Q:	.039	.043	.060	.068	.073	.076	.077	.078	.081	.081	.083
$\langle k\rangle$L	1.31	1.37	1.62	1.72	1.79	1.82	1.83	1.85	1.88	1.88	1.91

VIe. Type II, Device #6

The calculations for the above two tables are qualitatively similar, with resonances occuring at the same conditions within the well. The situation when the 5×10^{16}/cm^3 are removed from the structure leads to different results. First, it must be noted that the effect of eliminating the more heavily doped cladding layer, will reduce the concentration of carriers in the well, and as seen in figure (16a), where we note that while there is local accumulation within the well, it is not nearly as strong as that for figure (9b). There is another difference. There is a larger potential drop across the region upstream and downstream of the well (figure 16b); as a result there is not as significant a voltage tilt within the well as for the structures associated with figure 9. The quantum potential is displayed in figure 16c and shows the same structure as that of earlier calculations. The mean velocity is shown in figure 16d, and displays the precipitous drop in value under conditions for resonance. The important difference occurs with respect to the voltage at which the peak in current occurs; here it is at approximately 0.03 volts, which is a factor of two smaller than that discussed above. The contribution again indicates that the premature resonance arises because of the contribution of x_f in the interior of the structure. Nevertheless as the table below demonstrates, the condition for resonance is similar.

V:	.01	.02	.04	.06	.08	.10	.11	.12	.14	.16	.20
Q:	.033	.041	.047	.050	.052	.053		.054	.056	.057	
$\langle k\rangle$L	1.20	1.34	1.43	1.48	1.51	1.52		1.54	1.57	1.58	

The current voltage characteristic for the above data is displayed in figure 15, where we see that the extended spacer layer reduces the number of carriers available for tunnelling and thus reduces the current level .

Because the calculations for this structure show a very small amount of charge accumulation at low bias levels, this structure was studied for different and arbitrary values of x_f to determine the efficacy of the argument that the properties of the pressure gradient have a determining influence on the characteristics of the device. In one such calculation x_f was arbitrarily altered such that, with reference to equation 42, for values of $x_f < 4.4426$, the logarithm contribution was ignored. It was found that the quantum potential in the well fairly well tracked the variation of $E(x)$ and that the condition for resonance was not reached until the bias reached 0.25 volts. At this point there was the quasi bound state crossed the Fermi energy and there was a substantial flow of current as predicted by Luryi [9]. A drop in current was not observed.

VIf. Effects of Asymmetric Barriers on Resonant Tunneling Current

In this paragraph, we discuss asymmetric resonant tunneling structures. In all experimental situations, any RTD is never perfectly symmetric. This lack of symmetry is related to the control of growth conditions and is always present. We are interested in the actual case where an asymmetric RTD is grown either by changing the thickness of the barriers or their heights. Numerical I-V calculations based on the "Tsu-Esaki" formulation [8] have suggested that the resonance effect and the negative differential resistance characteristics can be substantially improved in the resonant tunneling diodes with a high-low asymmetric barrier configuration [17,18].

We performed similar calculations using our approach for the structure shown in the inset of figures 16 and 17 The resonant tunneling device was chosen to have the configuration $Al_{0.3}Ga_{0.7}As/GaAs/Al_{0.45}Ga_{0.45}As$. The thickness of the well and the two barriers were chosen to be 50A and 40A respectively. Note, once again we took the Al concentration x in both barriers lower than 0.45. Beyond this value, one encounters the controversial issues of multivalley transfer [19] and phonon scattering involved in the conversation of momentum.

For the asymmetric structure we see an expected rectification (compare the forward and reversed I-V curves on figures 17 and 18). Of interest here is the broad plateau in current for the higher anode barrier, and the presence of a low-voltage negative conductance for the low barrier height anode. The space charge distributions for this case are shown in figures (19a and 20a) and show significant differences. First consider the high anode barrier. For the high anode barrier there is more significant depletion within the second barrier as well as downstream from the second barrier. The charge in the well is lower for the high cathode barrier at all values of bias. Of these fewer carriers in the well a larger percentage tunnel through the second barrier. The energy distribution for the two structures is shown in figures 19b and 20b. Recall that Poisson's equation is determined by the difference between the mobile density and background. In both cases the mobile concentration within and downstream barrier of the second barrier are much smaller than background, and so Poisson's equation yields similar results.

The values of the quantum potential are displayed in figures 19c and 20c. For the high anode barrier the mean Q values are distributed as follows:

V:	.01	.02	.04	.06	.08	.10	.11	.12	.14	.16	.20
Q:	.044	.048	.053	.057	.060	.062		.064	.065	.066	.068
$<k>L$	1.39	1.45	1.53	1.58	1.62	1.65		1.68	1.69	1.70	1.73

The above values are consistent with the results discussed earlier for all type I devices. For the situation where the barriers are reversed we see an unusual trend, one where the mean Q values decrease at low values of bias. The detailed space charge profiles shown that this decrease is accompanied by a decrease in space charge in the well, as some of the type II devices display. This is not resonant behavior.

V:	.01	.02	.04	.06	.08	.10	.11	.12	.14	.16	.20
Q:	.038	.025	.024	.063	.065	.067		.068	.068	.068	.068
<k>L	1.29	1.05	1.03	1.66	1.69	1.72		1.73	1.73	1.73	1.73

For an asymmetric structure, one expects an increase in the peak-to-valley ratio (compared to the case of a perfectly symmetric structure; x = 0.3 for both barriers) since the valley current will be substantially reduced when one of the barrier height is higher. This results from the fact that a large component of the valley current is due to thermionic emission above the barriers and is therefore smaller in the case of asymmetric RTD. Though it is true that a further increase in the barrier height may lead to an even greater peak-to-valley current ratio, such an increase will, however, result in a rapid drop in the peak current that is not desirable for many practical purposes where current densities as high as 10^5 A cm^{-2} are needed. One important feature of the high-low resonant tunneling diode is the rectifying effect associated with the asymmetric I-V characteristics as seen in figures 17a) and 18). Applications of this effect are exploited in [17].

The above asymmetry in concentration and perhaps doping has recently been considered for interesting device applications [17,18]. A new device using quantum-well injection and transit-time effects, the QWITT diode, is shown on figure 20. The quantum mechanical tunneling in the QWITT diode is a low-noise injection mechanism with superior high frequency characteristics. In ref. [17], it was shown that the length of the transit-time region (see figure 21) could be optimized to obtain the best power-frequency performance device superior to the rf performance of pure quantum well oscillators. The presence of a drift region (transit-time region) increases both the device impedance and optimum bias voltage so that higher output power can be obtained. On the other-hand, the quantum well offers the opportunity to control the phase of the injected carrier population, i.e., the injection phase angle, as a function of dc bias, a new feature for a transit-time device. To the best of our knowledge, our calculations are the first ones to actually show the formation of a depletion layer downstream of the second barrier. As stated above, this could have interesting device applications and our simulations might be quite useful in the future in better design of new device concepts, such as the QWITT structure.

VII. Conclusions

The calculations display several very distinct features. For most of the structures:

(1) The charge from the emitter tunnels through the first barrier into the well, and the amount of charge in the well increases with increasing bias.

(2) Resonance and NDR are single particle effects and are always accompanied by a decrease in velocity in the well, usually approximately a decrease of two orders of magnitude. This increased dwell time is accompanied by a significant decrease in tunneling through the second barrier, and a concomitant increase in velocity in the second barrier. Resonance occurs at mean values of $<Q>$ corresponding to the value of energy associated with unity tramsmission, although the values of $<Q>$ are not calculated from the scattering matrix.

(3) Excessive increases in velocity in the second barrier **must** be accompanied by either elastic and/or inelastic scattering to prevent the mean velocity from reaching unrealistically high values.

(4) The detailed charge distribution and current voltage relationships are sensitively dependent on the properties of the cladding layers.

(5) At resonance estimates of the mena charge density show $<\rho>$ decreasing with increasing bias under resonance.

(6) The current voltage relationships exhibit peak-to-valley ratios which are smaller than the experimental values. However, for a device with a cross-section of 25μm x 25μm (which is a typical experimental cross-section), the peak-current calculated numerically are of the order of 0.2-20 mA. This is the typical range of peak current of various RTD's studied experimentally [2,3,4,5,6,7]. The peak and current levels obtained in our numerical simulations have the right order of magnitude. Our peak-to-valley ratios are typically only a factor 2 to 4 lower than the experimental findings. This probably results from the following: (a) As discussed in section 2, a numerical simulations using the moments of the density matrix equation must include the energy balance equation. Energy balance is indeed an important issue in the presence of (inelastic scattering). The low peak to valley ratios are related to the inclusion of a relaxation term in the momentum balance equation. It has been shown experimentally that the presence of scattering in typical RTD (voluntary doped) could substantially reduced their peak-to-valley ratios [14,20].

A detailed investigation of the above conclusion must await a more complete investigation of the influence of the doping profile on the shape of the current-voltage characteristics of typical RTD. For instance, very recent calculations [20,21] making use of the Wigner distribution formalism have shown the importance of a better treatment of the contact regions in developing a full quantum kinetic theory of RTD's and of any system open with respect to electron (or holes). Also, in the single-particle Wigner distribution formalism, no attempt is made to specify a priori what states electrons occupy in the contacts (which are assumed to be scattering states in the Tsu-Esaki approach). In our approach, we do not identify the individual states occupied by those electrons launched from the contacts. Rather we adopt an hydrodynamic picture in which mean boundary properties are identified. we treat the overall gas of electrons at once. This striking difference between our model and the Tsu-Esaki's picture can partly explain why our peak-to-valley ratios are substantially lower than in the Tsu-Esaki formalism and in closer agreement with the peak-to-valley ratios obtained in the Wigner distribution formalism.

At this point, it is worth mentioning that the high peak-to-valley ratios obtained in the Tsu-Esaki formalism are somehow dependent on the assumed plane-wave eigenstates for the electrons impinging from the contacts. In ref. [22], it has been shown that while using wave-packets instead of idealized plane-wave representation, in the Tsu-Esaki formalism, the peak-to-valley ratios of typical RTD's are substantially reduced and in better agreement with the experimental results. In other words, the assumption of the plane-wave solutions for electrons coming from the contacts is somehow an idealistic situation.

(7) The peak current occurs at a rather small bias and its location is strongly dependent on the actual doping profile outside the resonant tunneling structure itself. The results are strongly dependent upon the details of the quantum distribution function, whose form was <u>assumed</u> rather than calculated.

(8) Our previous discussion has stressed the importance of a better treatment of the boundary problem linked to the flow of electrons from the contacts. On the other hand, it is now recognized that meaningful theoretical attempts to reproduce the current-voltage characteristics of typical RTD's must be self-consistent in nature, i.e., must include the space-charge effects through a solution of Poisson's equation. Quite recently [23], it has

been shown that, while performing self-consistent calculations, the calculated I-V characteristics show an intrinsic bistability in the negative-differential conductivity region of the curve. This intrinsic bistability results from charge storage and the subsequent shifting of the internal potential of the device. On the cathode side of the RTD, there is a formation of a deep triangular well (the depth of this well depends on the actual doping profile). This can lead to quantized electron states and a large accumulation of charge which reduces the barrier height to a ballistic electron injected from the cathode. This effect could enhance the valley current and thereby reduce the peak-to-valley ratio. Our hydrodynamic model allows for the electron population of the triangular well on the cathode side of the RTD. This is presumably one of the reasons why our peak-to-valley ratios are substantially lower than those usually calculated in the Tsu-Esaki's picture. A full investigation on the influence of the doping profile on the actual population of the triangular well is therefore of primary importance in the design of typical RTD. Our numerical simulations have shown that the position of the NDR also strongly depends on the actual doping profile in the device and thereby the actual population of the triangular well on the cathode side of the RTD. A full investigation of the precise control of the NDR shift must await further numerical simulations.

In conclusion, even though incomplete, our approach making use of the first two moment-equations of the density matrix equation has been shown to lead to occurence of a NDR region in typical resonant tunneling structures. Further work is needed to include the energy-balance equation in our model together with a more sophisticated treatment of scattering (both elastic and inelastic) in our formulation. When included, those refinements will allow us to distinguish between the possibilities of coherent and/or sequential tunneling in resonant tunneling structures, and be used as a powerful tool to design typical RTDs.

Au/Cr

	Overall structure		
100 nm	InGaAs	$2 \times 10^{19} cm^{-3}$	
100 nm	InGaAs	$2 \times 10^{19} cm^{-3}$	
100 nm	InGaAs	$2 \times 10^{17} cm^{-3}$	
100 nm	InGaAs	$2 \times 10^{17} cm^{-3}$	
400 nm	InGaAs	$2 \times 10^{19} cm^{-3}$	
	InP	$2 \times 10^{19} cm^{-3}$	

Overall structure

Tunnelling layers

InGaAs		5 a.l.
AlAs	S.L.	10 a.l.
InGaAs		3 a.l.
InAs	S.L.	6 a.l.
InGaAs		3 a.l.
AlAs	S.L.	10 a.l.
InGaAs		5 a.l.

(a)

E_{CB}
E_{W2}

Electron energy →

E_{W1}
0
E_f

Position →

$-E_{CW}$
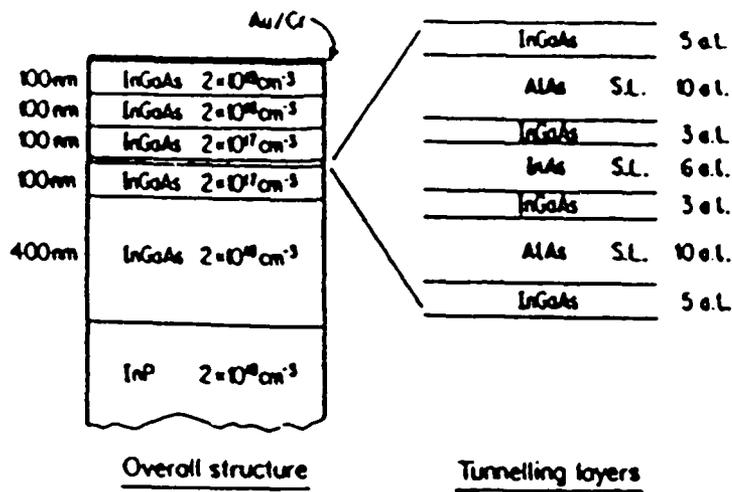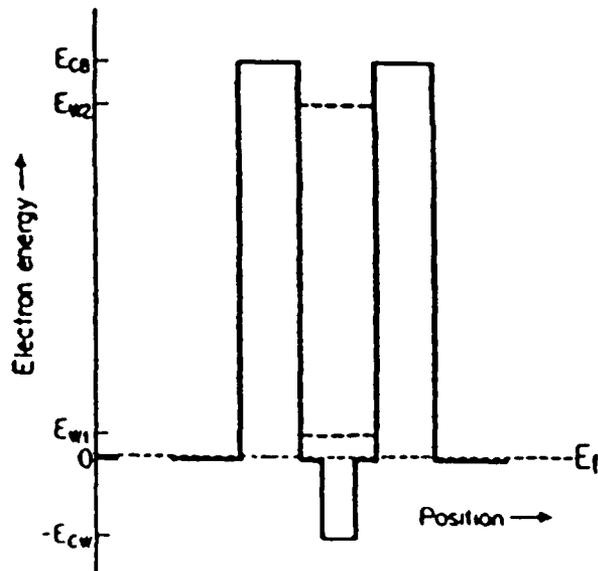
(b)

Figure 1: Pseudomorphic $In_{0.53} Ga_{0.47}$ As/AlAs/InAs resonant tunneling diodes proposed in Ref.[1]. Peak-to-valley current ratios as high as 30 at 300K and 63 at 77K were obtained with this structure.

GaAs/AlGaAS RTD

DATE	BARRIER	WELL	PEAK-TO-VALLEY RATIO	REFERENCE
JUNE 74	$Al_x Ga_{1-x}$ As x = 0.3 80 Å (MBE)	GaAs 50 Å	FIRST OBSERVATION OF NDR	#2
SEPT. 83	$Al_x Ga_{1-x}$ As x = 0.3 50 Å (MBE)	GaAs 50 Å	P.V.R. = 6 AT 25K	#3
FEB. 85	AlAs 42 Å (MOCVD)	GaAs 62 Å (MOCVD)	NDR AT TEMP. AS HIGH AS 260K. P.V.R. = 3.4 AT 4.2K	#4
JUNE 86	$Al_x Ga_{1-x}$ As x = 0.45 50 Å (MOCVD)	GaAs 50 Å	P.V.R. = 1.48 (300K) = 6 (77K)	#5
JULY 87	$Al_x Ga_{1-x}$ As 50 Å (MBE)	GaAs 50 Å	x = 0.3 P.V.R. = 2.2 (300K) = 7.0 (77K) x = 0.42 P.V.R. = 3.9 (300K) = 14.3 (77K)	#6
JUNE 88	AlAs 20 Å (MBE) Si SUBSTRATE	GaAs 56 Å	P.V.R. = 2.9 (300K) = 12.5 (77K)	#7

TABLE I: Evolution of peak-to-valley ratios since 1973. A brief overview.

a)

CHARGE DENSITY
$(2 \times 10^{18} cm^{-3})$

N_0

b)

QUANTUM POTENTIAL, (ev)

c)

TOTAL CONDUCTION
BAND PROFILE, (eV)

DISTANCE, $(\times 1000 \text{Å})$
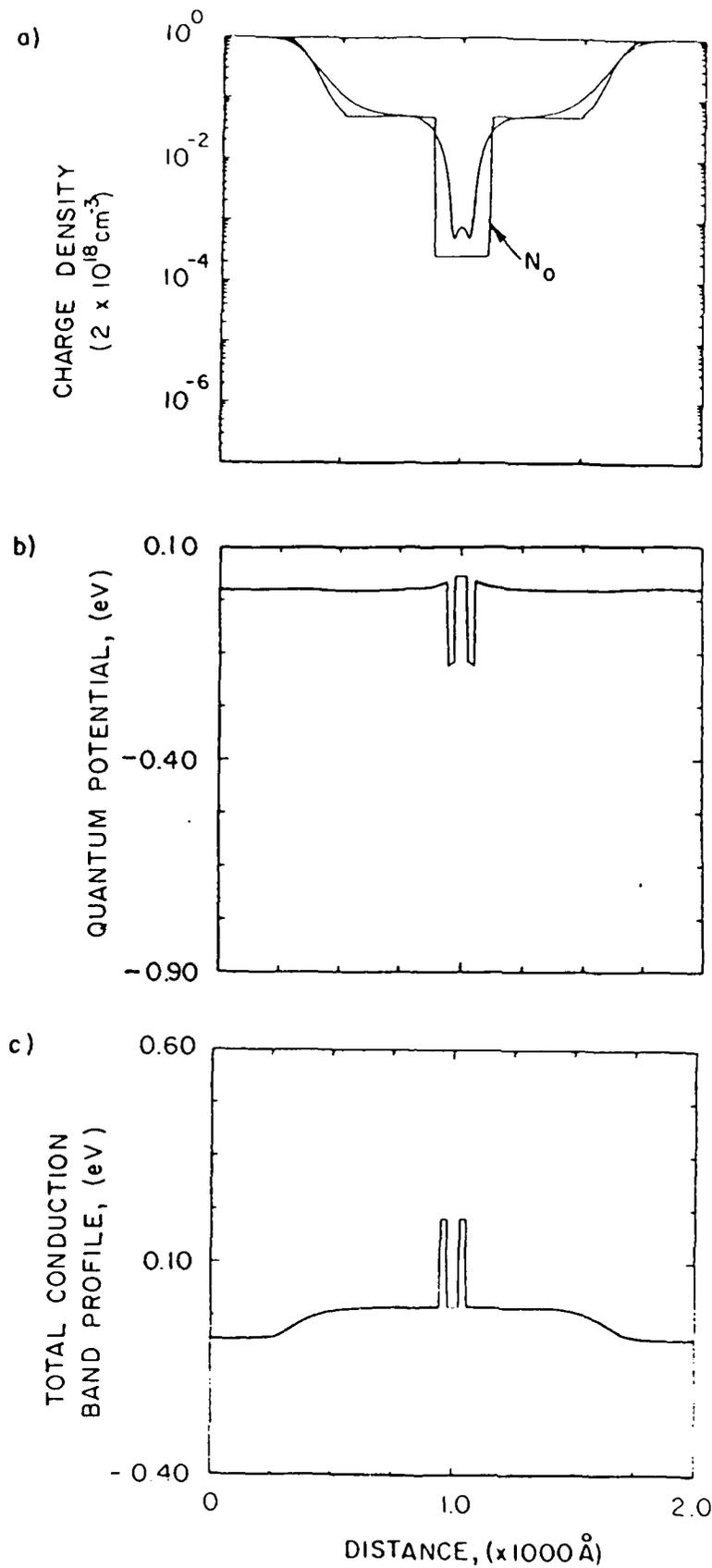
Figure 2: a) Charge density profile at equilibrium for device #1
of table II. N_0 is the doping profile (type I, see
fig. 2a). b) Quantum Potential, c) Conduction band
energy profile for the same structure. All calculations
performed at T = 77K.

DOPING	BARRIER (Å)	WELL (Å)	V_0 (eV)	V_1 (eV)	DEVICE
TYPE I	30	50	0.209	0.209	#1
	40	50	0.209	0.209	#2
	40	30	0.209	0.209	#3
	40	70	0.209	0.209	#4
	40	50	0.310	0.310	#5
TYPE II	40	50	0.209	0.209	#6
TYPE I (ASYMMETRIC) RTD	40	50	0.209	0.318	#7
	40	50	0.318	0.209	#8

TYPE I AND II REFER TO THE DOPING CONCENTRATIONS SHOWN IN FIGURE 2. BOTH WELLS ARE ASSUMED TO HAVE IDENTICAL WIDTH. V_0,V_1 ARE THE BARRIER HEIGHTS OF THE LEFT AND RIGHT BARRIER RESPECTIVELY.

TABLE II: Parameters of various Resonant Tunneling Devices. Studied in this report.
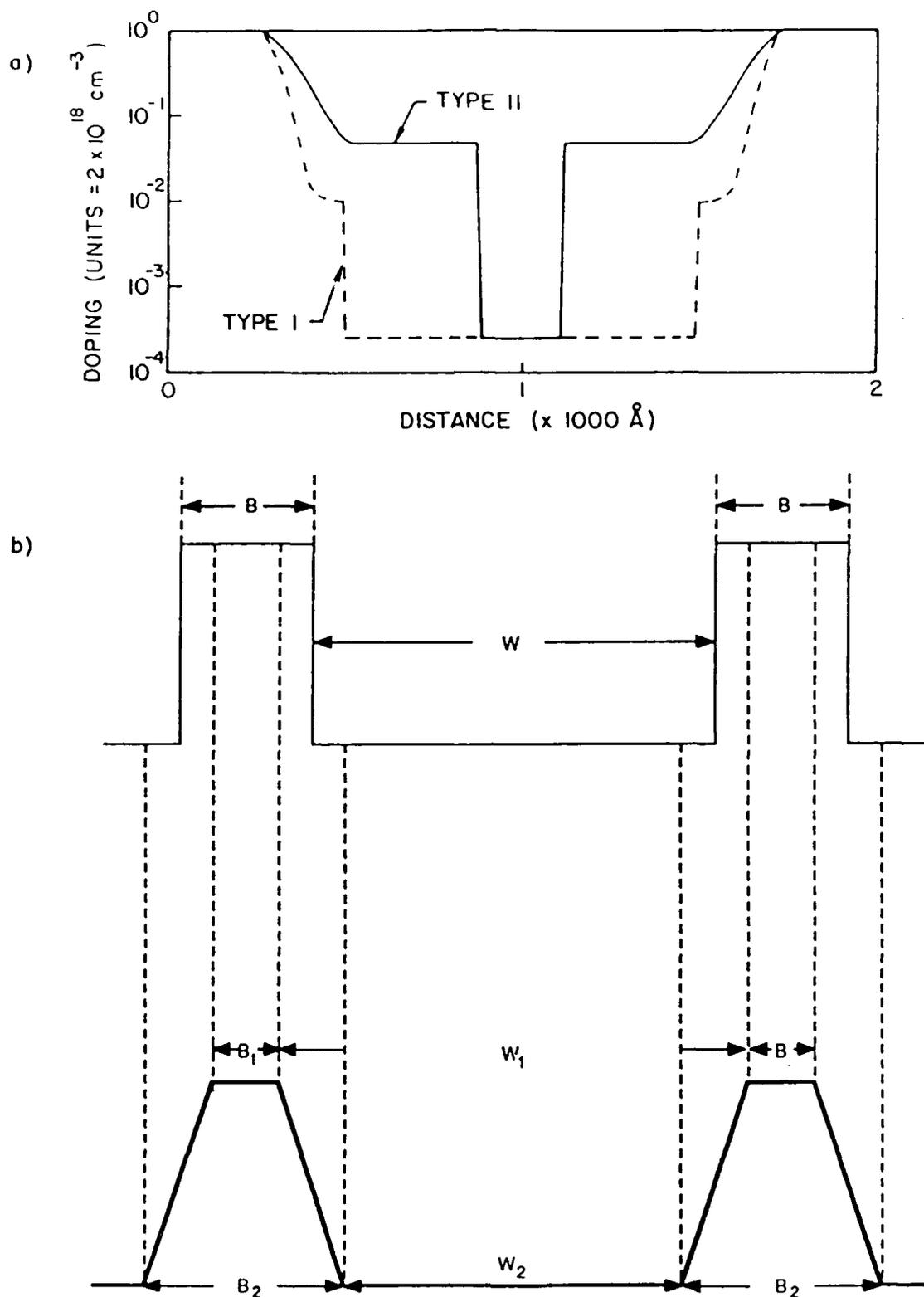
Figure 3: a) Doping profiles (type 1 and 11) considered in our numerical
simulations. The RTD is at the center of the device as the shape
shown in Figure 2b). b) Trapezoidal approximation of a typical RTD.
This approximation is used in our calculations to avoid the
numerical problems with shape interfaces. B,W are the Barrier/
well thickness respectively. $B_{1,2}$ and $W_{1,2}$ are chosen such that
$B = (B_1 + B_2)/2$ and $W = (W_1 + W_2)/2$.

1)

2)

(a) Bias voltage not sufficient
to cause resonant tunneling

(b) On resonance

(c) Bias too large for resonant tunneling
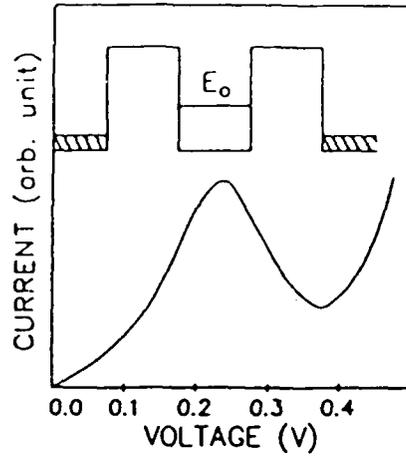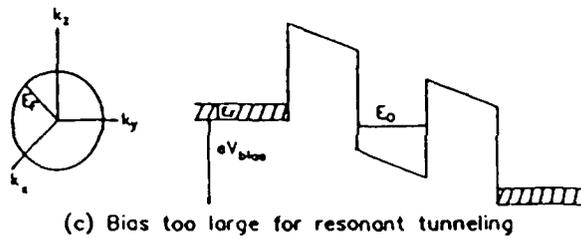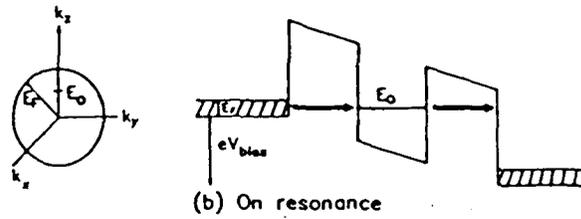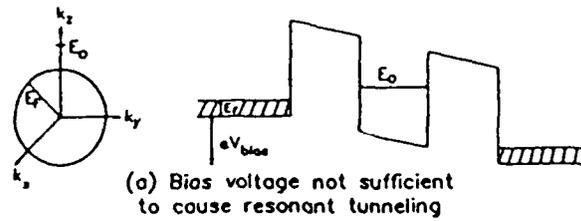
Figure 4: 1) Typical I-V characteristic of a resonant tunneling
structure. For coherent resonant tunneling, there is drop
in the I-V curve (NDR region) when the Quasi-Bound state E_o
is pulled below the conduction band in the left contact
(Figures 2a-b-c).
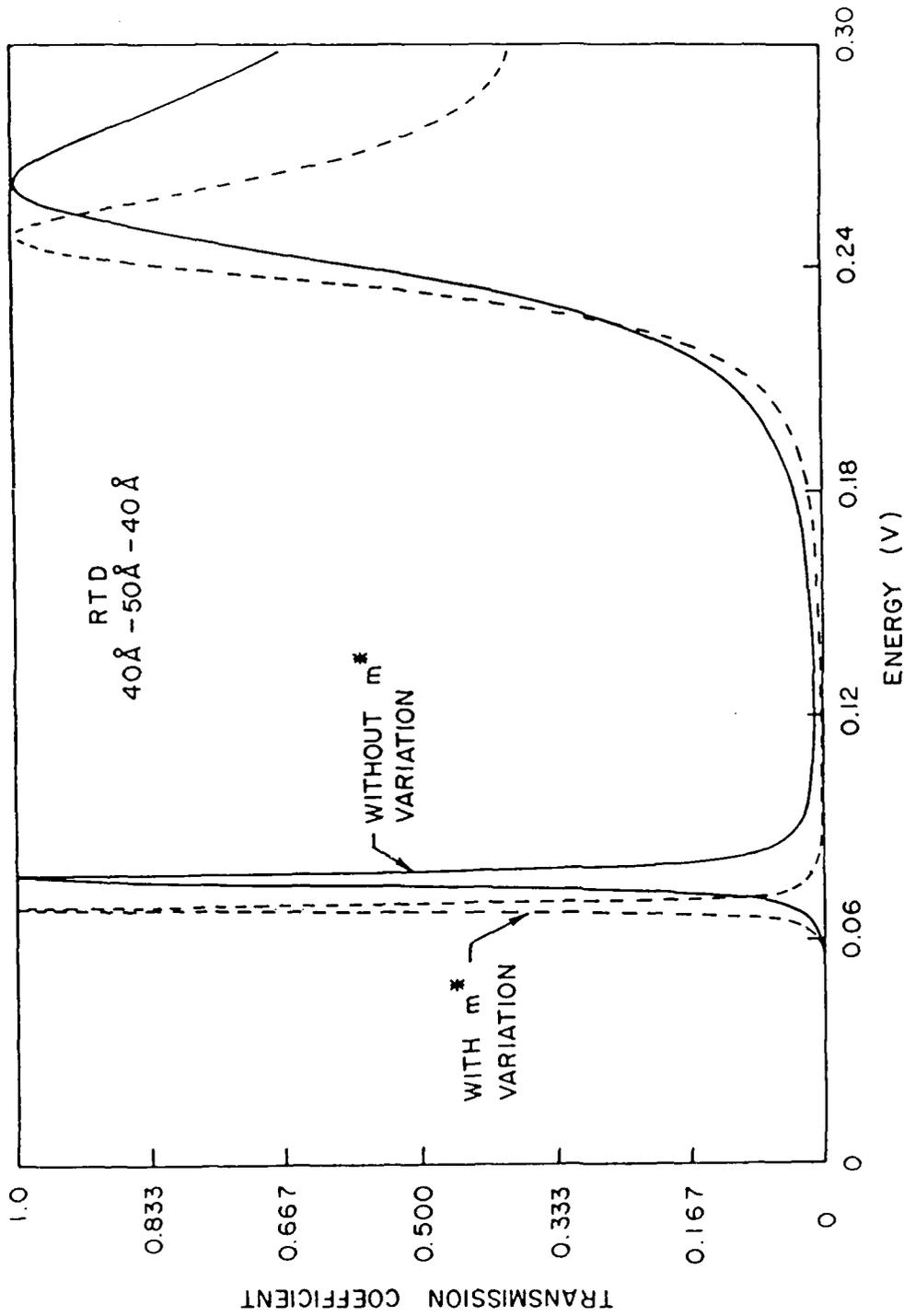
Figure 5a: Comparison of the transmission coefficient versus energy for a RTD (40Å-50Å-40Å) while including (dashed curve)/neglecting (full curve) the effective mass variation with position. The Barrier height is 0.209 eV. The effective mass in GaAs/ $Al_xGa_{1-x}As$ are 0.067/0.092 m_o respectively (x = 0.3).
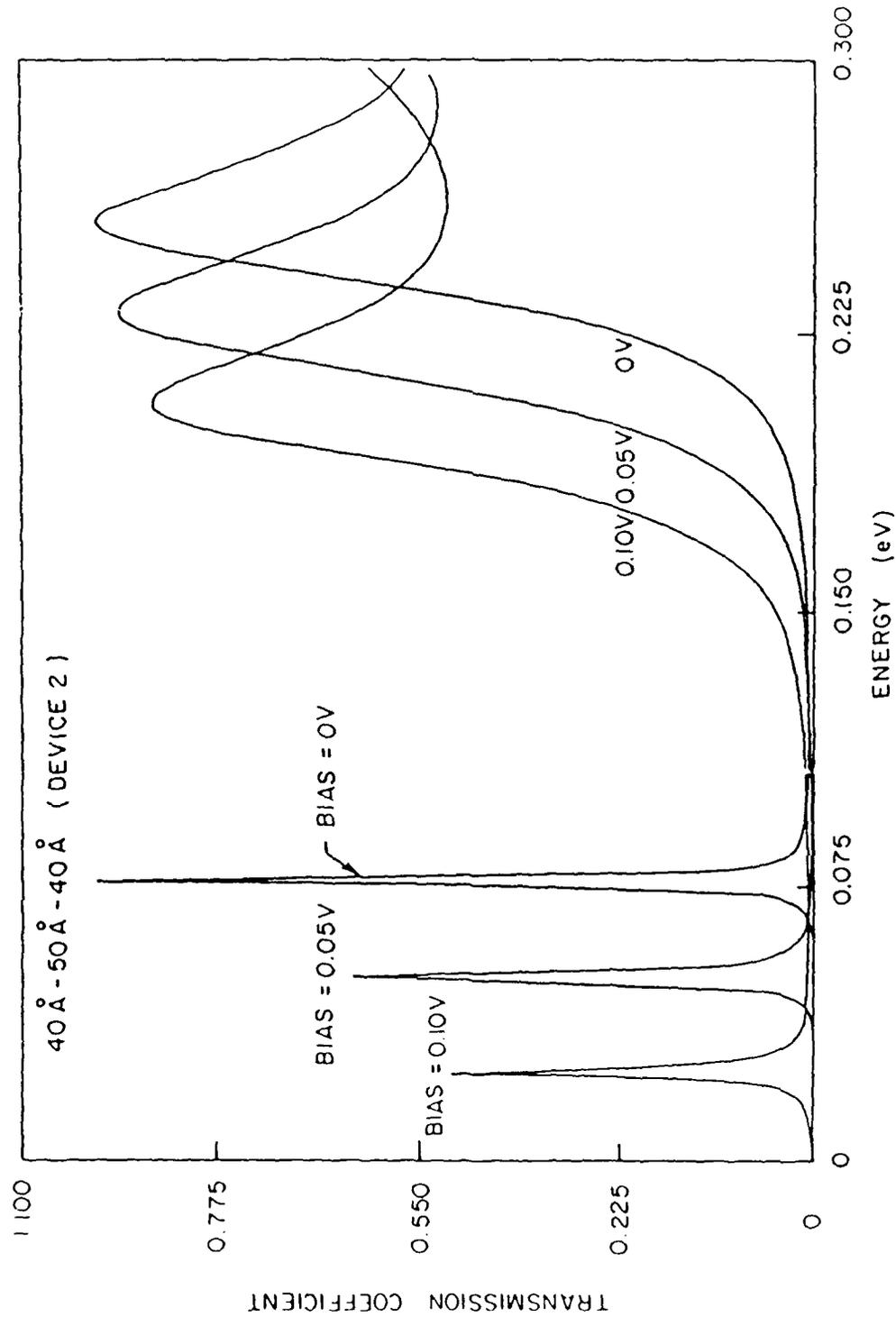
Figure 5b: Transmission coefficient versus energy for 3 different
bias applied across a typical resonant tunneling structure
(with a barrier height equal to 0.209eV). When the
applied bias is high enough, the resonance peak "disappears"
in the negative energy axis. This is the bias at which
negative energy is observed in the Tsu-Esaki's formalism.
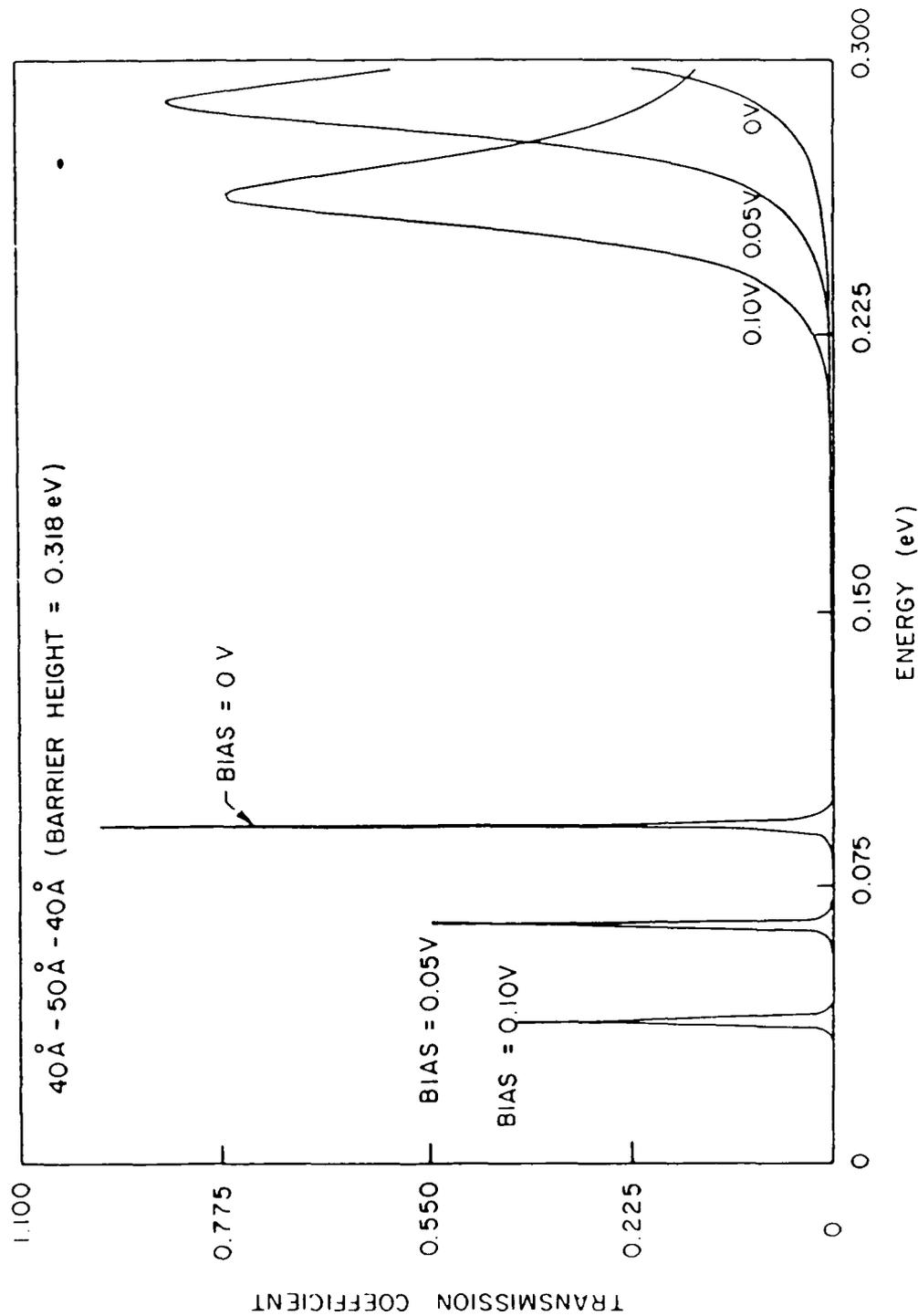
Figure 5c: Same as figure 5b for a resonant tunneling structure with a barrier height equal to 0.318eV. The Quasi-bound state is located higher in energy than in figure 5b. Therefore, the NDR occurs at a higher bias in the Tsu-Esaki formalism.

DOPING	DEVICE (SEE TABLE II)	V(NDR) TSU - ESAKI	V(NDR) (OUR CALCULATIONS)
TYPE I	# 1	0.13 eV	0.08 eV
TYPE I	# 2	0.13 eV	0.08 eV
TYPE I	# 3	0.14 eV	0.06 eV
TYPE I	# 4		NO NDR
TYPE II	# 6	0.12 eV	0.03eV

TABLE lll: Estimates of the position of the NDR region in the Tsu-Esaki Formalism.
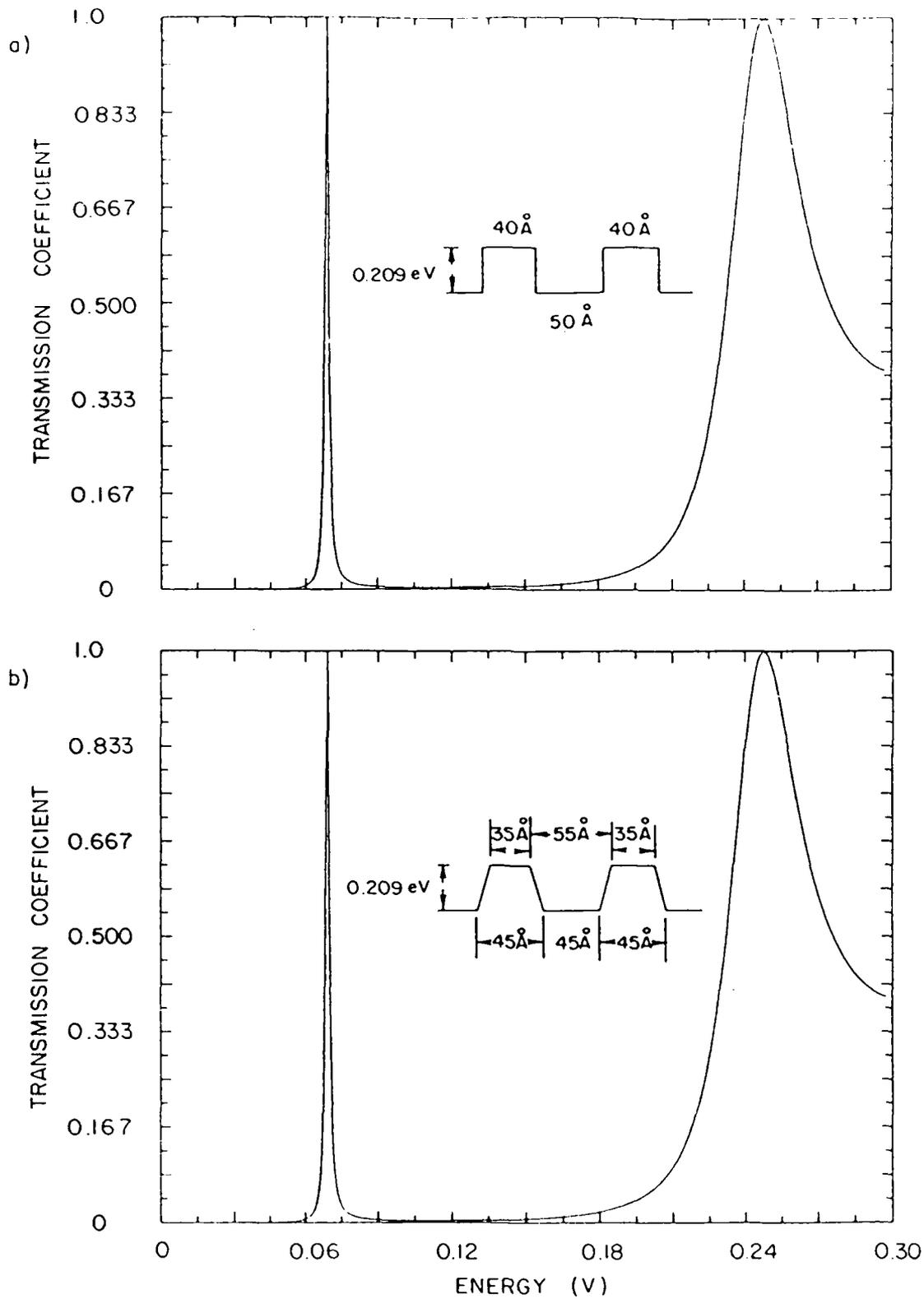
Figure 6: Transmission coefficient versus energy in the case a) of
perfectly sharp interfaces b) in the approximation of a
trapezoidal shape for the RTD. The effective mass variation
was taken into account.
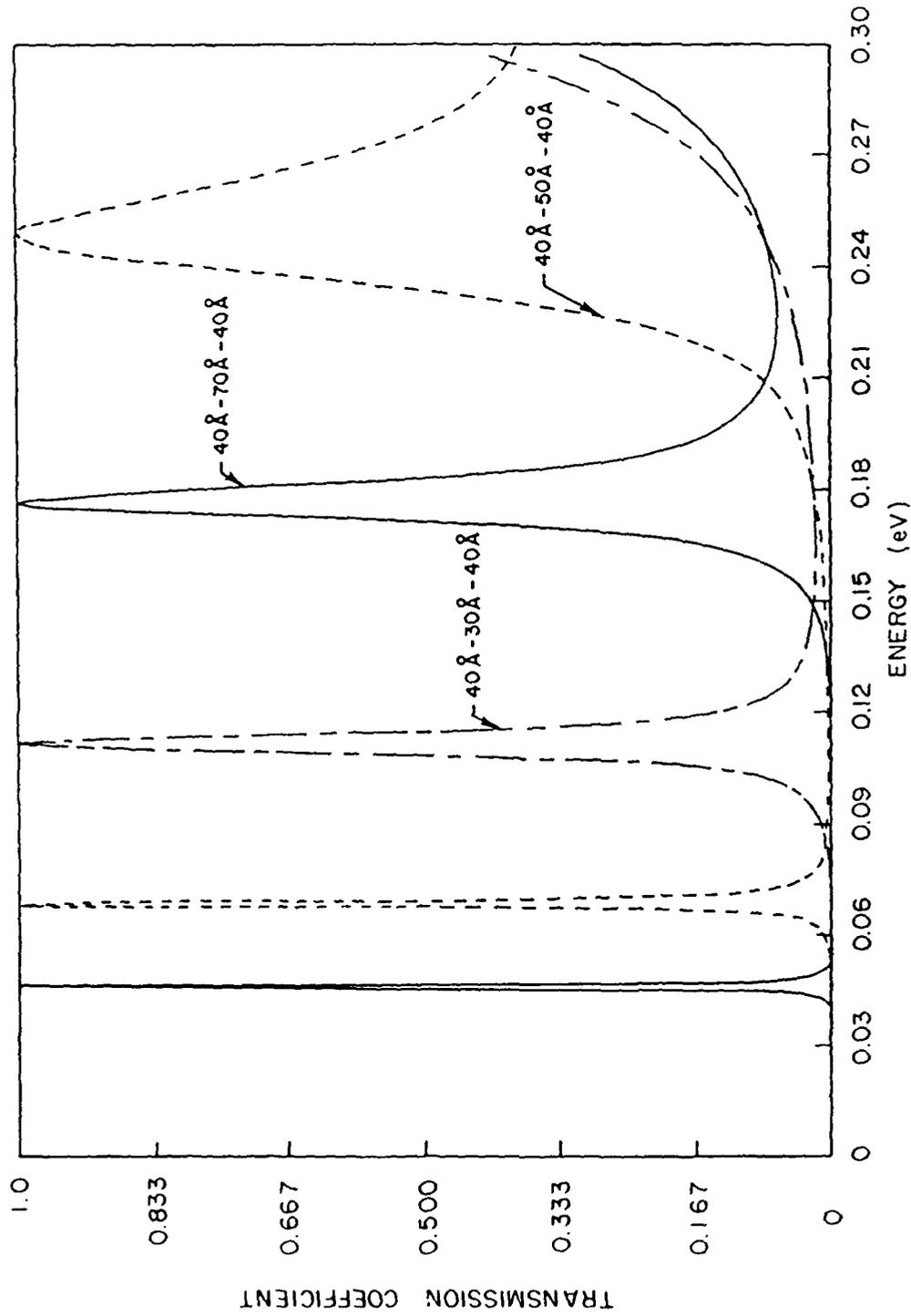
Figure 7 : Transmission coefficient versus energy through RTD's with different well sizes. The Barrier height is 0.209 eV. The effective mass variation is included in the calculation. The Quasi-Bound states energies are lower for RTD's with thicker wells.
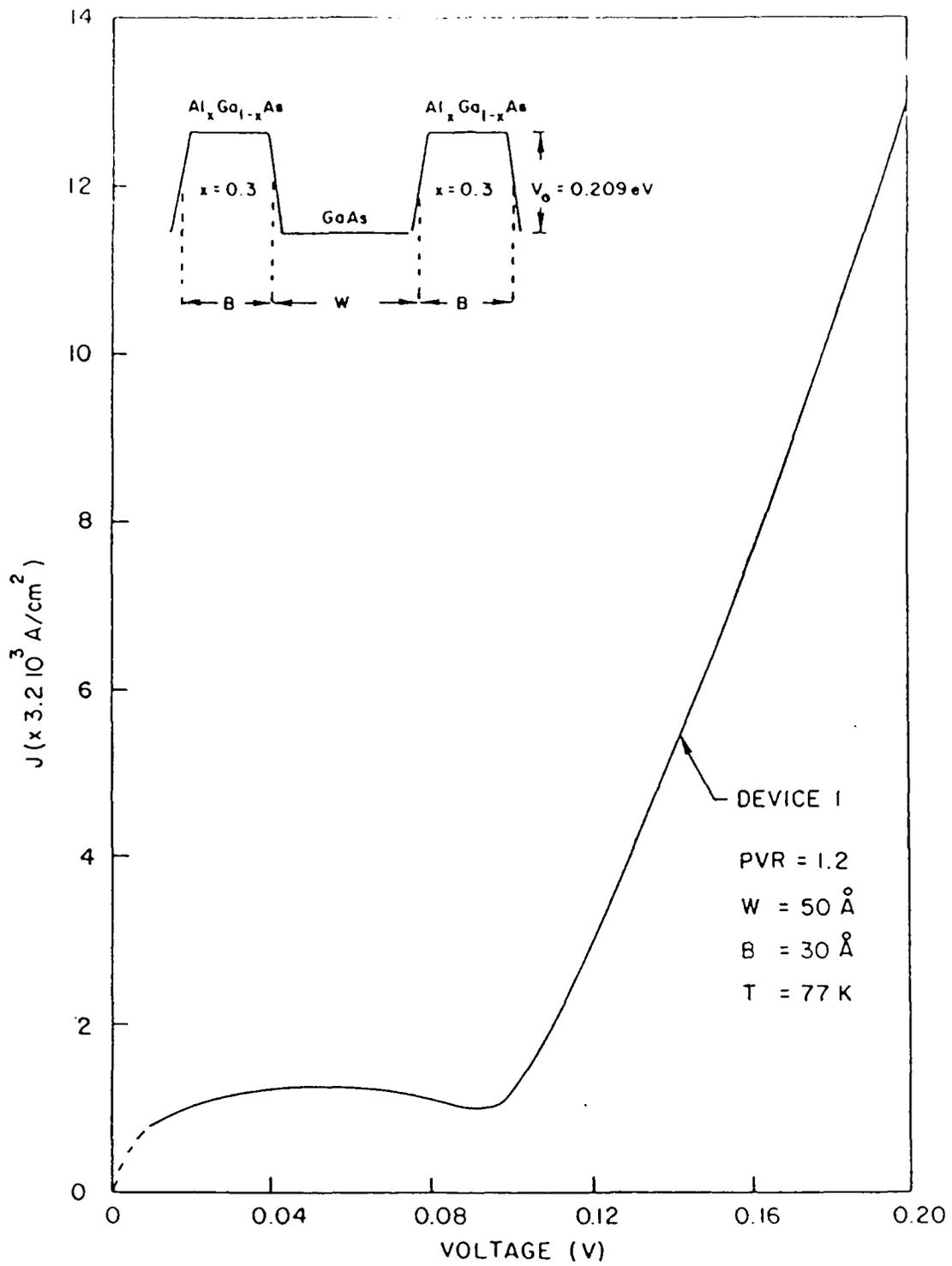
Figure 8: Current-Voltage Characteristic for device #1 of Table II. The parameters of the RTD are shown in the inset. The dashed line is the expected shape of the I-V curve at low value of bias.
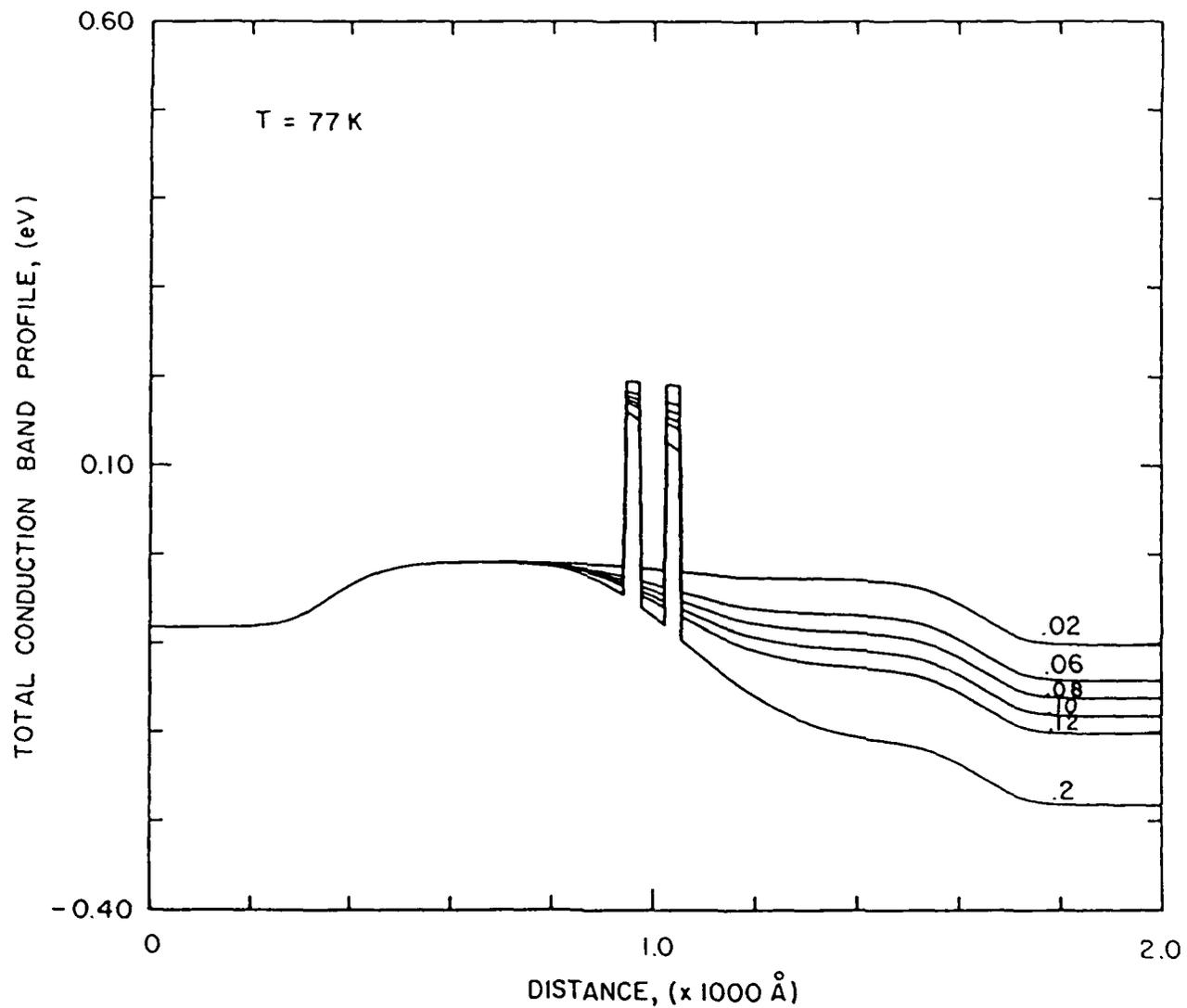
Figure 9a: Total conduction band energy profile as a function of bias for Device #1 of Table II. The different curves are labeled with the value of the voltage at which they are calculated.
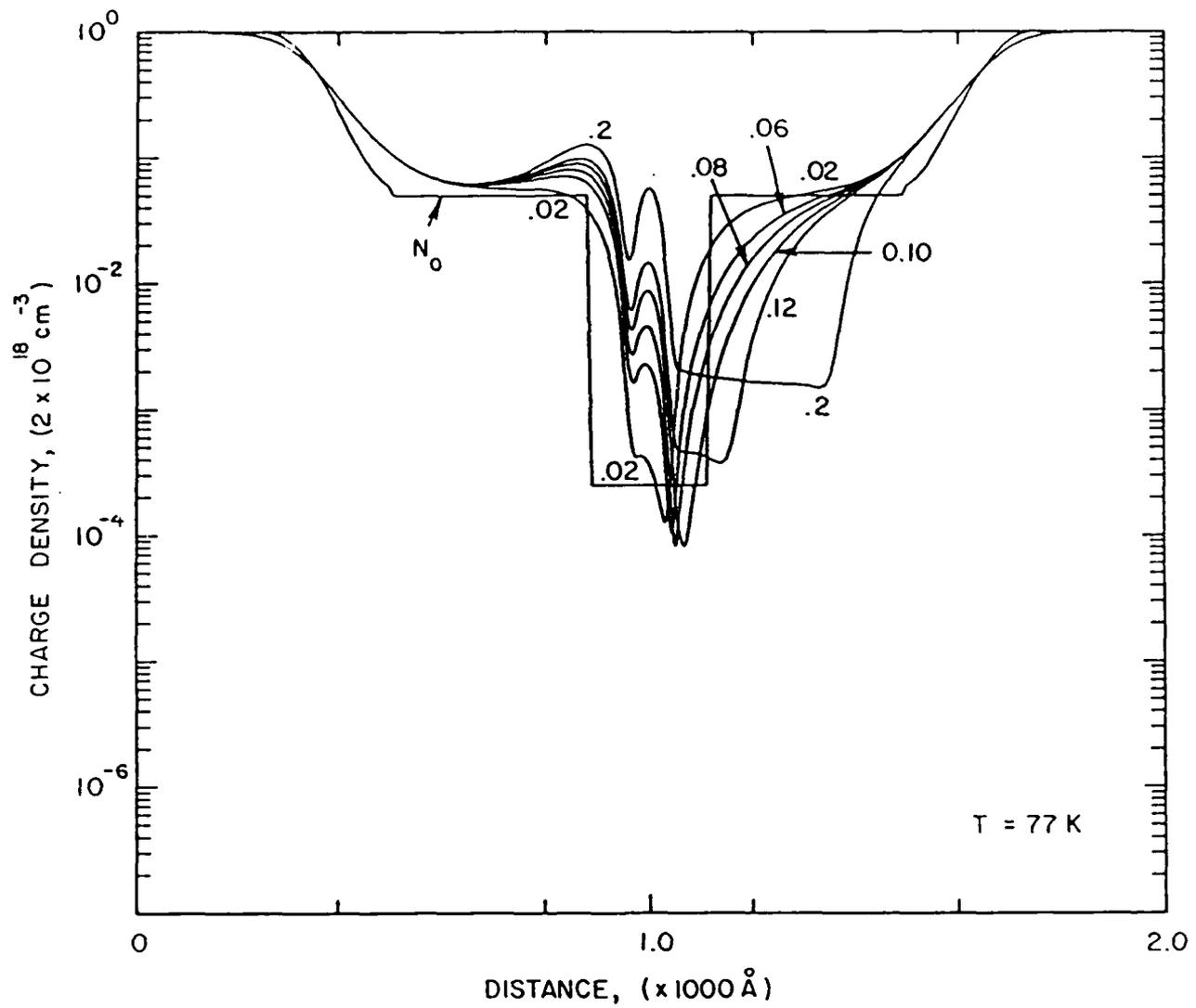
Figure 9b: Charge density as a function of bias for Device #1 of
Table II. N_o is the doping profile (type II; see fig. 2a).
The different curves are labeled with the
value of the voltage at which they are calculated.
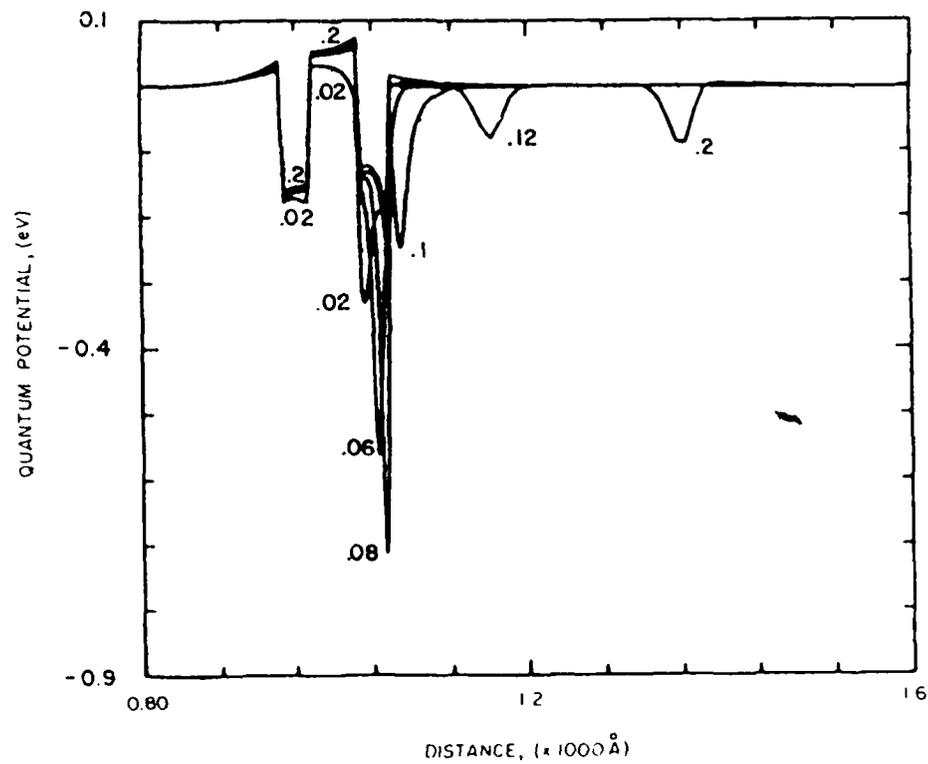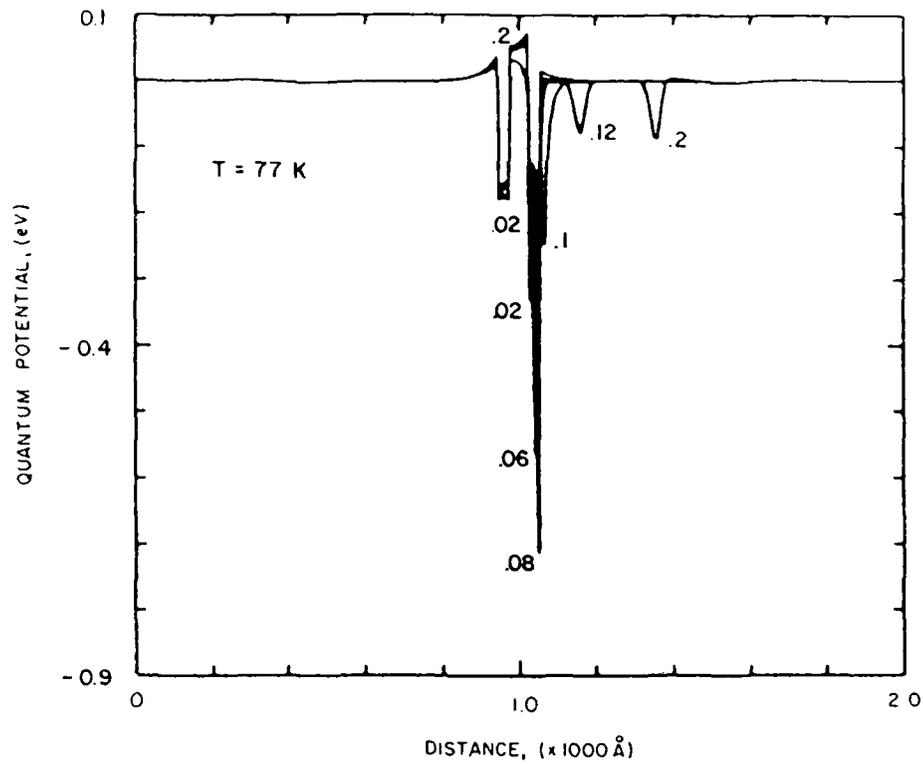
Figure 9c: Quantum potential as a function of bias for Device #1 of Table II. The lower figure is a closer look at the Quantum potential variation shown in the upper figure. The different curves are labeled with the value of the voltage at which they are calculated.
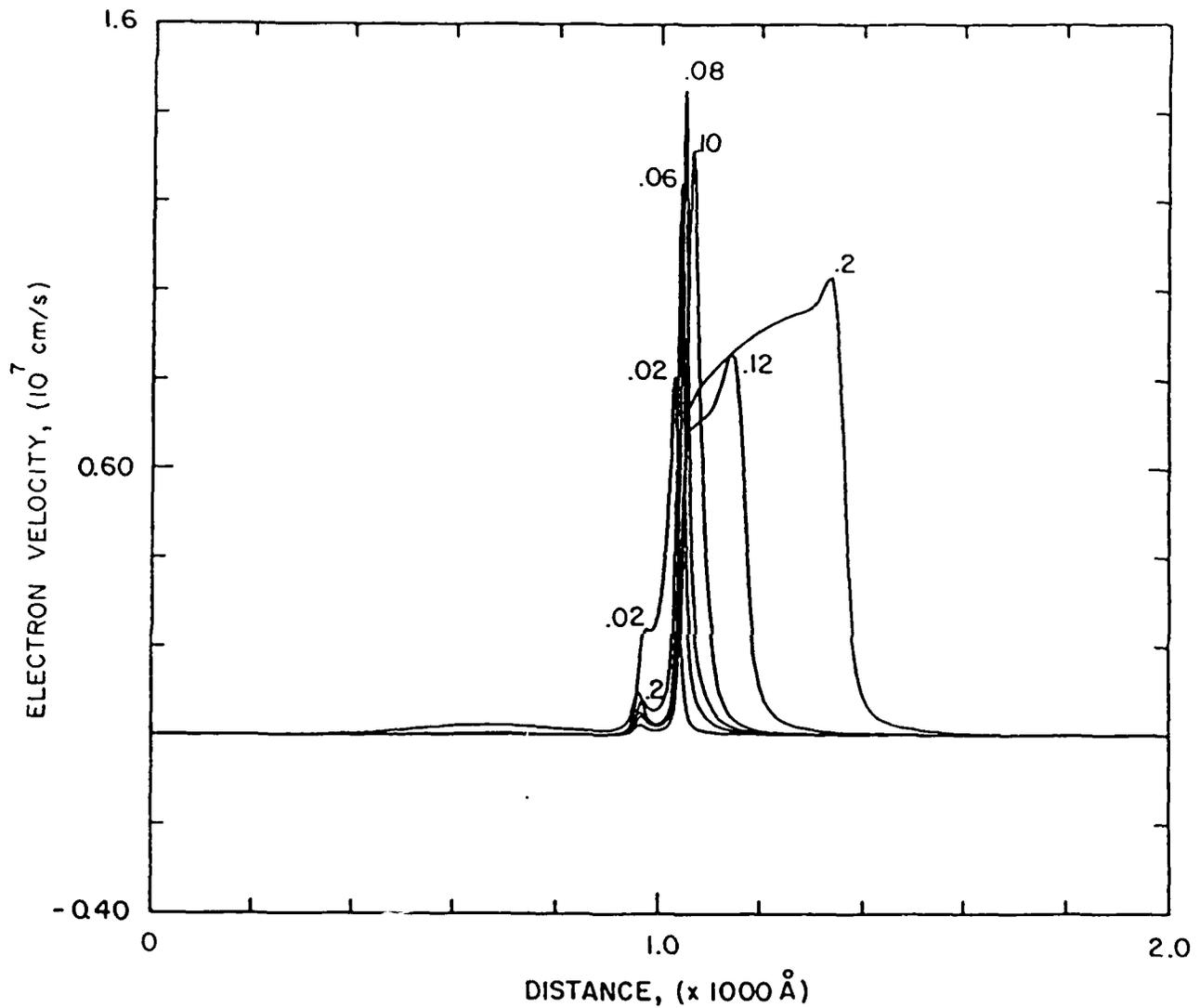
Figure 9d: Average velocity as a function of bias for Device #1 of Table II. The different curves are labeled with the value of the voltage at which they are calculated. The average velocity in the well increases for biases higher than the one corresponding to the minimum in the I-V curve.
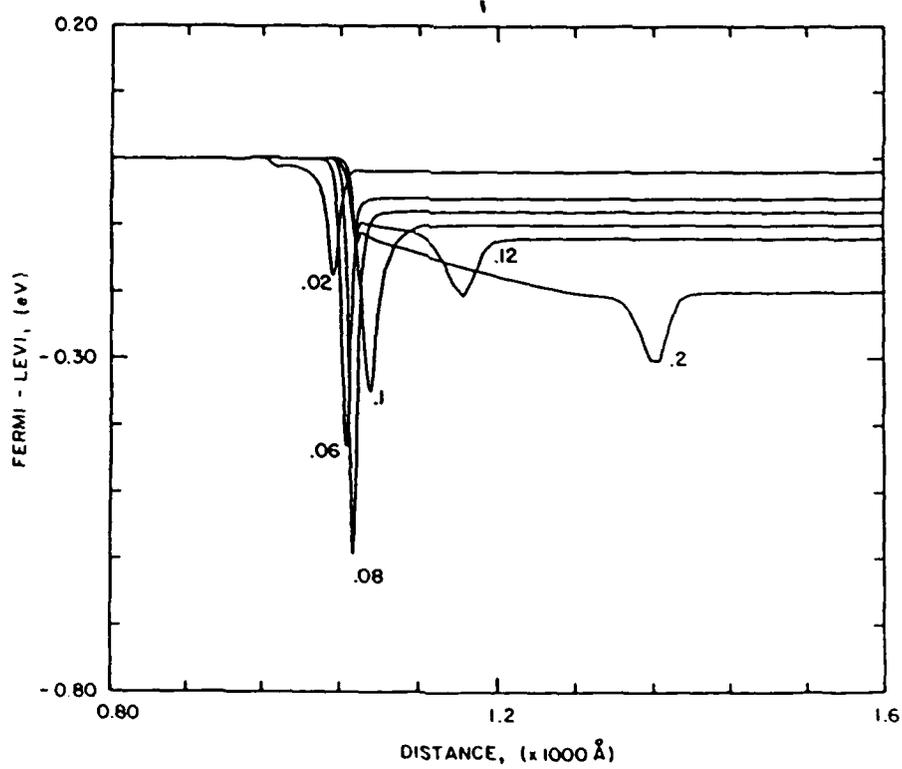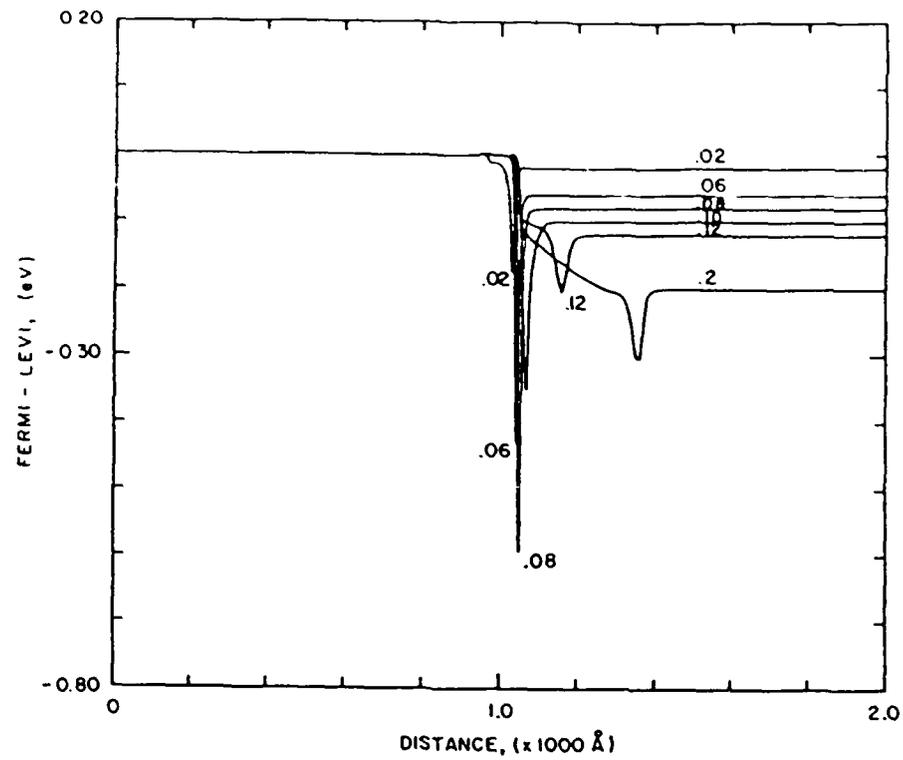
Figure 9e: Fermi level as a function of bias for Device #1 of Table II. The lower figure zooms on the interior of the device. The different curves are labeled with the value of the bias at which they are calculated. Notice the strong position dependence of the Fermi level across the double barrier resonant tunneling structure.
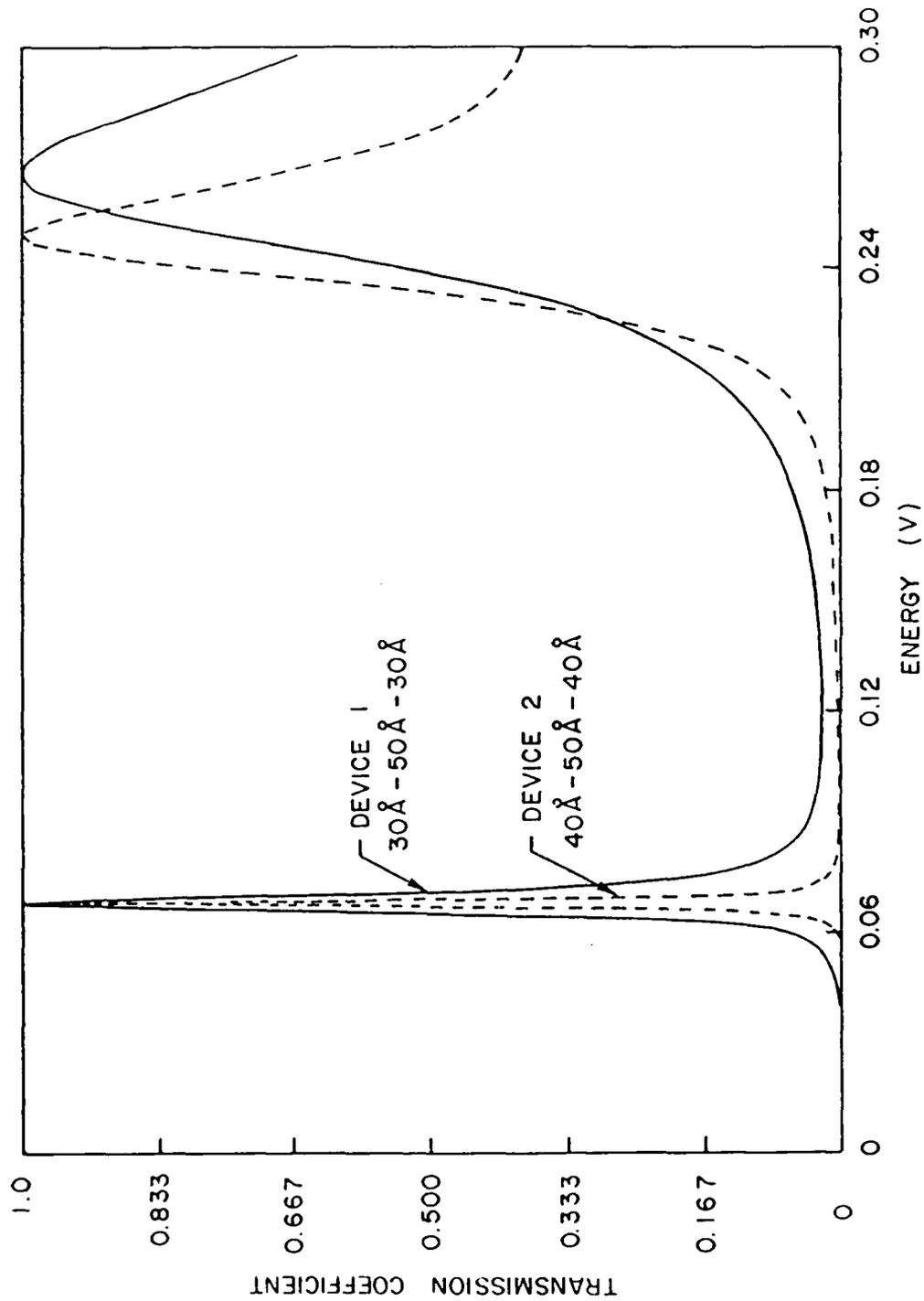
Figure 10: Comparison of the transmission coefficient through RTD's with different barrier thickness. The position of the first Quasi-Bound state is basically independent of the barrier thickness. The width of the transmission peak however is broader for RTD with thinner barriers.
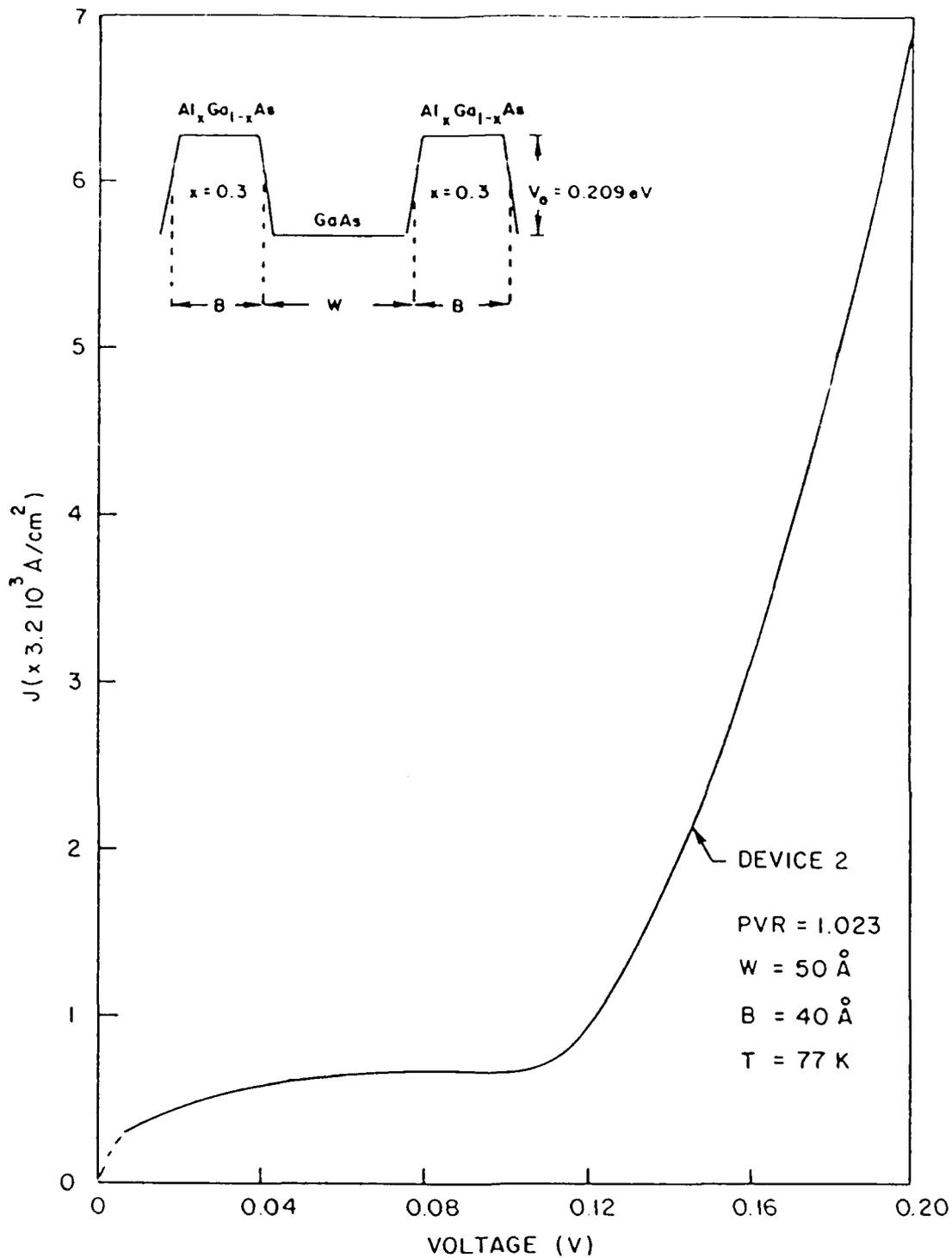
Figure 11: Current-voltage characteristics for device #2 of Table II.
The parameters of the RTD are shown in the inset.
The dashed line is the expected shape of the I-V curve
at low value of bias.
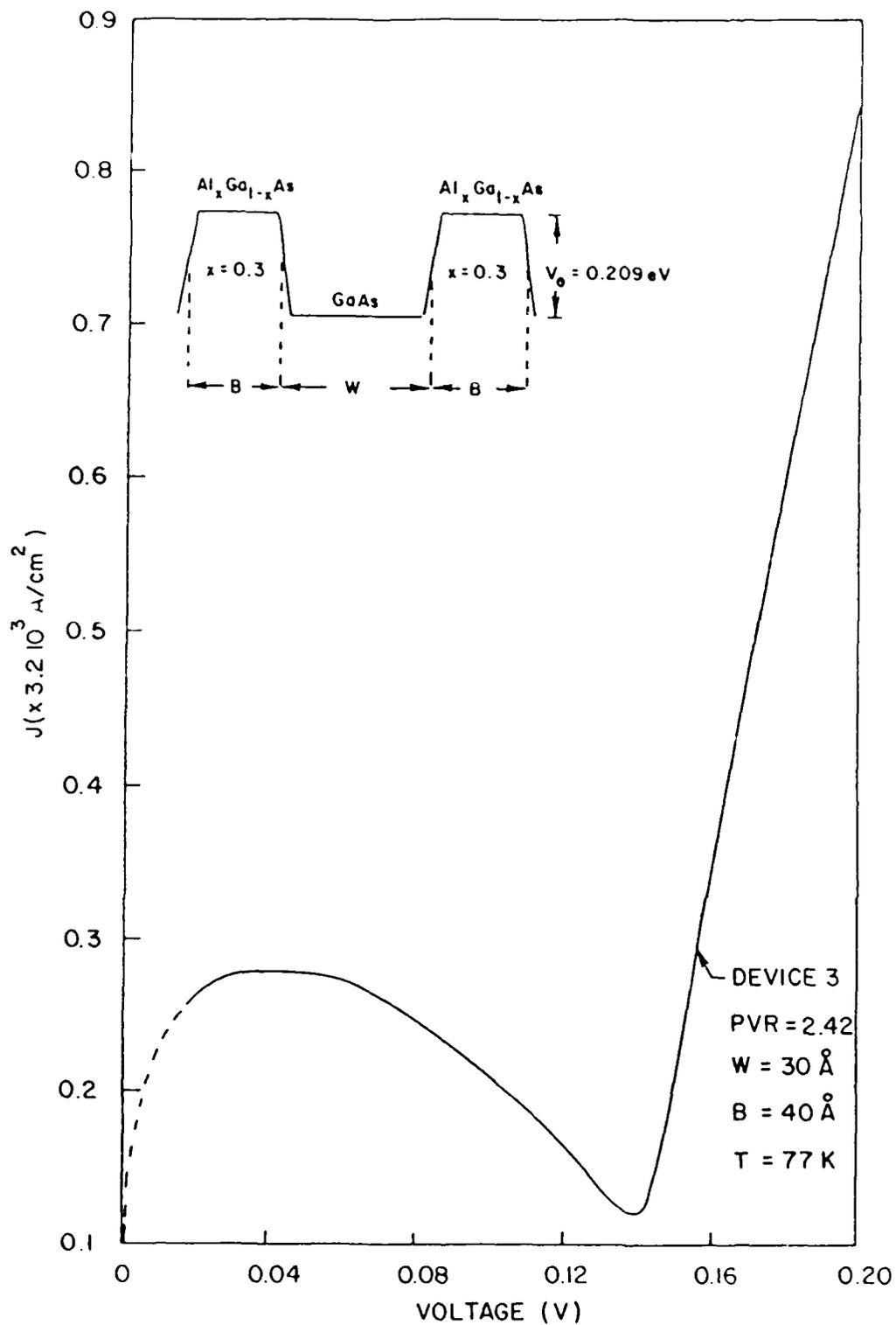
Figure 12: Dependence of the current-voltage characteristic on the
well thickness (compare with figures 11 and 13).
The resonant tunneling structure is shown in the inset.
The dashed line is the expected shape of the I-V curve at
low value of bias.
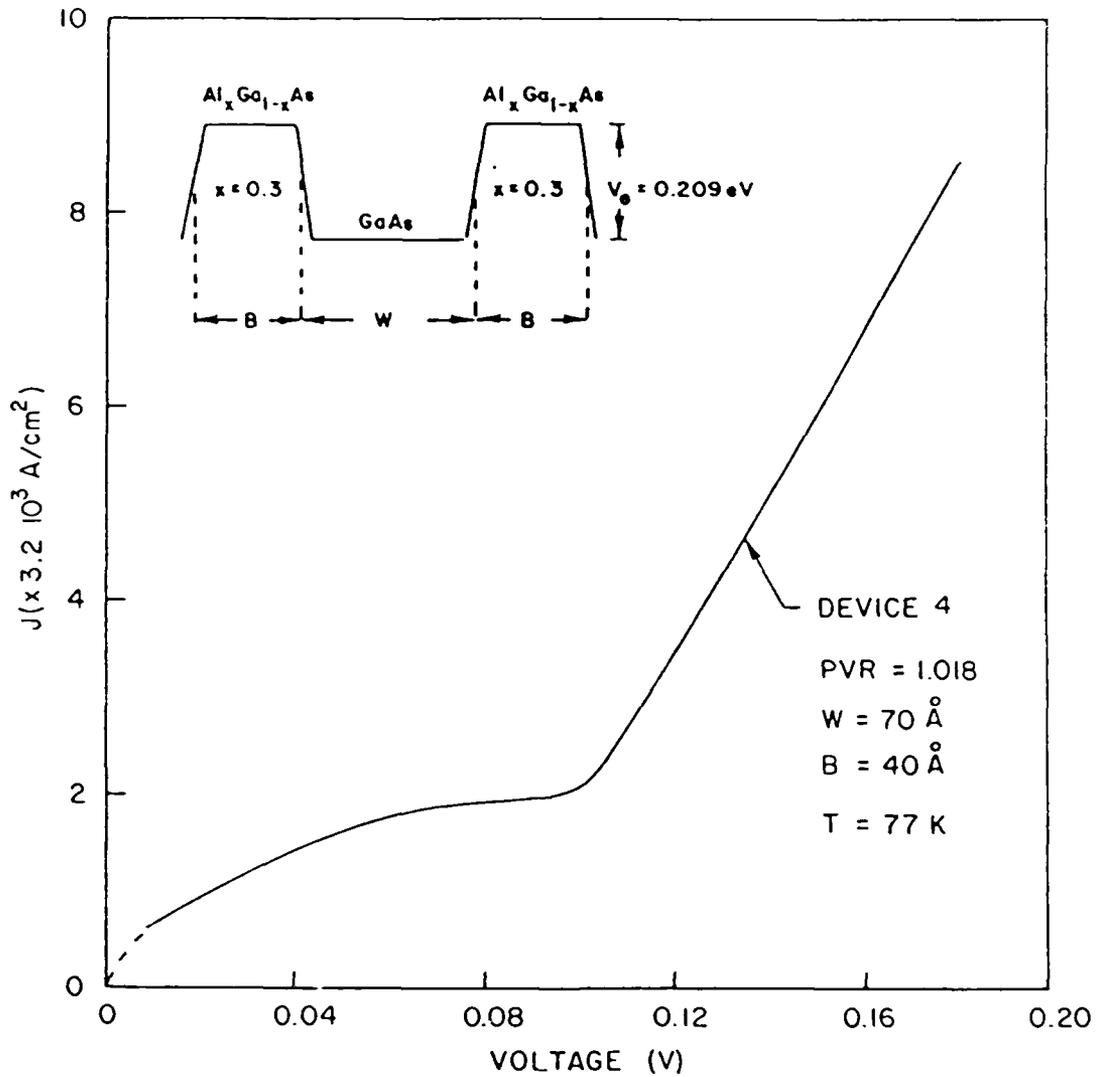
Figure 13: Dependence of the current-voltage characteristic on the
well thickness (compare with figures 11 and 12).
The resonant tunneling structure is shown in the inset.
The dashed line is the expected shape of the I-V curve
at low value of bias.
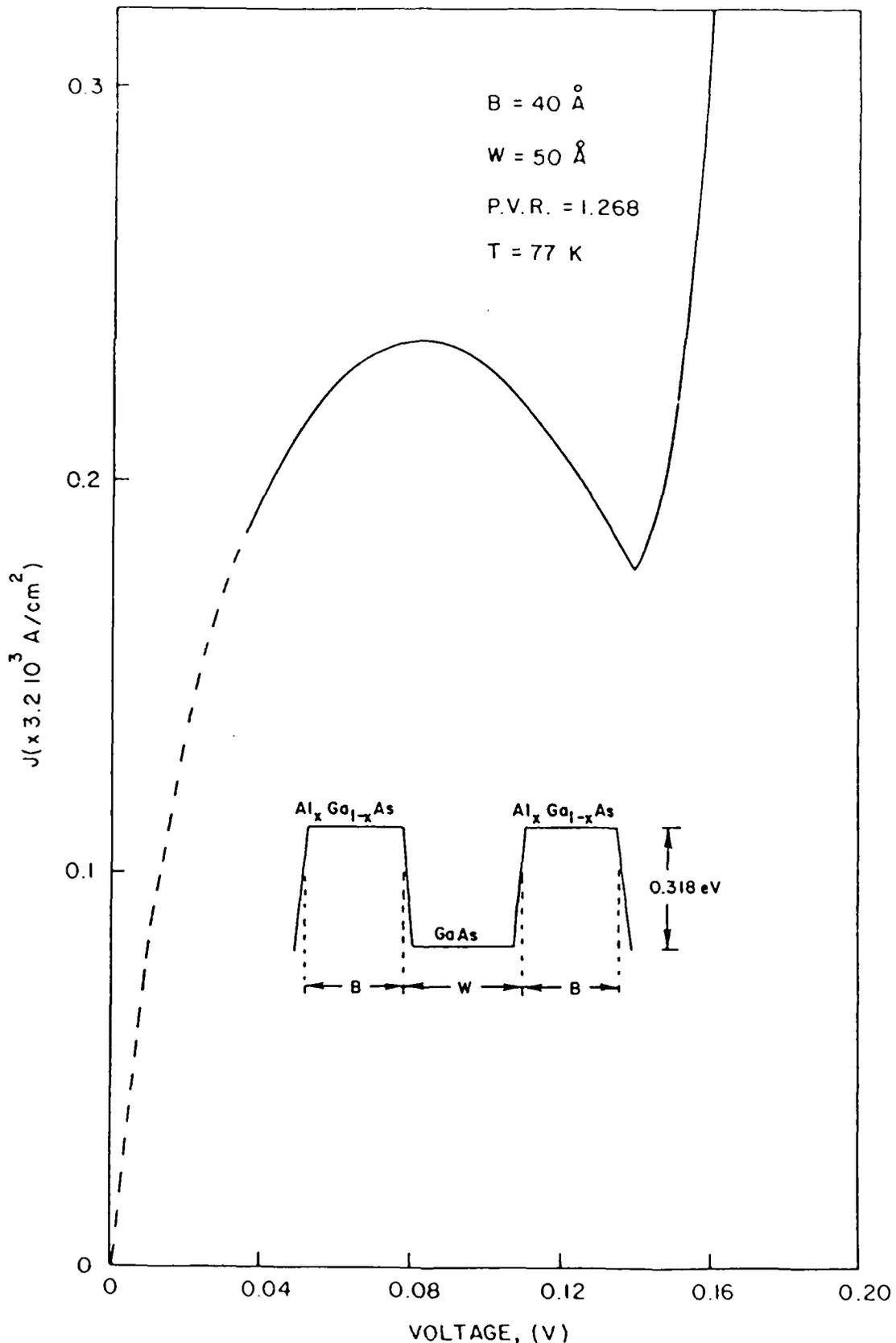
Figure 14: Current-voltage characteristic for RTD shown in the insert. The barrier height is 0.318eV and the effective mass is assumed to be constant $(m^*_{GaAs} = 0.067m_0)$.

The doping profile of type II is considered in our numerical simulations. However, the 50Å regions on both sides of the RTD were assumed to be undoped. The dashed line is the expected shape of the I-V curve at low value of bias.
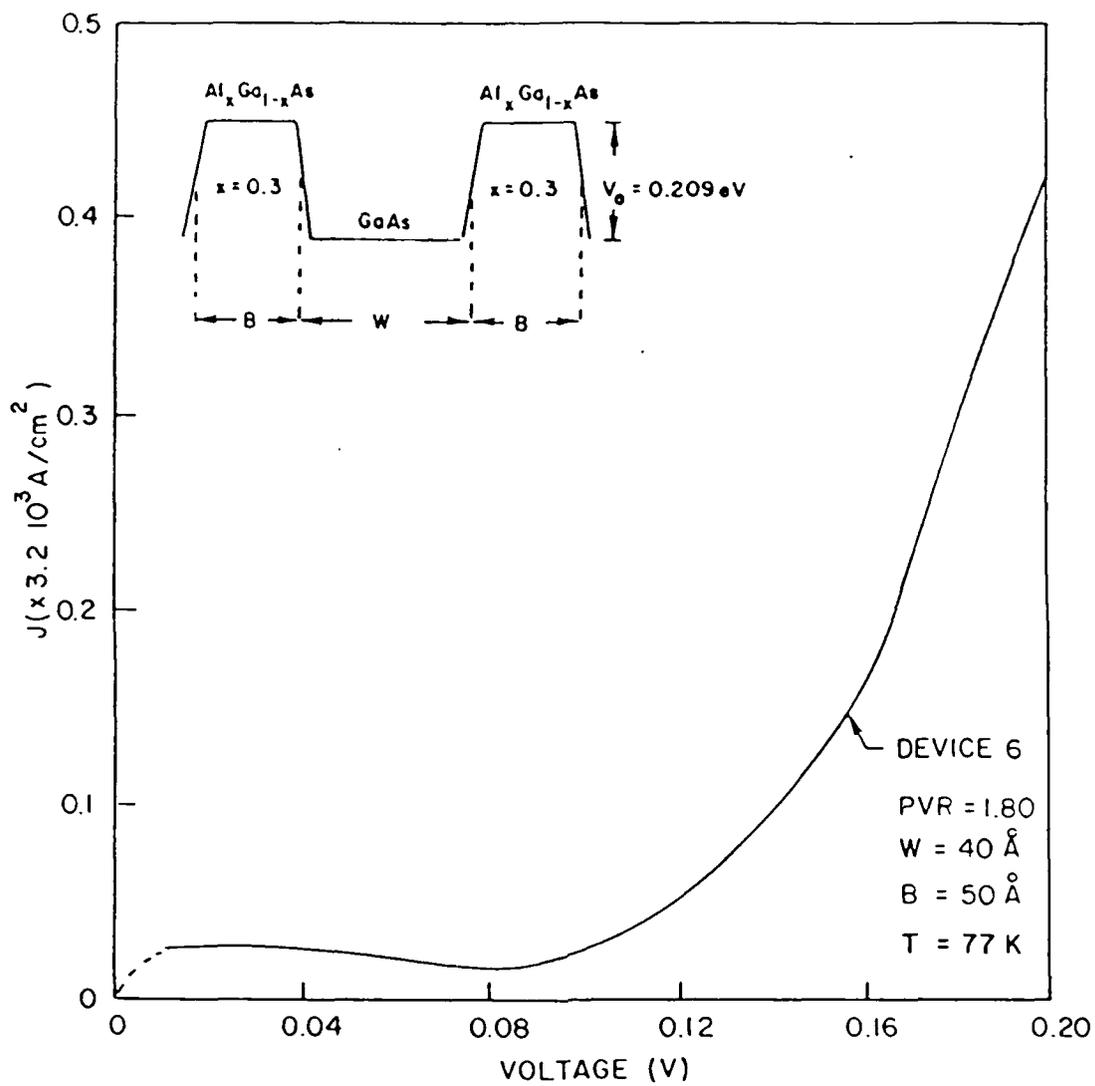
Figure 15: Current-voltage characteristics for device #6 of Table II.
The parameters of the RTD are shown in the inset.
The dashed line is the expected shape of the I-V curve
at low value of bias.
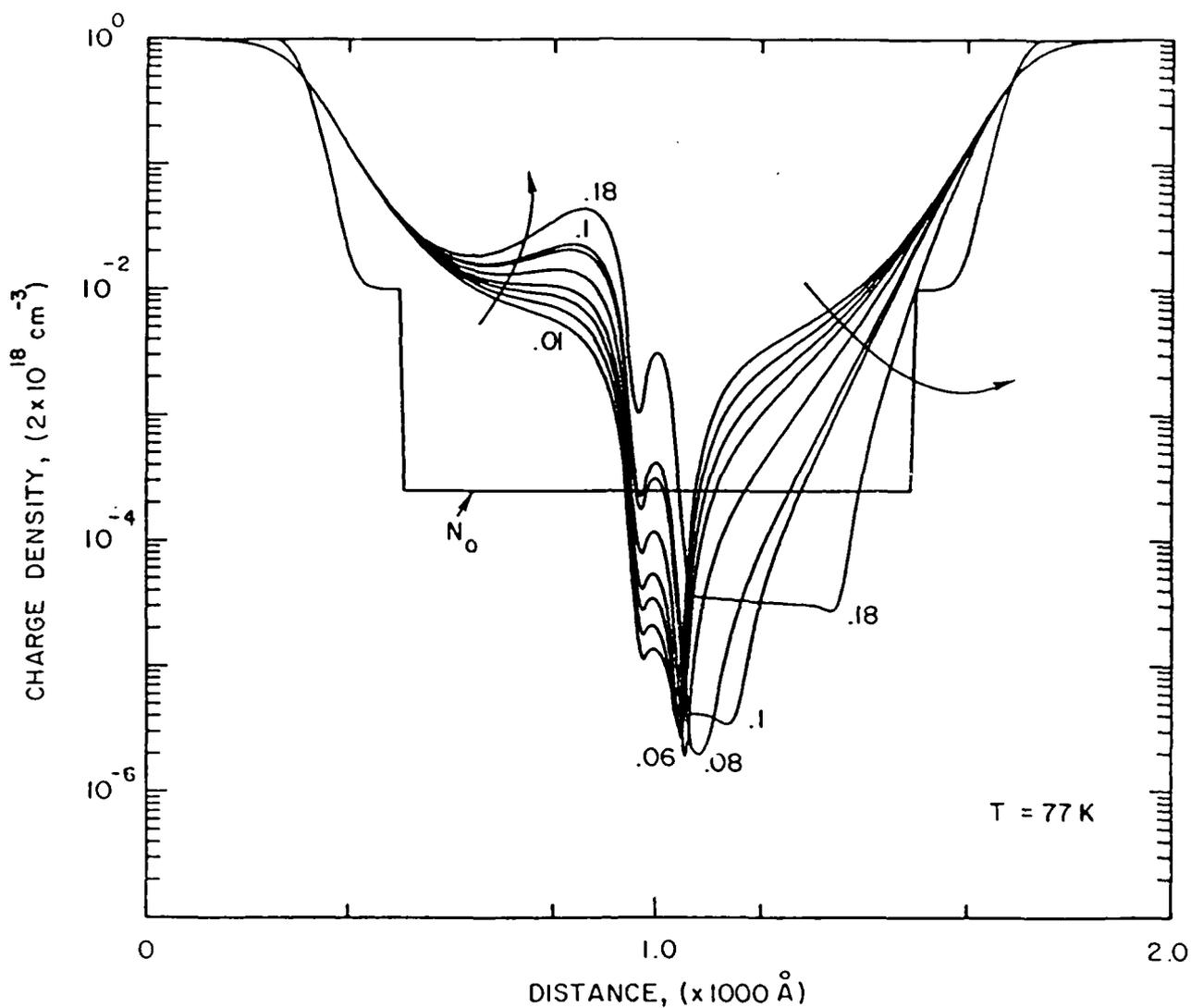
Figure 16a: Charge density as a function of applied bias for device #6
of Table II. The sloping in the middle of the device is
$5 \times 10^{16} cm^{-3}$. The bias increases in the direction indicated
by the arrow (0.01; 0.02; 0.03; 0.04; 0.06; 0.08; 0.10;
0.18). N_0 is the doping profile (type II; see fig. 2a)
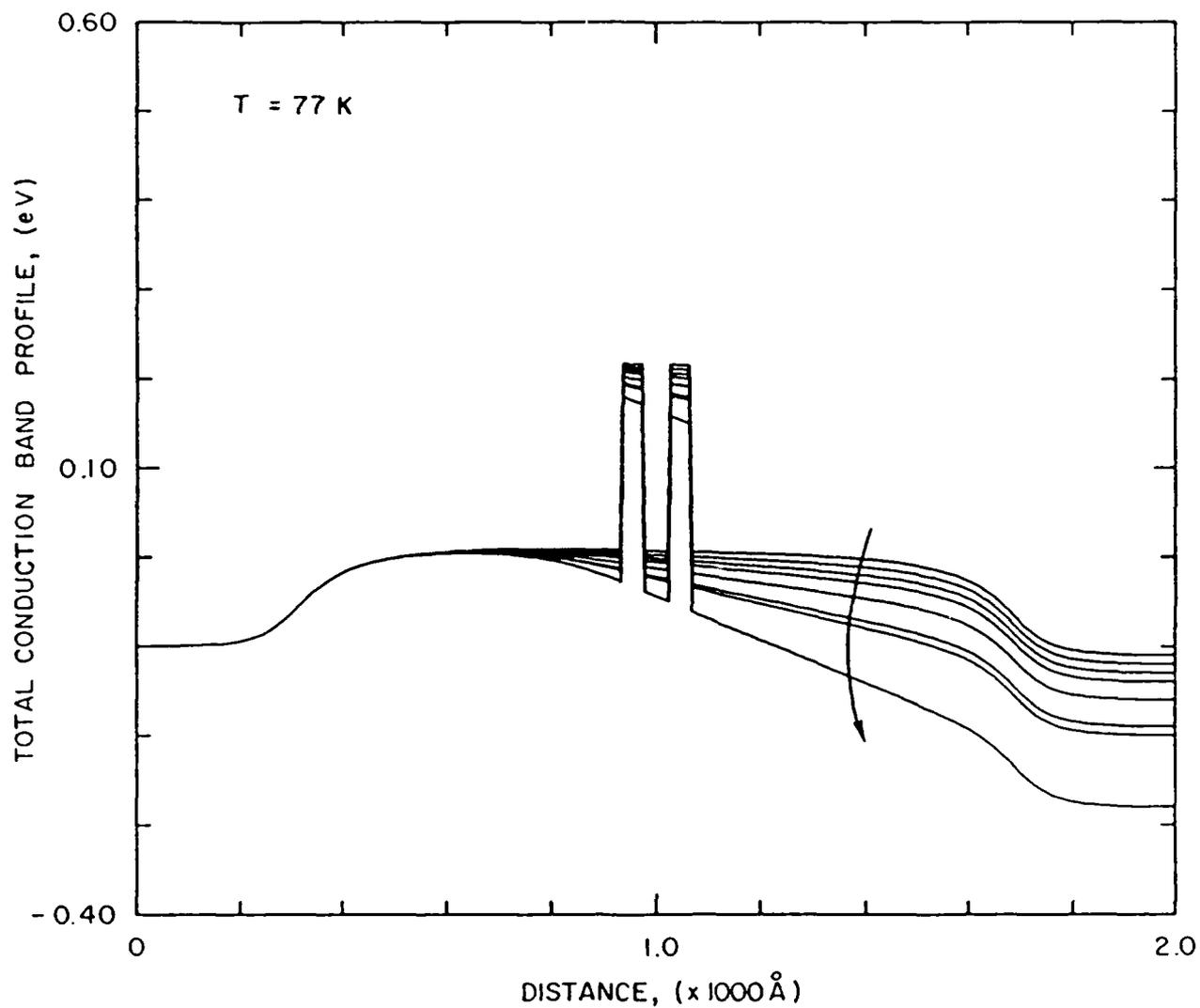
Figure 16b : Conduction Band Energy profile as a function of applied
bias for Device #6 of Table II. The bias increases
in the direction indicated by the arrow (0.01; 0.02; 0.03;
0.04; 0.06; 0.08; 0.10; 0.18).
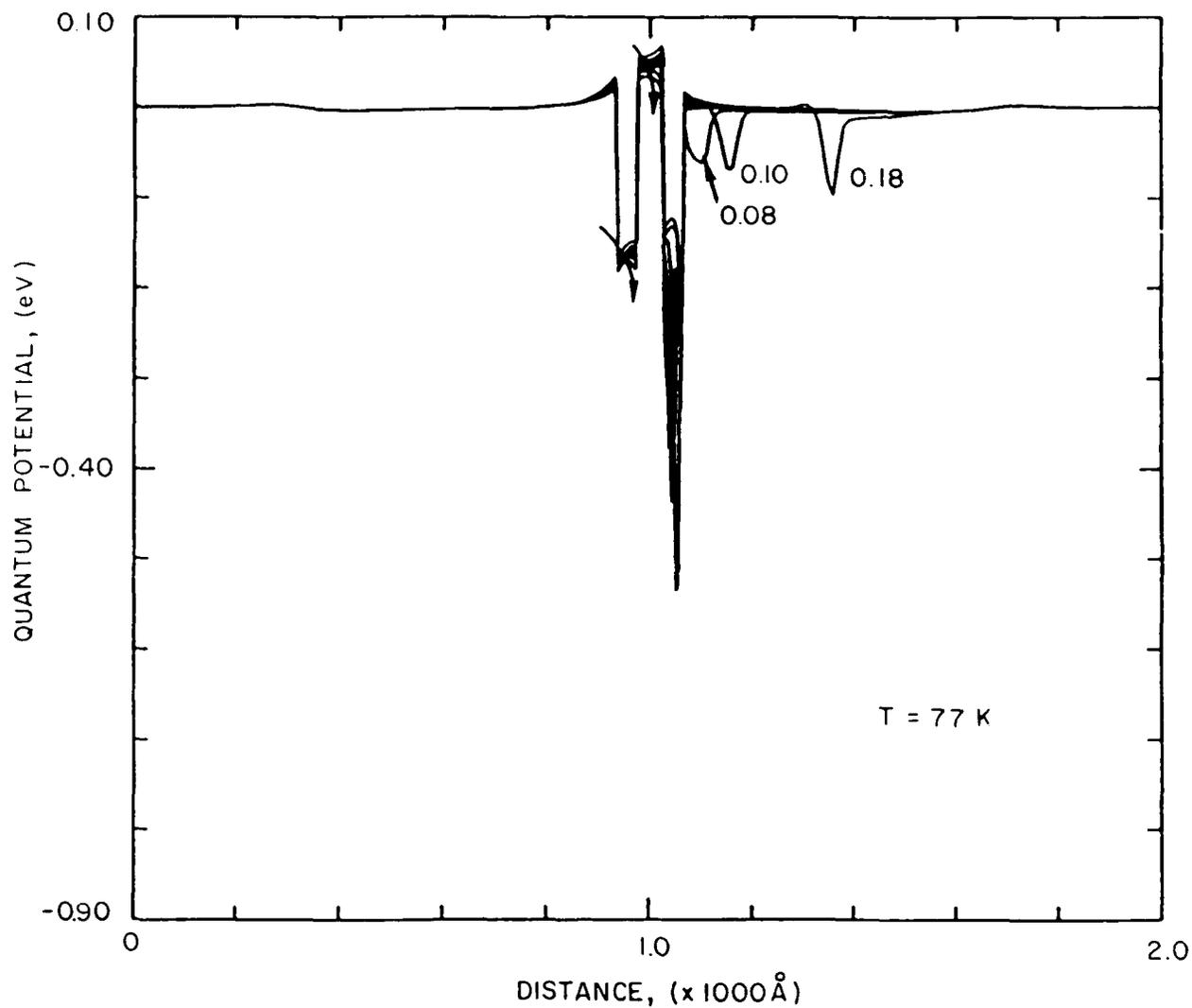
Figure 16c: Quantum Potential as a function of applied bias for device #5 of Table II. The charge density profile for the same structure is shown in figure 16a. The bias increases in the direction indicated by the arrow (0.01; 0.02; 0.03; 0.04; 0.06; 0.08; 0.10; 0.18).
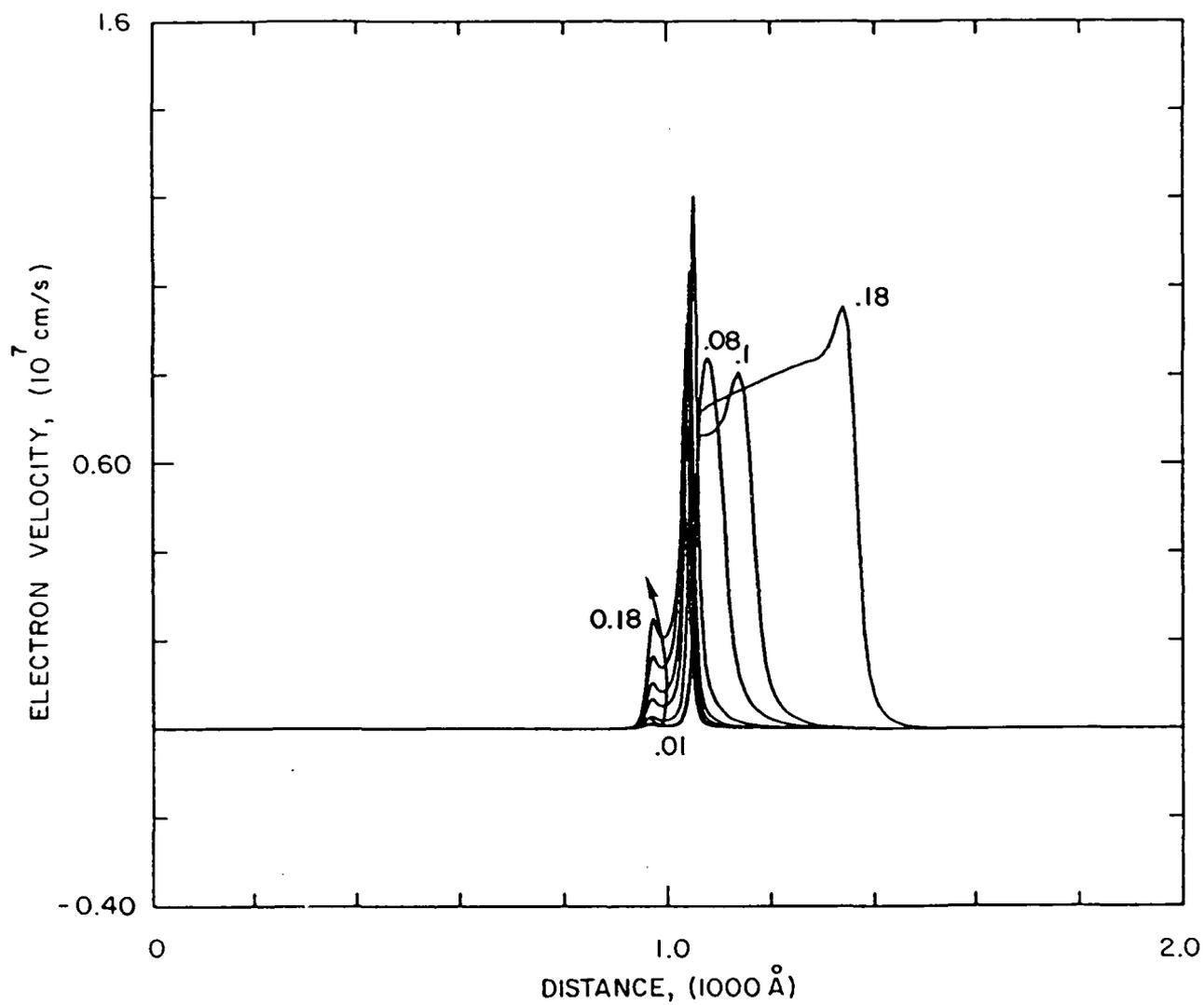
Figure 16d: Average velocity as a function of bias for Device 6
of Table II. The different curves are labeled with the
value of bias at which they are calculated. The arrow
indicates the direction of increasing biases.
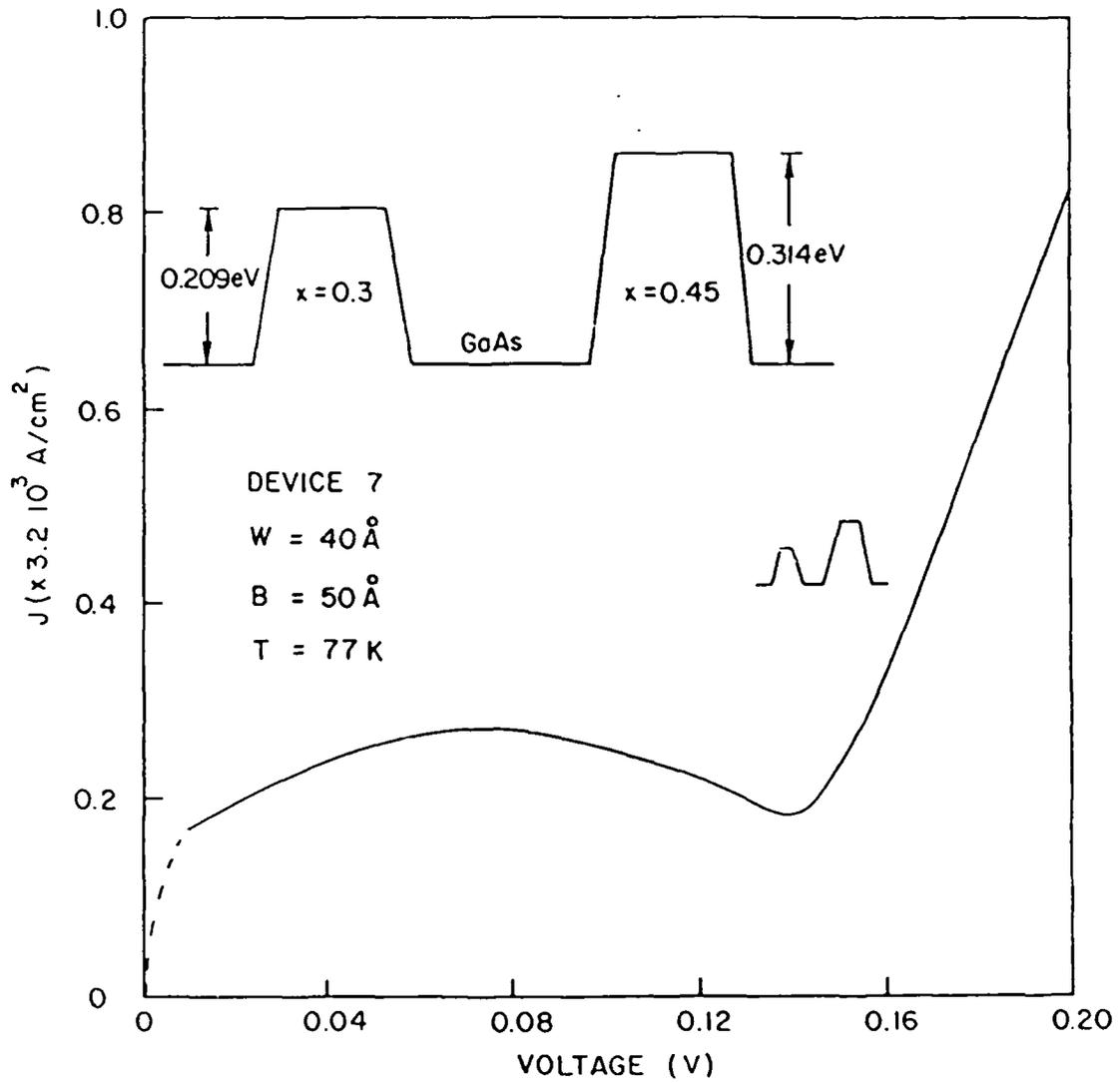
Figure 17: Current-Voltage Characteristic for device #7 of Table II. The parameters of the RTD are shown in the inset. The dashed line is the expected shape of the I-V curve at low value of bias.

6.0

5.0

0.209eV   x = 0.3   GaAs   x = 0.45   0.314eV

4.0

$J(\times 3.2\ 10^3\ A/cm^2)$

3.0

DEVICE 8

W = 40 Å

2.0

B = 50 Å

T = 77 K

1.0

0

0   0.04   0.08   0.12   0.16   0.20
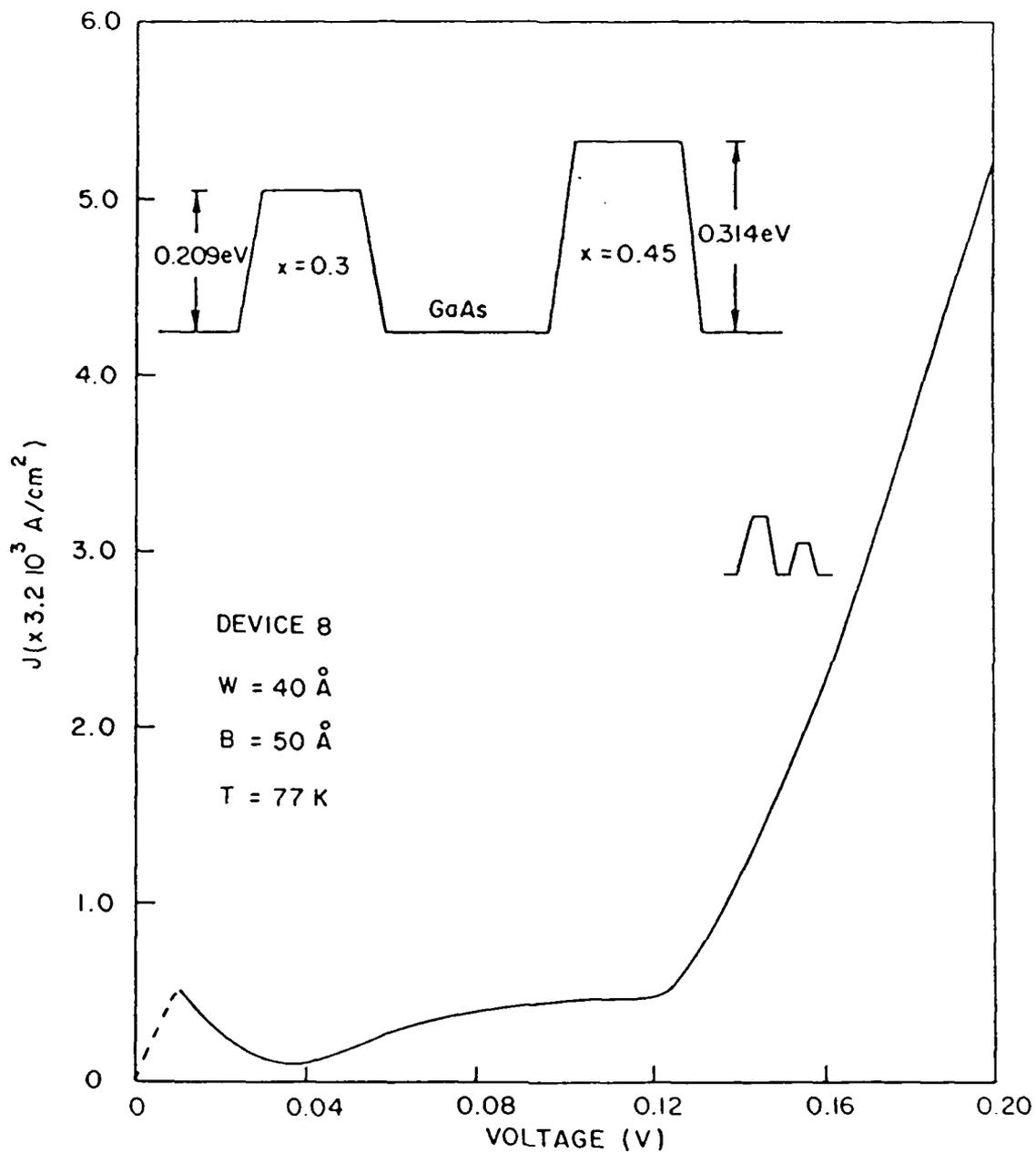
VOLTAGE (V)

Figure 18: Current-Voltage Characteristic for device #8 of Table II. This I-V curve corresponds to the reversed bias case of the I-V curve shown in figure 17. The parameters of the RTD are shown in the inset. The dashed line is the expected shape of the I-V curve at low value of bias.
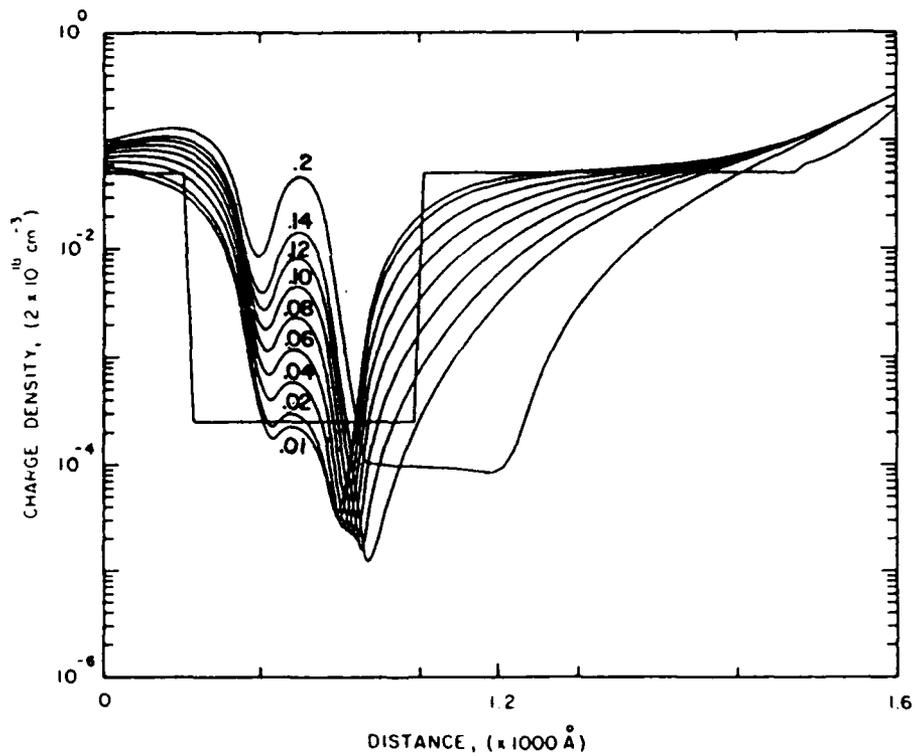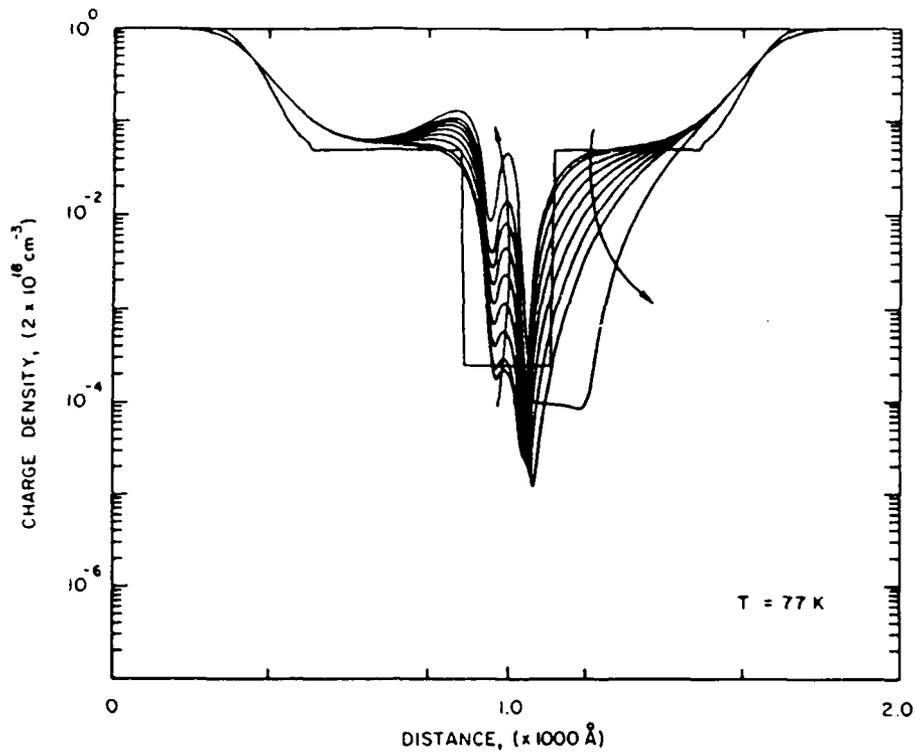
Figure 19a: Charge Density profile as a function of applied bias for device #7 of Table II. The arrows indicate the evolution of the charge density for increasing values of bias (0.01; 0.02; 0.04; 0.06; 0.08; 0.10: 0.12; 0.14; 0.20). The lower figure zooms on the inner portion of the upper one.
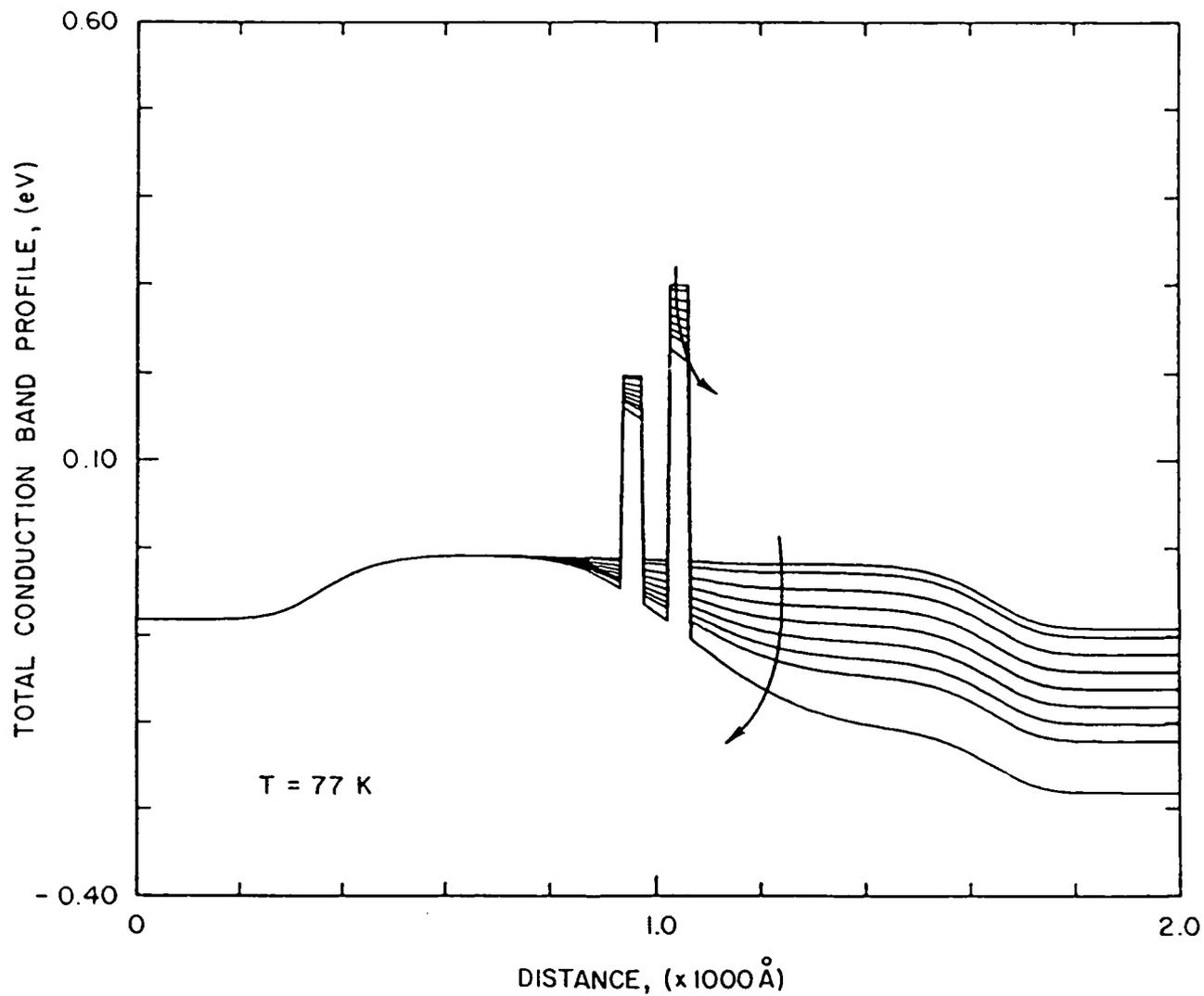
Figure 19b: Conduction Band Energy profile as a function of applied bias
for device #7 of Table II. The arrows indicate the evolution
of the charge density for increasing values of bias (0.01;
0.02; 0.04; 0.06; 0.08; 0.10; 0.12; 0.14; 0.20).
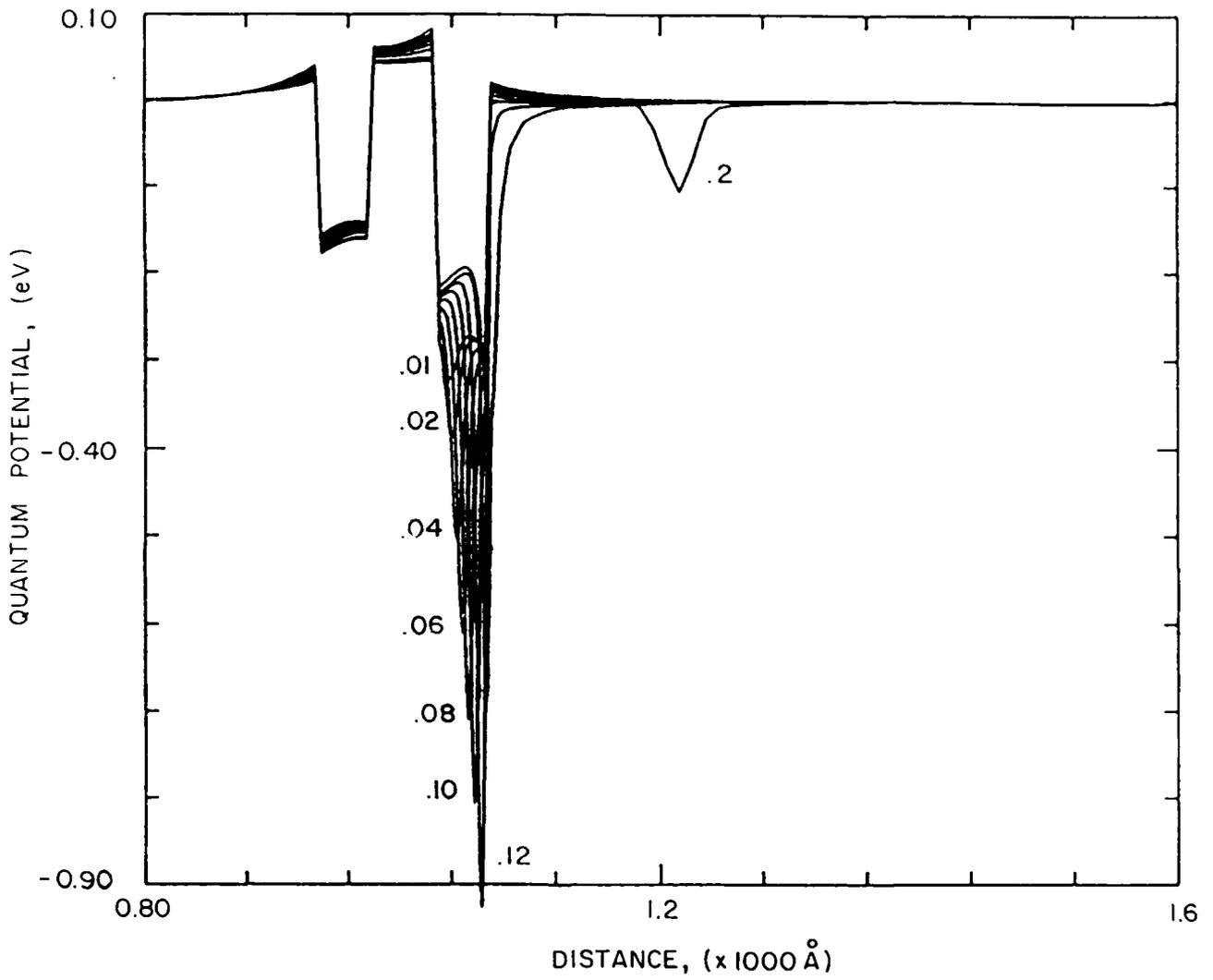
Figure 19c: Variation of the Quantum potential as a function of
applied bias for device #7 of Table II. Only the interior
portion of the device is shown. The curves are labeled with
the value of bias at which they are calculated (0.01: 0.02;
0.04: 0.06; 0.08; 0.10; 0.12; 0.20)

- 60 -
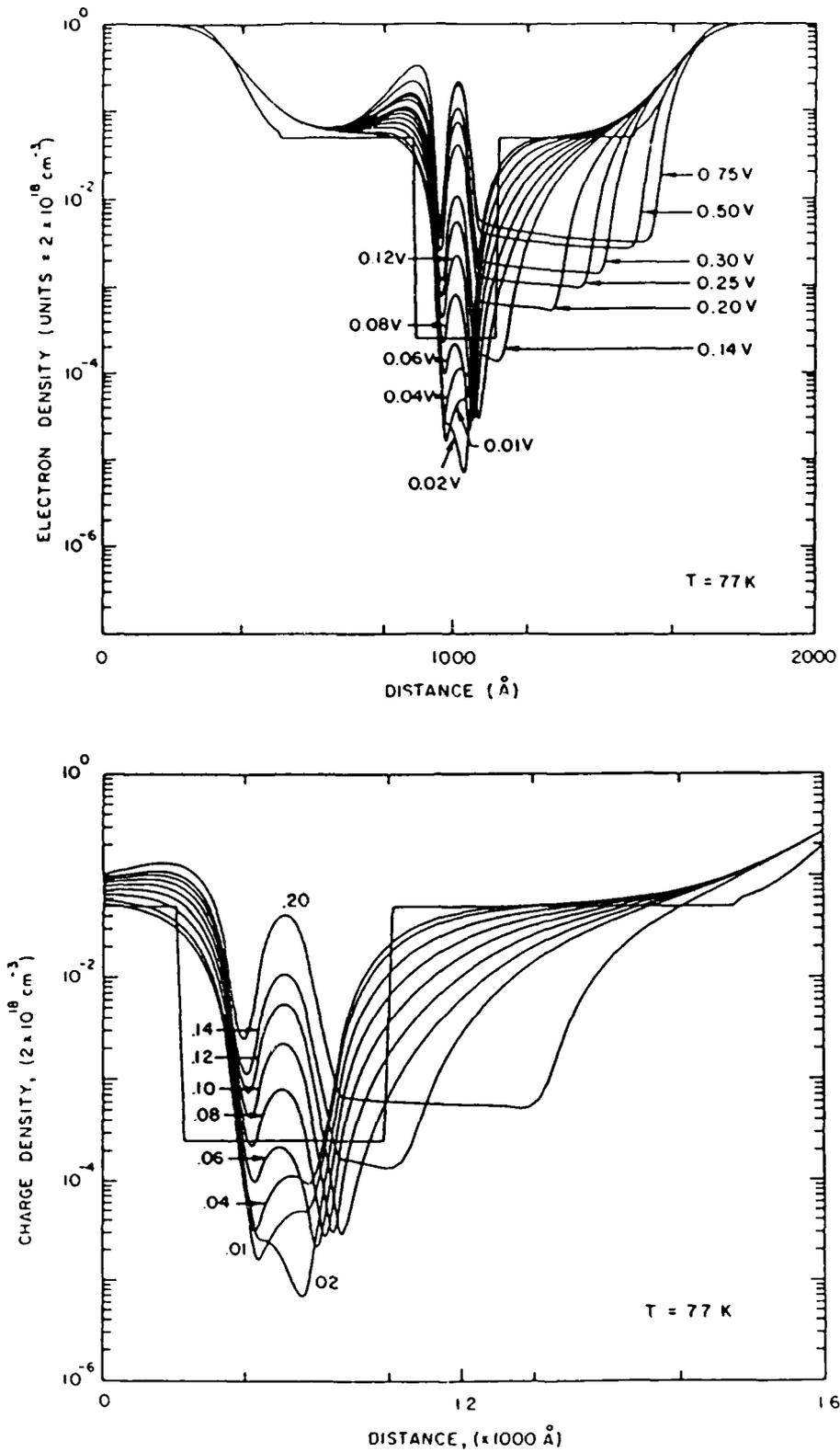
Figure 20a: Charge-Density profile as a function of applied bias for
              device #8 of Table II. The lower curve zooms on the
              inner portion of the device. Notice the decrease of the
              charge-density in the well for low values of bias.
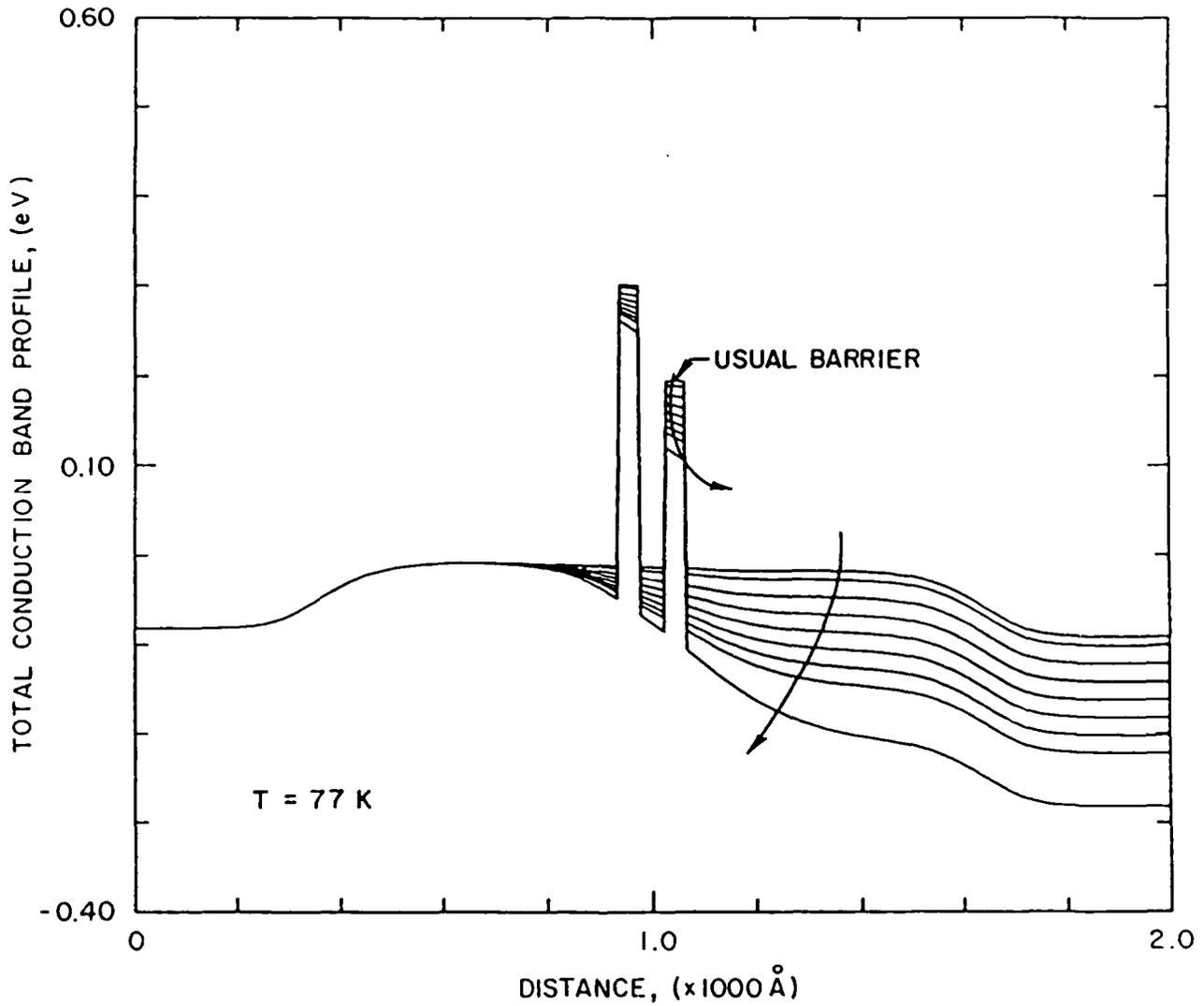
Figure 20b: Conduction Band Energy profile as a function of applied
bias for device #8 of Table II. The arrows indicate the
evolution of the charge density for increasing values of
bias.
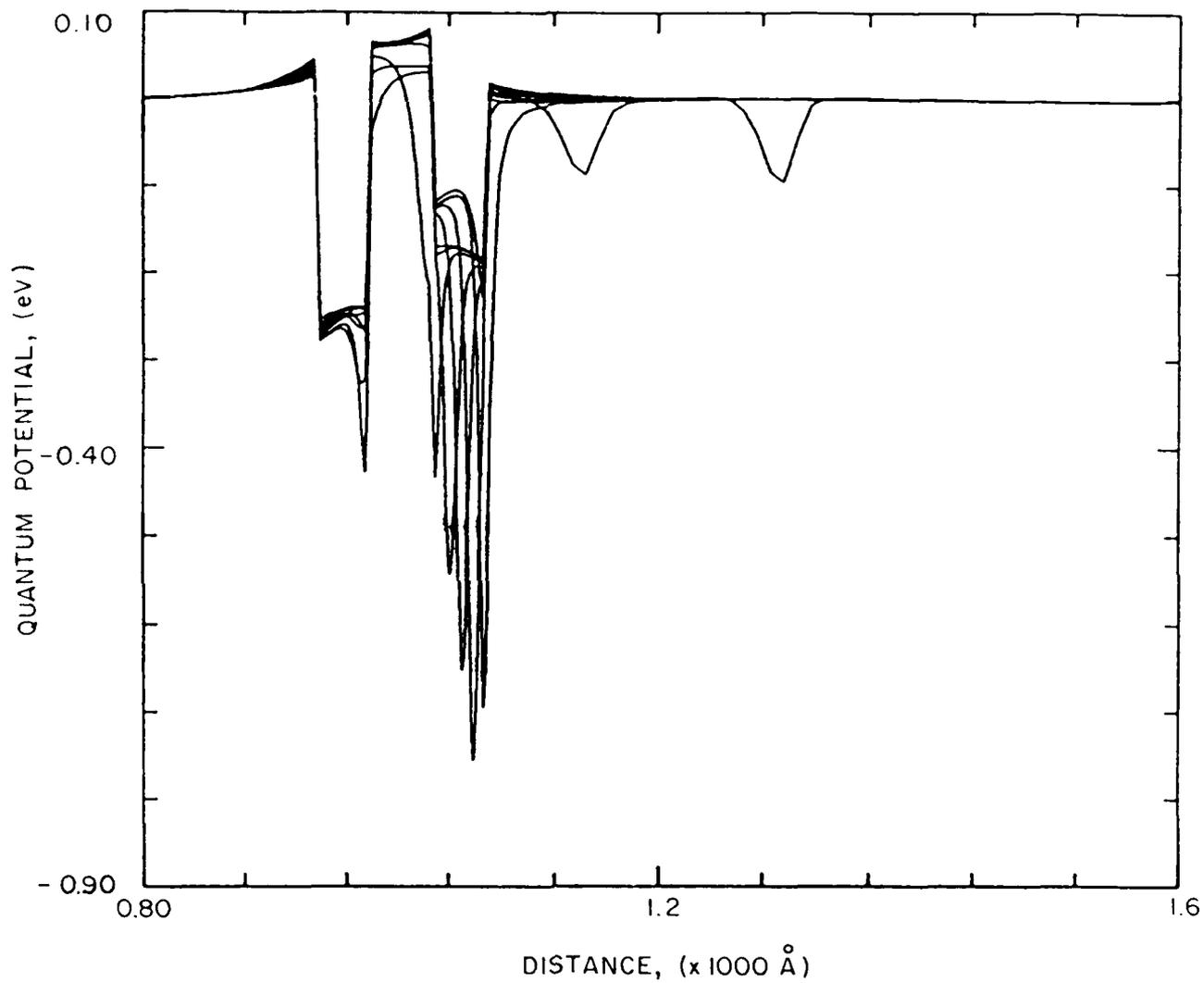
Figure 20c: Variation of the Quantum Potential as a function of applied
bias for device #8 of Table II. Only the interior portion
of the structure is shown. The curves are labeled with the
value of bias at which they are calculated.

a)
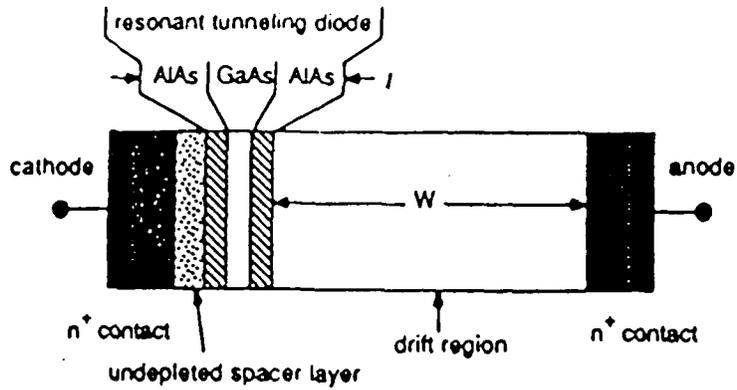
b)
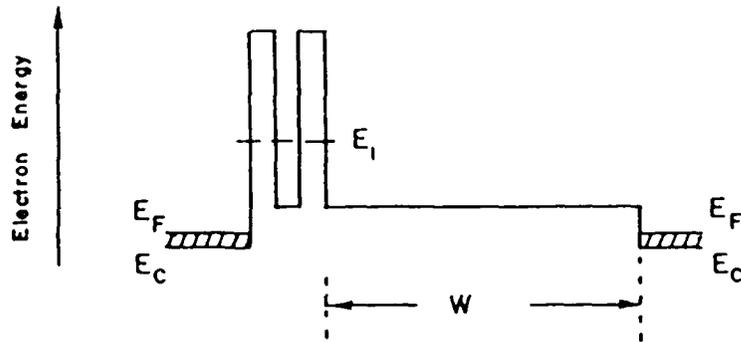
Figure 21: a) Physica' structure of a Transit-Time Device using
Quantum-well injection (QWITT) (Ref. 20).
b) Energy band diagram of the device when no bias is
applied. The length of the transit-time region W must
be greater than the quantum-well thickness for typical
millimeter-wave frequencies.

Appendix A - Solution of the Governing Equations

In order to solve the systems of equations (42a, 42b, 44, 48, 49) numerical techniques must be used. The numerical method used in the present algorithm is based on application of consistently split, linearized, block implicit (LBI) methods, as developed by Briley and McDonald [24] to the system of eqs. (42a, 42b, 44, 48, 49). LBI techniques center about the use of a formal linearization procedure in which systems of coupled nonlinear PDEs in one space dimension are reduced to a system of linear equations, which upon application of spatial differencing, may be expressed as a block coupled matrix system. The resulting system may then be solved efficiently to advance the solution in time, or to iterate to a steady state.

Briley and McDonald [24] considered the coupled system of ℓ nonlinear, time-dependent, multidimensional equations given by

$$\frac{\partial H(\phi_\ell)}{\partial t} = D(\phi_\ell) + S(\phi_\ell) \tag{A-1}$$

In Eq. [A-1] ϕ_ℓ represent the vector of dependent variables. $H(\phi_\ell)$ and $S(\phi_\ell)$ are nonlinear functions of ϕ_ℓ which contain no spatial operators, and $D(\phi_\ell)$ is a general, nonlinear, multidimensional, partial differential operator, Equation (A-1) is first time differenced about $t^n + \beta \Delta t$ as

$$\frac{H(\phi)^{n+1} - H(\phi)^n}{\Delta t} = \beta [D(\phi)^{n+1} + S(\phi)^{n+1}] + (1 - \beta) [D(\phi)^n + S(\phi)^n] \tag{A-2}$$

where $\Delta t = t^{n+1} - t^n$, and the subscript ℓ has been dropped for clarity. The parameter $\beta = 1$ for a fully implicit scheme or $\beta = 0.5$ for the Cranck-Nicolson formulation. The implicit level nonlinear operators H, D, and S are then formally linearized using a Taylor series expansion about the explicit time level

$$G(\phi)^{n+1} = G(\phi)^n + \left.\frac{\partial G(\phi)}{\partial \phi}\right|^n \Delta\phi^{n+1} + O(\Delta t^2) \tag{A-3}$$

Equation (A-2) may then be expressed at each grid point in the solution domain as a matrix equation of the form

$$(A + \Delta t L) \Delta\phi^{n+1} = \Delta t [D(\phi^n) + S(\phi^n)], \tag{A-4}$$

where

$$A = \left[\frac{\partial H}{\partial \phi}\right]^n - \beta \, \Delta t \, \left[\frac{\partial S}{\partial \phi}\right]^n \qquad \text{(A-5)}$$

and

$$L = -\beta \frac{\partial D}{\partial \phi}\Bigg|^n \qquad \text{(A-6)}$$

As a result, the nonlinear, coupled system of PDEs given by Eq. (A-1) has been reduced to a block lxl coupled, linear system of temporal difference equations (Eq. A-4) which, upon spatial differencing, need only be solved once per time step to obtain a transient solution. Additionally, since the linearization error is at worst of the same order as the temporal discretization error, the linearization is not expected to introduce significant inaccuracies.

Application of Eq. (A-4) to second order PDEs in one space dimension, using standard three-point spatial difference approximations requires the solution of one block lxl tridiagonal system per time step. Such a system can be solved efficiently using standard block-tridiagonal elimination procedures.

Since in the present application only steady state solutions are of interest, the time step may be viewed as a relaxation parameter, and as the solution approaches convergence the time step may be allowed to become very large without consideration of transient accuracy. As the time step goes to infinity the LBI scheme in one dimension reduces to Newtons method. Thus, as applied here, the LBI scheme may be thought of as a relaxed Newton method.

We note, however, that Poisson's equation, the equation defining Q and the equation relating N, N_c and x_f do not contain time derivatives. Since Poisson's equation is linear there is no potential problem there. However, the nonlinearities in the Q and x_f equations do represent possible problem sources in the numerical scheme. Numerical experiments revealed no problem with the Q equation, however in order to obtain converged solutions under arbitrary bias conditions it was necessary to recast Eqs. (42a,b) as

$$\frac{\partial N}{\partial t} = x_f - f(n/Nc) \qquad \text{(A-7)}$$

where $f(n/Nc)$ represent the appropriate function depending on the magnitude of x_f. This gives rise to an exponential decay of the carrier density to its steady state value and provides the necessary stability to the scheme.

With regard to spatial difference approximation standard three point central differences were applied in a manner which assured conservation of current and momentum.

Appendix B - Moments of the Density Matrix

The motivation for the equations discussed in the text finds further justification in examining the moments of the density matrix. We start the discussion from the single electron Hamiltonian:

$$H = \frac{p^2}{2m} + E(q) + H_{sc} \tag{B-1}$$

The eigenstates of the single particle Hamiltonian in the absence of scattering form the basis for calculating the ensemble averages of such quanties as the mean density, the mean current, etc. For example, the time rate of change of the ensemble averaged density operator:

$$p(o) = N(q_o) = |q_o><q_o| \tag{B-2}$$

is:

$$\frac{\partial}{\partial t} <<N(q_o)>> + \frac{1}{m}\frac{\partial}{\partial q_o} <<p^{(1)}>> = <<[N(q_o),H_{sc}]>>/i\hbar$$

$$= \frac{\partial}{\partial t}<<N(q_o)>>\Big|_{collision} \tag{B-3}$$

where

$$p^{(1)} = -\left[p|q_o><q_o| + |q_o><q_o|p\right] \tag{B-4}$$

is a symmetrized momentum density operator. The above operators have simple expressions in the energy representation:

$$<<N(q_o)>> = \sum_{mm'}\rho_{mm'}\Psi_{m'}^*(q_o)\Psi_m(q_o) = n(q_o) \tag{B-5}$$

If density matrix is diagonalized

$$<<N(q_o)>> = \sum_{mm}\rho_{mm}\Psi_m^*(q_o)\Psi_m(q_o) \tag{B-6}$$

Recalling the definition of a trace of a matrix

$$Tr\rho = 1 \tag{B-7}$$

for a pure state $\rho_{mm} = 1/N$, and:

$$<<N(q_o)>> = \Psi_m^\dagger(q_o)\Psi_m(q_o) \tag{B-8}$$

Also

$$<<P^{(1)}>> = \left[\frac{\hbar}{2i}\right] \sum_{mm'}\rho_{mm'}\left(-\frac{\partial\Psi_{m'}^*}{\partial q_o}\Psi_m + \frac{\partial\Psi_m}{\partial q_o}\Psi_{m'}^*\right) \tag{B-9}$$

If density matrix is diagonalized

$$<<p^{(1)}>> = \frac{\hbar}{2i}\sum_m \rho_{mm}\left(-\frac{\partial\Psi_m^*}{\partial q_o}\Psi_m + \frac{\partial\Psi_m}{\partial q_o}\Psi_m^*\right) \tag{B-10}$$

For a pure state

$$<<p^{(1)}>> = \frac{\hbar}{2i}\left[-\frac{\partial \Psi_m^*}{\partial q_o}\Psi_m + \frac{\partial \Psi_m}{\partial q_o}\Psi_m^*\right]$$

(B-11)

Without any loss of generality, let

$$\Psi = A_m \exp[iS_m/\hbar]$$

(B-12)

where A_m and S_m are real functions of position and time, and where Ψ is a solution to Schrodinger's equation

$$H\Psi = \left[\frac{p^2}{2m} + E(q)\right]$$

(B-13)

Now in a diagonal energy representation

$$<< N_o >> = \sum \rho_{mm} \Psi_m^* \Psi_m$$

(B-14)

$$= \sum \rho_{mm}A_m^2 \equiv \sum \rho_{mm}\, n_m(q_o) = n(q_o)$$

Also

$$<<P^{(1)}>> = \frac{\hbar}{2i} \sum \rho_{mm}\left[-\frac{\partial \Psi_m^*}{\partial q_o}\Psi_m + \frac{\partial \Psi_m}{\partial q_o}\Psi_m^*\right]$$

(B-15a)

$$= \sum \rho_{mm}A_m^2\frac{\partial S_m}{\partial q_o} \quad \bullet \sum \rho_{mm}n_m(q_o)p_m(q_o)$$

(B-15b)

where

$$p_m(q_o) \bullet \frac{\partial S_m}{\partial q_o}$$

(B-16)

With

$$<<P^{(1)}>> \equiv P(q_o)$$

(B-17)

identified as a momentum density, and with the following definitions of a drift velocity and drift momentum:

$$v_d \equiv P(q_o)/mn(q_o)$$

(B-18a)

$$p_d \equiv mv_d$$

(B-18b)

we obtain the familiar continuity equation:

$$\frac{\partial n(q_o)}{\partial t} + \frac{\partial n(q_o)v_d}{\partial q_o} = \frac{\partial n(q_o)}{\partial t}\bigg|_{collision}$$

(B-19)

Consider next the time rate of change of the ensemble averaged momentum density operator:

$$\frac{\partial}{\partial t}<<P^{(1)}>> + \frac{1}{m}\frac{\partial}{\partial q_o}<<P^{(2)}>>$$

$$= -\frac{\partial E}{\partial q_o}<<P^{(0)}>> + <<[P^{(1)},H_{sc}]>>/i\hbar$$

$$= -\frac{\partial E}{\partial q_o}<<P^{(0)}>> + \frac{\partial}{\partial t}<<P^{(1)}>>\Big]_{coll} \tag{B-20}$$

where

$$P^{(2)} = \left[\frac{1}{2}\right]^2\left[p^2|q_o><q_o| + 2p|q_o><q_o|p^2 + |q_o><q_o|p^2\right] \tag{B-21}$$

is the symmetrized energy density operator. In the energy representation

$$<<P^{(2)}>> = \left[\frac{\hbar}{2i}\right]^2\sum\rho_{mm'}\left[\frac{\partial^2\Psi_{m'}}{\partial q_o^2}\Psi_m^* -2\frac{\partial\Psi_{m'}}{\partial q_o}\frac{\partial\Psi_m^*}{\partial q_o} + \Psi_{m'}^*\frac{\partial^2\Psi_m}{\partial q_o^2}\right] \tag{B-22}$$

For a diagonal density matrix

$$<<P^{(2)}>> = \left[\frac{\hbar}{2i}\right]^2\sum\rho_{mm}\left[\frac{\partial^2\Psi_m^*}{\partial q_o^2}\Psi_m -2\frac{\partial\Psi_m^*}{\partial q_o}\frac{\partial\Psi_m}{\partial q_o} + \Psi_m^*\frac{\partial^2\Psi_m}{\partial q_o^2}\right] \tag{B-23}$$

For a pure state

$$<<P^{(2)}>> = \left[\frac{\hbar}{2i}\right]\left[\frac{\partial^2\Psi_m^*}{\partial q_o^2}\Psi_m -2\frac{\partial\Psi_m^*}{\partial q_o}\frac{\partial\Psi_m}{\partial q_o} + \Psi_m^*\frac{\partial^2\Psi_m}{\partial q_o^2}\right] \tag{B-24}$$

In terms of the amplitude and phase, in a diagonal representation:

$$<<P^{(2)}>> = \sum\rho_{mm}\left[\frac{\partial S_m}{\partial q_o}\right]^2 A_m^2 - \frac{\hbar^2}{2}\sum\rho_{mm}\left[\frac{\partial^2 A_m}{\partial q^2} -\left[\frac{\partial A_m}{\partial q_o}\right]^2\right] \tag{B-25}$$

Now

$$2\left[A_m\frac{\partial^2 A_m}{\partial q_o^2} - \left[\frac{\partial A_m}{\partial q_o}\right]^2\right] = A_m^2\frac{\partial^2}{\partial q_o^2}(\ell nA_m^2)$$

$$\tag{B-26}$$

$$= n_m\frac{\partial^2}{\partial q_o^2}(\ell nn_m)$$

Now

$$\sum\rho_{mm}\,p_m(q_o)\,n_m(q_o) = \sum\rho_{mm}(p_m-p_d+p_d)^2 n_m \tag{B-27}$$

Thus

$$<< P^{(2)} >> = n(q_0) p_d^2 + \sum \rho_{mm} n_m (p_m - p_d)^2$$
$$- \frac{\hbar^2}{4} \sum \rho_{mm} n_m \frac{\partial^2}{\partial q_0^2} (\ell n n_m) \tag{B-28}$$

Defining a stress tensor, in one dimension as

$$\Omega = m^{-1} \sum \rho_{mm} (p_m - p_d)^2 \tag{B-29}$$

equation 2-28 becomes

$$<< P^{(2)} >> = n p_d^2 + m\Omega - \frac{\hbar^2}{4} \sum \rho_{mm} n_m \frac{\partial^2}{\partial q_0^2} (\ell n n_m) \tag{B-30}$$

In one dimension, the stress tensor, with the distribution function representing a Maxwellian, is equal to

$$\Omega = n k T_e \tag{B-31}$$

where T_e is an electron temperature. Thus the momentum balance equation has the form

$$\frac{\partial n p_d}{\partial t} + \frac{\partial n p_d v_d}{\partial q_0} =$$
$$- n \frac{\partial E}{\partial q_0} - \frac{\partial}{\partial q_0} \Omega + \frac{\hbar^2}{4m} \frac{\partial}{\partial q_0} \sum \rho_{mm} n_m \frac{\partial^2}{\partial q_0^2} (\ell n n_m) + \frac{\partial}{\partial t} <<P^{(1)}>> \Big|_{coll} \tag{B-32}$$

For the case when derivatives and summation signs may be interchanged:

$$\frac{\hbar^2}{4m} \frac{\partial}{\partial q_0} \sum \rho_{mm} n_m \frac{\partial^2}{\partial q_0^2} (\ell n n_m) = \frac{\hbar^2}{4m} \sum \rho_{mm} \frac{\partial}{\partial q_0} \left[\frac{\partial^2}{\partial q_0^2} (\ell n n_m) \right] \tag{B-33}$$

Straight forward manipulation shows that

$$\frac{\hbar^2}{4m} \sum \rho_{mm} \frac{\partial}{\partial q_0} \left[n_m \frac{\partial^2}{\partial q_0^2} (\ell n n_m) \right] = \frac{\hbar^2}{2m} \sum \rho_{mm} \frac{\partial}{\partial q_0} \frac{1}{(n_m)^{\frac{1}{2}}} \frac{\partial^2 (n_m)^{\frac{1}{2}}}{\partial q_0^2} \tag{B-34}$$

and the momentum balance equation reads (after further manipulation)

$$\frac{\partial}{\partial t} n p_d + \frac{\partial n p_d v_d}{\partial q_0} = - \sum \rho_{mm} n_m \frac{\partial}{\partial q_0} (V + Q_m) - \frac{\partial}{\partial q_0} \Omega$$
$$+ \frac{\partial <<P^{(1)}>>}{\partial t} \Big|_{coll} \tag{B-35}$$

where
$$Q_m = - \frac{\hbar^2}{2m} \frac{1}{(n_m)^{\frac{1}{2}}} \frac{\partial^2 (n_m)^{\frac{1}{2}}}{\partial q_0^2} \tag{B-36}$$

behaves as a density dependent potential

We next consider the energy balance equation:

$$\frac{\partial}{\partial t} << P^{(2)} >> + \frac{1}{m}\frac{\partial}{\partial q_0} << P^{(3)} >> = 2\frac{\partial E}{\partial q_0} <<P^{(1)} >>$$

$$+ <<P^{(2)},H_{sc}>>/\hbar i \qquad (B-37)$$

where

$$P^{(3)} = \left[\frac{1}{2}\right]^3 \left[p^3 |q_0><q_0| + 3p|q_0><q_0|p^2 + 3p^2|q_0><q_0|p + |q_0><q_0|p^3\right]$$

$$(B-38)$$

In the energy representation

$$<<P^{(3)}>>=\left[\frac{\hbar}{2i}\right]^3 \sum \rho_{mm'}\left[\Psi_m^{*'}\frac{\partial^3\Psi_m}{\partial q_0^3} + \frac{\partial^2\Psi_m^{*}}{\partial q_0^2}\frac{\partial\Psi_m}{\partial q_0} - 3\frac{\partial\Psi_m^{*}}{\partial q_0}\frac{\partial^2\Psi_m}{\partial q^2_0} - \frac{\partial^3\Psi_m^{*}}{\partial q^3_0}\Psi_m\right]$$

$$(B-39)$$

In the diagonal representation, and expressing the results in terms of the amplitude and phase

$$<<P^{(3)}>> = n_0 p_d^3 + 3m p_d \Omega + U - \frac{3\hbar^2}{4}\sum \rho_{mm}\left[n_m\frac{\partial^2 \ell n n_m}{\partial q_0^2}\right]\frac{\partial S_m}{\partial q_0} - \frac{\hbar^2}{4}\sum \rho_{mm}n_m\frac{\partial^3 S_m}{\partial q_0^3} \quad (B-40)$$

where
$$U \equiv \sum \rho_{mm}n_m(p_m - p_d)^3 \qquad (B-41)$$

Equation (B-37) with $<<P^{(3)}>>$ given by equation (B-40) are to be inserted into the energy balance equation for solution.

Appendix C - Alternative Theoretical Formulation

There has been previous attempts to derive a close self-consistent set of moment equations of the Liouville equation [25,26]

$$i\hbar \partial \rho(x,x';t)/\partial t = [H, \rho(x,x';t)] \tag{C-1}$$

where ρ is the full density matrix and H is the Hamiltorian of the system (the gas of electrons flowing from both contact in our case). In their derivation, Ploszojczak and Rhoades-Brown [25] use the Wigner representation [20] as a tool to approximate the Liouville equation for the time evolution of the density matrix. In their approach, the off diagonal elements of the density matrix are expanded in powers of deviations from the mean momentum value defined as follows

$$<(p-\bar{p})^n> = \rho_0^{-1} \int f(x,p) \ (p-\bar{p})^n dp \tag{C-2}$$

where $\bar{p}$ is defined as

$$\rho_0 \bar{p} = \int f(x,p) p \, dp \tag{C-3}$$

and corresponds to the time-dependent momentum-distribution function $p(x,t)$.
ρ_0 is the diagonal one-body density matrix and $f(x,p)$ is the one-body Wigner distribution function. Using their approximation for the off-diagonal elements of the density matrix, Ploszajczak and Rhoades-Brown derive the following set of moment equations

• Continuity equation

$$\frac{\partial}{\partial t} \rho_0 = \frac{-1}{m} \frac{\partial}{\partial x}(\rho_0 \bar{p}) \tag{C-4}$$

• Momentum balance equation

$$\frac{\partial}{\partial t} \bar{p} = -\frac{\partial}{\partial x}H_{cL} - \frac{1}{m\rho_0} \frac{\partial}{\partial x} [\rho_0 < (p-\bar{p})^2>] \tag{C-5}$$

• Energy balance equation

$$\rho_0 \frac{\partial}{\partial t} < (\bar{p}-p)^2> = \frac{-\bar{p}}{m}\frac{\partial}{\partial x}[\rho_0 < (p-\bar{p})^2>] + \frac{\bar{p}}{m} < (p-\bar{p})^2 > \frac{\partial \rho_0}{\partial x} \tag{C-6}$$

$$\frac{-2\rho_0}{m} \frac{\partial p}{\partial x} < (p-p)^2>$$

-72-

where $H_{cL} = \left[\dfrac{\bar{p}^2}{2m}\right] + V_{eff}(x)$ and the constraining equation

$$\frac{1}{m}\frac{\partial}{\partial x}\,[\rho_O <(p-\bar{p})^2>] = \frac{\hbar^2}{12}\frac{\partial^3 V_{eff}}{\partial x^3}\,\rho_O\,[<(p-\bar{p})^2>]^{-1} \qquad \text{(C-7)}$$

This last equation is an expression of the spatial properties of $\rho_O <(p-\bar{p})^2>$ in terms of the higher-order derivatives of V_{eff}. The potential $V_{eff}(x)$ includes the conduction band discontinuities and the Hartree contribution, i.e., the electrostatic potential solution of Poisson's equation.

The formalism above doesn't include any relaxation contribution on the right hand side of eqs (C-5) and (C-6). While using the constraining condition (C-7) into eq. (C-5), the momentum balance equation can be rewritten.

$$\qquad \text{(C-8)}$$

$$\frac{\partial \bar{p}}{\partial t} = -\frac{\partial H_{cL}}{\partial x} - \frac{\hbar^2}{12\Delta P}\frac{\partial^3 V_{eff}}{\partial X3}$$

where

$$\qquad \text{(C-9)}$$

$$\Delta P = <(p-\bar{p})^2>$$

This equation should be compared with the one obtained in our formalism equation (34), after manipulation with the continuity equation, while neglecting the $1/\tau$ relaxation term and assuming a constant effective-mass throughout the structure. In that case, equation (34) becomes

$$\qquad \text{(C-10)}$$

$$\frac{\partial \bar{p}}{\partial t} = -\frac{\partial}{\partial x}\left[\frac{\bar{p}^2}{\partial m} + V(x) - Q\right] - \frac{2}{3\rho_O}\frac{\partial}{\partial x}\,(\rho_O kT\; G[(E_F - E_C)/k_B T])$$

Where G represents the contribution of mixed states - a feature missing from the formalism of equations C-1 thru C-10. In the limit where $\hbar \to 0$, both eqs. (C-8) and (C-10) agree with the momentum-balance equation of the Boltzman equation. The difference between eqs. (C-8) and (C-10) comes basically from the quantum correction (term proportional to $\hbar^2$ in both equations). Further work is needed to understand the relationship between the two approximations.

The full derivation of the energy-balance equation using our formalism and its implementation in our numerical algorithm will be undertaken in the future. We also intend to compare the results of our approach to that taken by Stroscio [26] which nobody has so far tried to solve numerically to the best of our knowledge.

List of References

[1] Tom P.E. Broekaert, Wai Lee and Clifton G. Fonstad, "Pseudo-morphic $In_{0.53}$ $Ga_{0.47}$ As/AlAs/InAs resonant tunneling diodes with peak-to-valley current ratios of 30 at room temperature", Appl. Phys. Lett. 53 (16), 1545-1547 (1988).

[2] L. L. Chang, L. Esaki and R. Tsu, "Resonant Tunneling in Semiconductor Double Barriers", Appl. Phys. Lett. 24, 593 (1974).

[3] T. C. L. G. Sollner, W. D. Goodhue, P. E. Tannenwald, C. D. Parker and D. D. Peck, "Resonant Tunneling Through Quantum Wells at Frequencies up to 2.5 THZ", Appl. Phys. Lett. 43, 588 (1983).

[4] A. R. Bonnefoi, R. T. Collins, T. C. McGill, R. D. Burnham and F. A. Ponce, "Resonant Tunneling in GaAs/AlSb Heterostructures Grown by Metalorganic Chemical Vapor Deposition", Appl. Phys. Lett. 46, 285 (1985).

[5] S. Ray, P. Ruden, V. Sokolov, R. Kolbas, R. Boonstra and J. Williams, "Resonant Tunneling at 300K in GaAs-AlGaAs Quantum Wells Grown by Metalorganic Chemical Vapor Deposition", Appl. Phys. Lett. 48, 1666 (1986).

[6] C. I. Huang, M. L. Paulus, C. A. Bozada, S. C. Dukley, K. R. Evans, C. E. Stutz, R. L. Jones and M. E. Cheney, "AlGaAs/GaAs Double Barrier Diodes With High Peak-To-Valley Current Ratio", Appl. Phys, Lett., 51, 121 (1987).

[7] S. C. Kan, H. Morkoc and A. Yariv, "GaAs/AlAs Double-Barrier Resonant Tunneling Structure on Si With Large Peak to Valley Ratio at Room Temperature", Appl. Phys. Lett. 52, 2250 (1988).

[8] L. Esaki, and R. Tsu, "Superlattice and Negative Differential Conductivity in Semiconductors", IBM Journal of Research and Development, pp. 61-65, 1970.

[9] S. Luryi, "Frequency Limit of Double-Barrier Resonant Tunneling Oscillators", Appl. Phys. Lett. 47, 70 (1985).

[10] M. O. Vassell, Johnson Lee and H. F. Lockwood, "Multibarrier Tunneling in $Al_xGa_{1-x}As$/GaAs Heterostructures", J. Appl. Phys. 54, 5206 (1983).

[11] M. Cahay, M. McLennan, S. Datta and M.S. Lundstrom, "Importance of Space-Charge Effects in Resonant Tunneling Devices", Appl. Phys. Lett. 50, 612 (1987).

[12] K. M. S. V. Bandara and D. D. Coon, "Electron-Electron Interactions and Resonant Tunneling in Heterostructures", Appl. Phys. Lett. 53 (19), 1865 (1988).

[12b] B. Jogai et al. (preprint 1989).

[13] W. R. Frensley, "Transient Response of a Tunneling Device Obtained from the Wigner Function", Phys. Rev. Letters, 57, 2853 (1986).

[14]   R.K. Mains and G. I. Haddad, "Wigner Function Modeling of Resonant Tunneling
        Diodes with High Peak-to-Valley Ratios", J. Appl. Phys. 64, 5041 (1988).

[14b]   C. Philippidis, D. Bohm and R. D. Kaye, IL Nuovo Cimento, 71B, 75 (1982)

[14c]   D. Bohm "Quantum Theory", Prentice Hall.

[14d]   SRA report (unpublished)

[14e]   S. G. Radshteyn, I. M. Ryzhik, Table of Integrals

[14f]   Messiah, Quantum Mechanics", Vol. 1.

[15]   M. G. Ancona and G. J. Iafrate (preprint)

[16]   B. Ricco and M. Ya. Azbel, "Physics of Resonant Tunneling. The One-Dimensional
        Double-Barrier CAse", Physical Review B, 29 (4), pp. 1970-1981 (1984).

[16b]   R. Landauer, talk presented at A.P.S. meeting, St. Louis (March 1989)

[16c]   V. J. Goldman, D. C. Tsui and J. E. Cunningham, Phys. Rev. Lett. 58, 1256 (1987).

[16d]   V. J. Goldman, D. C. Tsui and J. E. Cunningham, Phys. Rev. B, 9387 (1987).

[17]   Vijay P. Kesan, Dean P. Neikirk, Ben G. Streetman and Peter A. Blakley, "A New
        Transit Time Device Using Quantum Well Injection", IEEE Electron Device
        Letters, Vol. EDL-8, No. 4, p. 129 (1987).

[18]   Jumping Zou, Jingming Xu and Mark Sweeney, "Effects of Asymmetric
        Barriers on Resonant Tunneling Current", Semicond. Sci. Technol. 3, 819-822
        (1988).

[19]   J. S. Blakemore, J. Appl. Phys. 53, 123 (1982).

[20]   E. P. Wigner, "On the Quantum Correction for Thermodynamic Equilibrium", Phys,
        Rev. 40, 749 (1932).

[21]   William R. Frensley, "Quantum Kinetic Theory of Nanoelectronic Devices", talk
        presented at the First International Symposium on Nanostructure Physics and
        Fabrication, College Station, Texas A & M, Texas (1989).

[22]   K. Diff and G. Neofotistos, "Resonant Tunneling in Double Barrier Diodes", poster
        presented at the First International Symposium on Nanostructure Physics and
        Fabrication, College Station, Texas A & M, Texas (1989).

[23]   N. C. Kluksdahl, A. M. Kriman and D. K. Ferry, "Self-Consistent Study of the
        Resonant Tunnelng Diode", to appear in Phys. Rev. B.

[24]   Briley and McDonald, "On the Structure and Use of Linearized Block Implicit
        Schemes", Journal of Computational Physics, 34, p. 54 (1978).